

**System Design and Validation of
Multi-Band OFDM Wireless Communications
with Multiple Antennas**

Von der Fakultät für Elektrotechnik und Informatik
der Gottfried Wilhelm Leibniz Universität Hannover
zur Erlangung des akademischen Grades

Doktor-Ingenieur

(Dr.-Ing.)

genehmigte

Dissertation

von M.Sc. Emil Dimitrov

geboren am 01.10.1977 in Sofia

2013

Referent: Prof. Dr.-Ing. Thomas Kaiser

Korreferent: Prof. Dr.-Ing. Holger Blume

Vorsitzender: Prof. Dr.-Ing. Markus Fidler

Tag der Promotion: 06.03.2013

Acknowledgements

This thesis would not have been possible without the restless support of all those people who have accompanied me during the past years of my PhD studies.

Especially, I would like to thank Prof. Dr.-Ing. Thomas Kaiser for providing me with the opportunity to join his research team, as well as for the profound theoretical and practical insights, encouraging support and guiding throughout my research activities at the Institute of Communications Technology (IKT). My sincere appreciation and gratitude belong likewise to Prof. Dr.-Ing. Holger Blume and Prof. Dr.-Ing. Markus Fidler, for the fruitful discussions and close supervision of my work.

Furthermore, I want to express my grateful recognition to all the colleagues, team members and research partners, who have shared their great expertise, academic dedication and social spirit with me.

Last but not least, my very acknowledgements go to my family and friends for the firm belief and moral assistance in pursuing my scientific goals.

Kurzfassung

Multiple-Input Multiple-Output (MIMO)-Systeme werden weithin als eine praktikable Lösung geschätzt, um die gegenwärtigen Beschränkungen der drahtlosen Kommunikation zu überwinden. Aufgrund der hohen Energiestreuung sowie der weiten Winkelspreizung des Mehrwegekanals findet die Anwendung der Ultra-Breitband (UWB)-Technologie in Verbindung mit MIMO besonders im Innenbereich einen idealen Einsatzort. Durch Erschließung eines zusätzlichen Freiheitsgrades für die Kommunikation ermöglicht der Einsatz mehrerer Antennen am Sender und/oder Empfänger eine vorteilhafte Nutzung der Mehrwegeausbreitung, wobei letztere ja ursprünglich als Nachteil im Bereich der drahtlosen Kommunikation erachtet wurde, sodass es nunmehr möglich ist, die Systemkapazität linear zu steigern oder ebenso eine Optimierung der Abdeckung und Robustheit durch Verringerung der Fehlerrate zu erzielen.

Während die Vorzüge der MIMO-Technologie im Bereich der Breitband-MIMO-OFDM-Drahtloskommunikation bereits weitestgehend erkundet sind und das diesbezügliche Potential ausgeschöpft scheint, so befindet sich die Forschung hinsichtlich der Realwelt-Implementierung sowie der Validierung von MIMO-UWB-Lösungen nach wie vor in den Kinderschuhen. Diese Tatsache ist zum Anlass genommen worden, in dieser Arbeit den Fokus zu setzen auf die Entwicklung und die Validierung geeigneter MIMO-Ansätze zur Kurzstrecken-Hochgeschwindigkeits-UWB-Kommunikation aus der Perspektive effizienten Algorithmendesigns, Implementierungs-beschränkungen sowie Nicht-Idealitäten in der HF Hardware. Die Zielsetzung dieser Arbeit ist daher das Design von Systemarchitekturen und fortgeschrittenen Algorithmen, welche die Anforderungen nach hohem Durchsatz und Performance bei künftigen UWB-Anwendungen im Bereich Wireless Personal Area Networks (WPANs) bedienen werden.

Fortgeschrittenes Algorithmen- und Systemdesign bedarf grundsätzlich aufwendiger Testreihen und Messungen mittels einer Hochleistungs-Prototypen-Plattform, die in der Lage ist, Abstraten von mehreren Gigahertz zu beherrschen und ferner über parallele HF- und Basisband-Verarbeitungswege verfügt. Damit Verbesserungen der Spektraleffizienz und höchste Datenraten in der UWB-Kommunikation nachgewiesen werden können, ist eine Offline-MIMO-UWB-Forschungsplattform entwickelt worden, welche bis zu 4×4 MIMO-Konfigurationen unterstützt. Diese flexible Plattform ermöglicht darüber hinaus die präzise Erforschung HW-spezifischer Effekte im RF-Frontend sowie nicht-ideale Synchronisierung in Zeit und Frequenz über das Real-Air-Interface. Abschließend erlaubt der modulare Aufbau dieser Plattform eine effiziente Validierung des Hardware-in-the-Loop-Leistungsverhaltens sowie eine Evaluierung des Ressourcenverbrauchs als Grundlage für eine zukünftige Halbleiter-Implementierung dedizierter MIMO-UWB-Lösungen und den damit verbundenen Ressourcennutzung.

Abstract

Multiple-Input Multiple-Output (MIMO) systems have been widely considered a viable solution to overcome the current limits in wireless communication. The application of Ultra-wideband (UWB) to indoor environments, with the rich energy scattering and large angular spreads of the multipath channel, provides an ideal scenario for MIMO. By unclosing an additional degree of freedom for communication, multiple antennas at the transmitter and/or receiver can effectively turn multipath propagation, considered initially a drawback in wireless communications, into an advantage so as to linearly increase the capacity of the system, or improve its coverage and robustness in terms of error probability.

While the benefits of MIMO have been widely studied and exploited in broadband MIMO-OFDM wireless communications, the field of real-world implementation and verification of multiple antenna UWB solutions is still in its infancy. In this thesis, we have therefore focused on developing and validating suitable MIMO approaches for short-range, high-speed UWB communications from the perspective of low-complexity algorithm design, implementation-level constraints and RF frontend imperfections. Aim of this work is thus the design of system architectures and advanced algorithms satisfying the high throughput and performance requirements of emerging UWB applications in Wireless Personal Areas Networks (WPANs).

The advanced algorithm- and system design requires inherently the extensive test and measurement via a high-performance prototyping platform, able to cope with sampling rates of multiple Gigahertz and featuring parallel RF- and baseband processing branches. In order to verify the enhancements in spectral efficiency and potentially highest data rates for UWB communications, we have therefore developed an offline MIMO-UWB test-bed supporting up to 4×4 MIMO configurations. This flexible platform further enables the investigation of HW specific impairments in the RF frontend, as well as aspects of imperfect synchronization in time and frequency over the real-air interface. Finally, its modular setup allows for efficient hardware-in-the-loop performance validation and resource evaluation of dedicated MIMO-UWB solutions as basis for their future silicon implementation and utilization.

Schlagwörter / Keywords

Ultra-Wideband (UWB), Multiple-Input Multiple-Output (MIMO), Multiband OFDM

Contents

List of Abbreviations	x
Chapter 1 Introduction.....	1
1.1 Goals and Motivation.....	2
1.2 Outline and Contributions	3
Chapter 2 Background of Ultra-Wideband Wireless Communications.....	5
2.1 Evolution and State of the Art	5
2.2 Worldwide Activities on UWB Regulation	6
2.3 Multi-Band Orthogonal Frequency Division Multiplexing.....	7
2.3.1 Design Criteria and Performance Requirements	8
2.3.2 Mathematical Model of the MB-OFDM Signal.....	9
2.3.3 System Architecture.....	10
2.4 UWB Channel Modelling.....	12
2.4.1 Physical Characteristics of the UWB Channel	13
2.4.2 Correlation-based Double-directional Stochastic MIMO-UWB Channel Model	14
Chapter 3 Multiple-Input Multiple-Output Technology	20
3.1 MIMO-OFDM System Model	22
3.2 Multiple Antenna Techniques at the Transmitter.....	22
3.2.1 Spatial Multiplexing	22
3.2.2 Dual Mode Transmission	23
3.2.3 Diversity Schemes in Space, Time and Frequency	24
3.2.4 Antenna Subset Selection	27
3.3 MIMO Combining at the Receiver	27
3.3.1 Linear Receivers	27
3.3.2 Successive Interference Cancellation for V-BLAST Architectures	28
3.3.3 Close-to-ML Efficient MIMO Processing	29
3.3.4 MIMO Decoding for Diversity Schemes	30

Chapter 4 System Design of a MIMO MB-OFDM System.....	32
4.1 Concept of a Modular MIMO-UWB System	32
4.1.1 System Level Considerations	34
4.1.2 System Parameters and Frame Structure	38
4.2 Basic Signal Processing Blocks	44
4.2.1 Robust Synchronization of Time-Frequency Interleaved Signals	44
4.2.2 Synchronization Performance.....	50
4.2.3 Channel Estimation in Frequency-Hopping MIMO-UWB Systems.....	53
4.2.4 Modelling, Impact and Compensation of Impairments	56
4.3 Conclusions	63
Chapter 5 Advanced Deployment Schemes for MIMO MB-OFDM.....	65
5.1 Deployment Scenarios and Performance Requirements.....	66
5.2 Linear MMSE Receiver with QR-Decomposition.....	67
5.3 Ordered SIC Receiver with MMSE-based Sorted QR-Decomposition	71
5.3.1 Sorted MMSE-based QR Decomposition	72
5.3.2 Ordered SIC Detection with Back Substitution	74
5.4 Orthogonal STF Decoder with Scaled LLR Demodulation	76
5.4.1 MIMO Coding Framework.....	77
5.4.2 MIMO Combining.....	78
5.4.3 Bitwise LLR Demodulation	80
5.5 Differential Algorithm for Interference Detection and Mitigation	83
5.6 On the Implementation Complexity of MIMO MB-OFDM	87
5.6.1 Transceiver Architecture, Power Consumption and Silicon Area	87
5.6.2 RF Frontend	88
5.6.3 Efficient Multichannel FFT Processing	88
5.6.4 FPGA Implementation Complexity of the Proposed MIMO Algorithms	89
5.7 Conclusions	90

Chapter 6 Performance Verification via the MIMO-UWB Test-bed	92
6.1 Experimental MIMO-UWB Test-bed	93
6.1.1 General Set-up and Verification Environment	93
6.1.2 Transmitter	94
6.1.3 Receiver	96
6.1.4 Data and Control Interfaces	97
6.1.5 Measurement and Verification Methodology	98
6.2 Application-specific MIMO-UWB Channel Measurements	98
6.2.1 Enhancements in Spectral Efficiency	99
6.3 Performance Verification in Indoor Environment	103
6.4 Conclusions	110
Chapter 7 Summary and Conclusions	111
List of Figures	113
List of Tables	117
Bibliography	118
Own Contributions	124
Curriculum Vitae	125

List of Abbreviations

ADC	Analog-to-Digital Converter
AGC	Automatic Gain Control
AWGN	Additive White Gaussian Noise
BB	Base Band
BER	Bit Error Rate
BS	Back Substitution
CFO	Carrier Frequency Offset
CIR	Channel Impulse Response
CP	Cyclic Prefix
CSI	Channel State Information
DAA	Detect-And-Avoid
DAB	Digital Audio Broadcasting
DAC	Digital-to-Analog Converter
DFT	Discrete Fourier Transform
DoA	Direction of Arrival
DoD	Direction of Departure
DSP	Digital Signal Processor
DVB-T	Digital Video Broadcasting - Terrestrial
EGC	Equal Gain Combining
EIRP	Equivalent Isotropic Radiated Power
EUWB	Co-Existing Short Range Radio by Advanced Ultra-Wideband Radio Technology
FCC	Federal Communications Commission
FDS	Frequency Domain Spreading
FER	Frame Error Rate
FFI	Fixed-Frequency Interleaving
FFT	Fast Fourier Transform
FPGA	Field Programmable Gate Array
GUI	Graphical User Interface
I/Q	In-Phase/Quadrature
ICI	Inter-Carrier Interference
IDFT	Inverse Discrete Fourier Transform
IEEE	Institute of Electrical and Electronics Engineers
IF	Intermediate Frequency
IFFT	Inverse Fast Fourier Transform
INR	Interference-to-Noise Ratio
IR	Impulse Radio
ISI	Inter-Symbol Interference
LAN	Local Area Network

LDC	Low Duty Cycle
LLR	Log Likelihood Ratio
LNA	Low Noise Amplifier
LO	Local Oscillator
LOS	Line of Sight
LSE	Least-Square Estimation
LTE	Long Term Evolution
MAC	Media Access Control Layer
MB-OFDM	Multi-Band Orthogonal Frequency Division Multiplexing
MF	Matched Filter
MIMO	Multiple-Input Multiple-Output
ML	Maximum Likelihood
MM	Matrix Multiplication
MMSE	Minimum Mean Square Error
MRC	Maximum Ratio Combining
MS	Mobile Station
MSE	Mean Square Error
NLOS	Non-Line of Sight
PAPR	Peak-to-Average Power Ratio
PDP	Power Delay Profile
PHY	Physical Layer
PSD	Power Spectral Density
RF	Radio Frequency
RX	Receiver
SIC	Successive Interference Cancellation
SIMO	Single-Input Multiple-Output
SINR	Signal-to-Interference-plus-Noise Ratio
SISO	Single-Input Single-Output
SMUX	Spatial Multiplexing
SNR	Signal-to-Noise Ratio
SQRD	Sorted QR Decomposition
STBC	Space-Time-Block Coding
STFC	Space-Time-Frequency Coding
SVD	Singular Value Decomposition
TDS	Time Domain Spreading
TFI	Time-Frequency Interleaving
ToA	Time of Arrival
ToD	Time of Departure
TX	Transmitter
UWB	Ultra-Wideband

V-BLAST	Vertical Bell Laboratory Space Time
VHDL	Very High Speed Integrated Circuit Hardware Description Language
WiMAX	Worldwide Interoperability for Microwave Access
WLAN	Wireless Local Area Network
WPAN	Wireless Personal Area Network
ZF	Zero Forcing
ZP	Zero Padding
ZPS	Zero-Padded Suffix

Chapter 1

Introduction

Nowadays, wireless communications have become omnipresent, pervading deep into almost every part of our social and professional life. In the past few decades, the world of wireless connectivity has witnessed the birth of numerous novel applications with ever-increasing demands for highest data rates, quality of service (QoS), extended coverage and flexible networking. The technological advances in chip manufacturing and the exponential increase in transistor count of Integrated Circuits (ICs), which according to Moore's Law double in performance every 18 months (originally stated every 2 years) gave rise to rapid developments in the consumer electronics and mobile telecommunications industry. Driven by the advances in industry and information theory, hundreds of short-range, high-speed connectivity and networking scenarios have emerged in the field of Wireless Local/Personal Area Networks (WLAN/WPANs). Prominent examples of such enabling technologies in WLAN/WPAN are the IEEE 802.11 standard family (WiFi), IEEE 802.15.1 (Bluetooth), IEEE 802.15.4 (ZigBee), or RFID, to name a few. Their served applications range from broadband internet access at home or the office, over PC/laptop wireless connectivity to peripherals like hard drives, monitors, printers, cameras, etc., down to "smart home" networking and sensor data exchange between household devices.

In the meanwhile, meeting the harsh application requirements of high-speed, enhanced performance, long coverage and battery life has become a real challenge for existing standards operating in e.g. the license-free Industrial, Scientific and Medical (ISM) bands. In fact, the almost exponential increase in data rates in the last two decades has been predicted and confirmed by Edholm's law of bandwidth. As the aforementioned standards are still limited in the resource utilization by the available bandwidth, the allowed transmit power as posed by regulators, or the power consumption constraints of hand-held devices, the need of a novel technology able to overcome these bottlenecks in today's wireless communications and to boost data rates, but also enhance coverage and link quality, has become obvious. This observation is truly conform with the famous Shannon's capacity theorem, which states that the maximum achievable error-free information data rate in an additive white Gaussian noise (AWGN) channel is directly proportional to the signal bandwidth, and depends logarithmically on the Signal-to-Noise ratio in the system. Straightforward conclusion is that the most efficient way of reaching highest data rates would be by increasing the signal bandwidth. Later on, Telatar and Foschini proved in [1][2] that for multiple

antenna systems the channel capacity C is further linearly proportional to the minimum of the number transmit and receive antennas (N_T and N_R) being deployed, i.e.

$$C = \min\{N_T, N_R\} B \log_2 \left(1 + \frac{P_s}{P_n} \right),$$

where B stands for the signal bandwidth, and P_s / P_n is the ratio of the signal to noise power.

These fundamental findings paved the way for the development of both Multiple-Input Multiple-Output (MIMO) and Ultra Wideband (UWB) technologies that possess the huge potential to reach the Shannon's capacity limit and meet the demands of future short-range high-speed communication systems. Indeed, UWB is mainly applicable to indoor WPAN/WBAN environments, in which the dense multipath propagation leads for high data rates to generally detrimental Inter Symbol Interference (ISI). A widely known approach for turning this drawback in to a benefit is to exploit such rich scattering environments by the use of multiple antennas, at one or both sides of the communication link.

Although MIMO had initially been considered prohibitively expensive and therefore impractical for commercial deployment, the final breakthrough of MIMO was triggered by its adoption in the first drafts of the IEEE 802.11n specification. In fact, the targeted data rates at that time were unable to cope with the higher order modulation schemes because of too expensive analog RF frontends, whereas MIMO offered the possibility to close this gap by linearly increasing the system capacity through spatial multiplexing. Further on, multiple antennas at the TX and/or RX were able to improve the robustness of the system in terms of error propagation and to extend its coverage by means of smart diversity schemes, beamforming and efficient combining techniques. More details on the benefits of UWB and MIMO, and the combination of both technologies will be given in the chapters to follow.

1.1 Goals and Motivation

The advantages of MIMO technology have been widely explored and realized in broadband MIMO-OFDM wireless communications, whereas research on the real-world implementation and verification of multiple antenna UWB solutions is still at a very early stage. Even though the field of UWB communications has attracted a lot of research interest within the past years, the combination of MIMO and UWB has been studied mostly analytically, whereas the area of MIMO-UWB design, low-complexity implementation and verification via prototyping and extensive measurements is not yet fully explored. In this thesis, we have therefore focused on developing and validating suitable MIMO approaches for short-range, high-speed UWB communications from the perspective of low-complexity algorithm design, implementation-level constraints and real-world imperfections.

Aim of this work is thus the design of system architectures and advanced algorithms satisfying the high throughput and performance requirements of emerging UWB applications in WPANs. The development of application-aware algorithms for link quality improvement, range extension, and interference mitigation has been a major objective of this work in order to exploit the benefits offered by the use of multiple antenna technology.

The validation and proof of concept of the advanced algorithm- and system designs however require extensive tests and measurements via a high-performance prototyping platform, which is able to cope with sampling rates of multiple Gigahertz and features parallel RF- and baseband processing branches. This necessity has motivated us to develop an offline MIMO-UWB test-bed for up to 4×4 MIMO configurations that can support the experimental evaluation of the potential enhancements in spectral efficiency (and highest data rates) and performance of UWB communications, including the effects of real-world propagation constraints and hardware imperfections.

1.2 Outline and Contributions

The thesis is structured as follows. In Chapter 2, the background and evolution of Ultra Wideband wireless communications, as well as summary of the worldwide regulation and standardization activities are provided. Next, we describe the target Multiband OFDM (MB-OFDM) technology and the underlying signal model based on the ECMA-368 PHY/MAC layer specifications [3]. Subsequently, the propagation environment is characterized, analyzed and modelled using a double-directional correlation-based stochastic approach. Chapter 3 gives a general overview of multiple antenna systems and efficient MIMO processing techniques at both the transmitter and receiver side, including spatial multiplexing, dual mode and transmit diversity schemes.

The system design and modular concept of the proposed MIMO-UWB MB-OFDM system is elaborated in Chapter 4. Main contributions of this chapter are:

- Design of a modular system featuring multiple antennas at both sides of the link, an offline MIMO-UWB test-bed and HW-in-the-loop MIMO-UWB simulation environment.
- Link budget analysis for HDR and VHDR modes of operation in AWGN and CM1 channels.
- Specification of ECMA-368 standard conform system parameters, frame structure and MIMO preamble design for VHDR mode.
- Design and implementation of robust synchronization algorithms for timing- and TFC acquisition, including evaluation of synchronization performance.
- Framework for modelling, estimation and compensation of RF impairments, including evaluation of the impact of Phase Noise (PN), I/Q-imbalance and Carrier Frequency Offset (CFO) in the receiver down-conversion part.

The technology description in Chapter 5 provides advanced algorithm design and implementation notes for low-complexity multiplexing-, diversity- and antenna selection techniques deploying multiple antennas. Main contributions of Chapter 5 are:

- Deployment of advanced MIMO combining schemes for high-speed MIMO-UWB communications
- Deployment and validation of linear MMSE receiver based on QR-Decomposition (QRD) for MIMO MB-OFDM.
- Deployment and validation of MMSE-based Ordered Successive Interference Cancellation (OSIC) receiver with Sorted QR-Decomposition (SQRD) for MIMO MB-OFDM.
- Deployment and validation of orthogonal Space-Time-Frequency (STF) detector with scaled Log-Likelihood Ratio (LLR) demodulation, including provision of coding framework at the transmitter.
- Development and verification of a differential algorithm for interference detection and mitigation based on the Detect-And-Avoid (DAA) approach.
- Experimental evaluation and validation of the above schemes via the offline MIMO-UWB test-bed.
- Provision of summary notes on the FPGA implementation complexity and resource utilization of the proposed algorithms.

Chapter 6 describes the setup of an experimental offline MIMO-UWB test-bed for test and verification of the proposed algorithms and system design, and provides validation results for selected indoor scenarios. Main contributions in this chapter are:

- Design and setup of an experimental offline 4×4 MIMO-UWB test-bed for test and verification of selected multiple antenna schemes.
- Real-world examination of system performance of selected MIMO approaches, including investigation of the impact of RF frontend imperfections and their compensation.
- Analysis and verification of the achievable MIMO capacity and diversity gains via the test-bed.
- Performance evaluation of MIMO systems deploying dual-polarized antennas and Dual Mode transmission.

In Chapter 7, we summarize the findings of this thesis, draw final conclusions and provide outlook for future research in the field of MIMO-UWB wireless communications.

Chapter 2

Background of Ultra-Wideband Wireless Communications

2.1 Evolution and State of the Art

Over the past decade, the research on Ultra Wideband (UWB) technology has gained remarkable momentum as response to the ever-increasing demand for high-speed connectivity among consumer electronics, personal computing and hand-held mobile devices operating within Wireless Personal Area Networks (WPANs). The history of UWB however goes late back to the year 1901 and the experiments of the first radios, as Guglielmo Marconi's transatlantic sparkle transmissions used in fact ultra-wideband signals.

Later on, with the invention and development of stable and accurate oscillator circuits in the early 1930s, the communication paradigm drastically changed to using single frequencies, allocated to licensed services for multiple of billions of dollars. This gave rise to the development of numerous single-carrier standards in the area of mobile communications, aeronautical, radar, and military applications.

The research on 'intentional' Impulse Radio UWB (IR-UWB) started back in the 1960s, owing to the pioneering work on the generation and reception of very short pulses, occupying the available bandwidth of multiple GHz [4]. However, the single band approach faces the challenge of designing a low complexity receiver able to capture sufficient energy in multipath environments with strong fading. Indeed, building RF analog circuits that operate at GHz-frequencies is still rather demanding for state-of-the-art receiver front-ends and analog circuits [5].

The landmark ruling of the Federal Communications Commission (FCC) in 2002 [6] as well as the developments of advanced multi-carrier standards such as those deployed in WLAN (e.g. IEEE 802.11 family) paved the way for a slightly revised definition of the underlay nature of UWB. In fact, license-exempt communications in WPAN have been allowed for a UWB signal defined by an absolute bandwidth of at least 500 MHz, or a relative 10-dB bandwidth greater or equal than 20% of its center frequency. The FCC ruling thus poses no direct limitation to the signal form, opening the door to modulation techniques other than impulse radio, e.g. DSSS or OFDM-based transmission.

In compliance with these FCC regulations, and in order to circumvent the inherent challenges of IR-UWB, multiband UWB schemes have been proposed, in which the total allocated spectrum of 7.5 GHz is divided into non-overlapping sub-bands of at least 500 MHz. The advantage over single-band transmission is that by interleaving the symbols across different sub-bands the information can be

processed over a much smaller bandwidth. This allows for significant reduction in the overall design complexity, greater spectral flexibility and worldwide compliance with existing and emerging UWB technologies. Since a Multiband UWB system enables an independent control of portions of the emitted spectrum, it can better coexist with narrowband (NB) systems from licensed services on adjacent or even co-located frequency bands, e.g. military radar, LTE, 802.11 standard family or WiMAX, and is therefore able to better comply with the UWB spectral mask posed by regulators.

2.2 Worldwide Activities on UWB Regulation

Owing to the underlay nature of the UWB technology, its signal power is spread across frequency bands already occupied by licensed services. With the allocation of unlicensed spectrum use for UWB devices, the FCC decision rules [6] allowed an unprecedented coexistence between those two players. Although the allocated spectral masks lie as low as the unintentional power emission levels for all radiators, incumbent spectrum holders are still rather concerned with having potential interferers in their bands of operation. These concerns have caused a lot of controversy and discussion across regulators and industry, preventing from allowing the harmonized use of UWB device across the world. Figure 2.1 depicts the current status of worldwide UWB regulation activities.

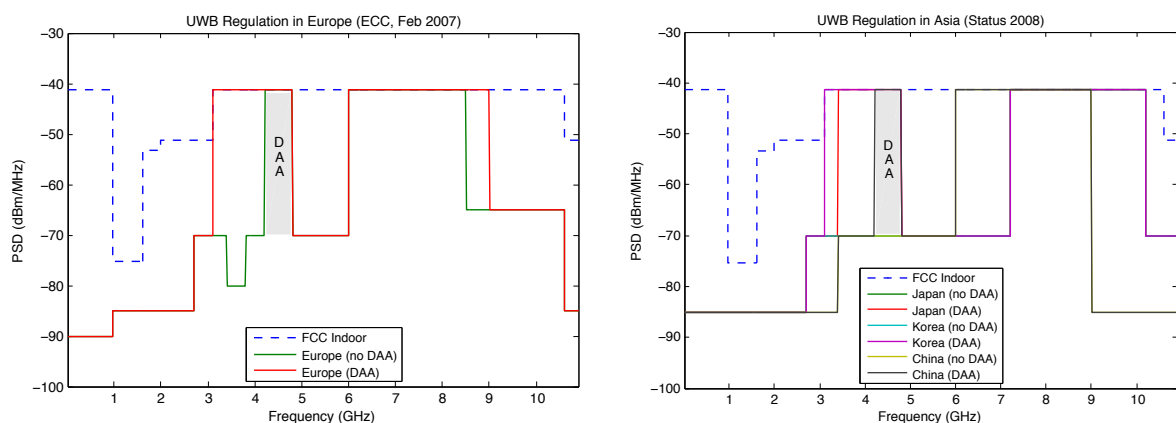


Figure 2.1: Worldwide UWB power emission limits.

In contrast to the FCC spectral mask, which allows indoor UWB PSD emissions as high as -41.3 dBm/MHz, regulators in Europe and consequently the Asian countries impose the requirement of additional interference mitigation techniques, via e.g. Detect-And-Avoid (DAA) mechanisms, to protect incumbent military radar, WiMAX, 4G mobile, and radiolocation services. In fact, due to the prohibitively low levels set in case of no DAA being applied, worldwide operation of UWB devices becomes viable only in Band Group 6 (7392 MHz to 8976 MHz).

2.3 Multi-Band Orthogonal Frequency Division Multiplexing

In multipath environments with rich scattering, the transmitted signal suffers deep fades in power level resulting in loss of information at the receiver side. To circumvent the fading problem and efficiently capture the multipath energy, the Multiband Orthogonal Frequency Division Multiplexing (MB-OFDM) technique has been adopted for UWB communications to modulate the information on each sub-band by transmitting multiple carriers in parallel over the frequency domain [7]. Common OFDM-based systems combat the multipath effects by introducing a sufficiently long Cyclic Prefix (CP) at the beginning of each symbol to convert the linear convolution with the channel impulse response into a circular one and thus to ensure ideal detection by the FFT at the receiver. Along with being efficient in capturing the multipath energy at the receiver, OFDM systems provide a simple method for frequency domain equalization, which is considered a significant challenge for high-rate single-carrier transmissions [8]. The resulting transmission scheme, called MB-OFDM UWB, shares the well-proven advantages of a multi-carrier scheme. In contrast to conventional OFDM transmission however, where the symbols are continually sent on one and the same band, MB-OFDM systems apply frequency hopping so that the symbols are interleaved over different sub-bands, i.e. in both time and frequency. The multiple access of different users (or adjacent piconets) has been enabled by careful design of the frequency-hopping patterns in order to minimize the multi-user interference.

A UWB Time-Frequency Interleaved OFDM (TFI-OFDM) PHY specification that has been initially proposed by Anuj Batra et al. within the IEEE 802.15.3a standardization task group TG3a deploys fast frequency hopping of OFDM-modulated symbols across 528 MHz wide sub-bands [9]. This proposal was later adopted by the newly formed WiMedia Alliance [10], and issued with slight modifications as an international ECMA-368/369 PHY/MAC standard (later also as ETSI TS 102 455 and ISO/IEC 26907:2007 standard) [3].

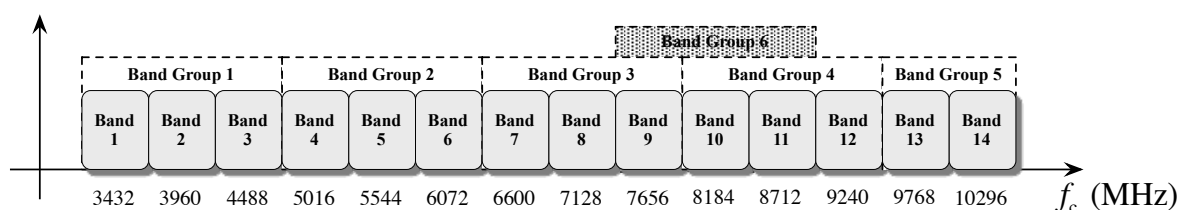


Figure 2.2: WiMedia frequency band plan

As shown in Figure 2.2, the whole 7.5 GHz wide UWB spectrum is subdivided into 14 sub-bands of 528 MHz bandwidth each, with three adjacent bands being further combined into Band Groups (BG), except for BG5 which contains only two bands. Band Group 6 is envisioned to provide worldwide support for next-generation WiMedia devices. This enables multiple user access and high data rate communication capabilities of 53.3 Mbps up to 480 Mbps (the current WiMedia PHY specification

foresees data rates of up to 1024 Mbps using LPDC), depending on various puncturing patterns and spreading factors.

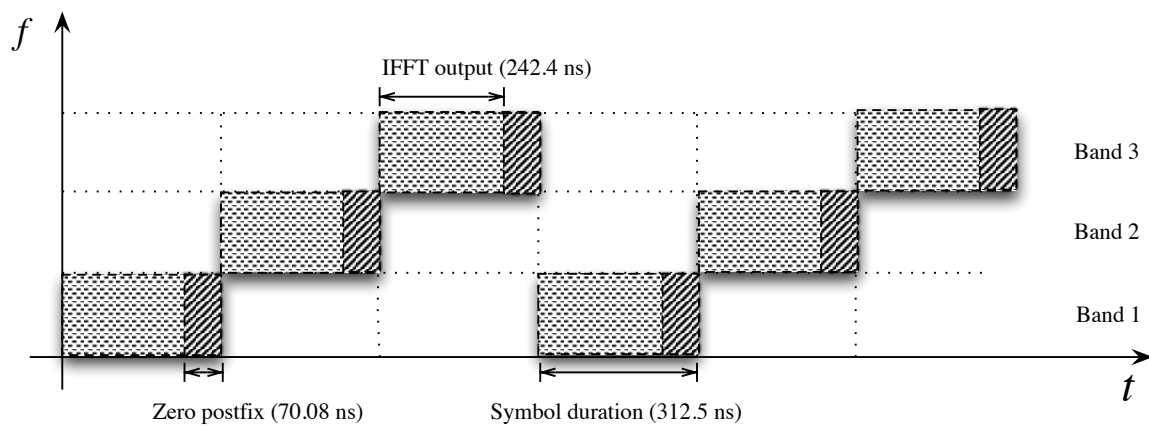


Figure 2.3: Time-frequency interleaving in MB-OFDM

An example of how the data is transmitted across the different sub-bands using time-frequency interleaving is given in Figure 2.3. The whole MB-OFDM symbol consists of the actual user data, a Zero Postfix (ZP) of length 60.6 ns and a Guard Interval (GI) of 9.5 ns after each symbol to reduce the complexity of the receiver and enable fast switching across the frequency sub-bands.

2.3.1 Design Criteria and Performance Requirements

The choice of core parameters for the MB-OFDM system described above depends on the emerging need for high data-rate, low-cost and low-power communications within the personal operating space. To enable fast wireless connectivity, low-cost implementation and high Quality of Service (QoS) within WPANs, the designed MB-OFDM system has to meet several technical requirements to form the basis of the standard.

The key criteria that determine the optimum parameters and design of the MB-OFDM in such High Data Rate (HDR) scenarios are performance, complexity and system flexibility. The desired system performance, i.e. robustness in severe multipath channels, directly influences the choice of modulation type, receiver architecture and complexity. The suitability of OFDM as modulation to effectively combat fading and collect multipath energy with low computational complexity implies the need to define important parameters such as FFT-size, length of the ZP, constellation size, coding scheme or spreading factors.

Another important criteria in the design of the HDR system is the optimal operating bandwidth. It impacts not only the link budget and thus the overall system performance, but also the TX/RX architecture and speed of the baseband signal processing. A carefully chosen frequency band of operation can therefore significantly alleviate the technical requirements for the channel pre-select filters, LNA, DACs, ADCs, mixers, and digital processing blocks. In order to reduce the overall

complexity, implementation costs and power consumption, a bandwidth as close as possible to the minimum 500 MHz specified by the FCC has been favoured [7].

Regarding the choice of FFT-size in an OFDM-based system, it should be noted that since this block typically accounts for 25% of the RX digital baseband complexity, a too big size is often prohibitive. Moreover, increasing the FFT-size reduces the frequency spacing between the subcarriers, causing errors in frequency synchronization to become destructive. On the other side, a too small size increases the overhead due to the ZP and degrades the range.

The ZP length on its turn determines the amount of multipath energy that could be captured by the RX, but introduces an overhead and thus reduces the system throughput. Since any multipath energy not captured during the ZP causes Inter-Symbol Interference (ISI), the ZP length including the Guard Interval needed for fast TFI switching has been set to 1/4 of the FFT length to minimise the ISI while keeping the total collected multipath energy at maximum. Note that in contrast to the original proposal of the IEEE 802.15.3a, the ECMA-368 PHY standard employs a ZP instead of a CP, as the former is reported to reduce the Peak-to-Average-Power Ratio (PAPR) of the transmitted signals and thus relaxes the requirements for the power amplifiers and needed back-offs and dynamic range of the DACs at the TX.

2.3.2 Mathematical Model of the MB-OFDM Signal

In the following we present the mathematical model of a frequency-hopping MB-OFDM signal.

The discrete-time signal during the m -th MB-OFDM symbol period can be described by

$$s_m[n] = \frac{1}{\sqrt{N}} \sum_{k=-N/2}^{N/2-1} d[k] e^{j2\pi kn/N} p_N[n], \quad (2.1)$$

$$\text{with } p_N[n] = \begin{cases} 1/\sqrt{N} & 0 \leq n \leq N \\ 0 & \text{otherwise} \end{cases}$$

being a single rectangular pulse of unit energy, and $d[k]$ standing for the complex data sub-carriers modulated to the subcarrier intermediate frequency $2\pi k / N$ using an IFFT of size N .

After insertion of the ZP and digital-to-analog conversion, the baseband signal $s_m(t)$ is further up-converted to the corresponding RF center frequency f_c^m , resulting in the real valued signal $s_{\text{RF}}(t)$ to be transmitted over the wireless channel

$$s_{\text{RF}}(t) = \text{Re} \left\{ \sum_{m=0}^{N_s-1} s_m(t - mT_{\text{sym}}) e^{j2\pi f_c^m t} \right\}, \quad (2.2)$$

where $s_m(t) = 0$ for $t \notin [0, T_{\text{sym}})$, N_s is the total number of transmitted symbols within a frame, and $T_{\text{sym}} = T_{\text{FFT}} + T_{\text{ZP}}$ the duration of the MB-OFDM symbol.

The center frequency f_c^m in each time slot m is controlled by the TFI block according to the specified time-frequency code (TFC) of transmission. The proposed ten TFCs for BG 1 have been designed to minimize the interference between collocated networks/piconets, and can therefore be interpreted as logical channels in the frequency domain used to enable multiple user access in the system. For the m -th transmitted symbol, the center frequency of the corresponding sub-band of transmission can be derived from the band ID $l_m \in [1 \dots 14]$ of a given TFC $\{l_1, l_2, \dots, l_{N_{\text{TFC}}}\}$ as [3]

$$f_c^l = 2904 + 528l_{\text{mod}(m, N_{\text{TFC}})+1} \quad [\text{MHz}], \quad (2.3)$$

where $B = 528$ is the system bandwidth in MHz, $N_{\text{TFC}} = 6$ is the length of the TFC, and $\text{mod}(\cdot)$ denotes the modulo operation.

2.3.3 System Architecture

The *transmitter architecture* of the proposed MB-OFDM UWB system is quite similar to that of a traditional OFDM system, the main difference being the use of a time-frequency interleaver (TFI) to control the frequency hopping between sub-bands.

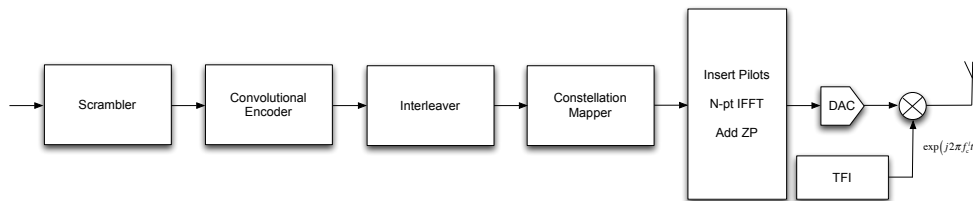


Figure 2.4: MB-OFDM TX architecture

Figure 2.4 shows the block diagram of an example TX architecture of the MB-OFDM UWB system. At the input of the system, binary payload data are first scrambled and then passed through an industry-standard 1/3 rate convolutional encoder with generator polynomials $g_0 = 133_8$, $g_1 = 165_8$ and $g_2 = 171_8$ in octal notation. The different code rates (1/2, 5/8 and 3/4) are derived from the 1/3 base rate by applying puncturing according to specified patterns. By omitting certain bits at the transmitter side ("bit-stealing") and subsequent insertion of dummy zeros at the receiver decoder, the code rates and thus the system data rate and overall performance can be adjusted according to the mode of transmission and desired quality of service. For diversity purposes, further reduction of data rate can be obtained by redundant transmission of data on another sub-band in a following

time slot (time-domain spreading), or by forcing a conjugate symmetric input of the IFFT block (frequency-domain spreading).

Prior to modulation, the coded bit stream is interleaved in three stages (symbol-, tone- and cyclic-shift interleaver) to provide additional robustness against burst errors.

In the following stage, the coded and interleaved bit stream is fed into a QPSK Gray-coded (or DCM for data rates exceeding 200 Mbps) constellation mapper. The output complex symbols are now grouped in blocks of 100 tones, which are further combined with the evenly spaced pilot tones, in addition to guard- and zero tones near the band edges, in order to enable robust coherent detection against CFO and phase noise impairments at the receiver. The resulting 128 tones are then introduced in parallel to the actual OFDM modulation block. The latter basically performs the Inverse Discrete Fourier Transform (IDFT) on the vector of complex tone coefficients, and is often implemented in practice by the computationally efficient Inverse Fast Fourier Transform (IFFT) of a power-of-two size N .

Due to the properties of the IDFT, the sub-carriers comprising the MB-OFDM symbol have a sinc-function shape and partly overlap in the frequency domain. This significantly increases the spectral efficiency of the modulation scheme as compared to conventional non-overlapping multi-carrier systems, but implies that the separation of the different tones at the RX can not be done by BP filtering.

The discrete-time domain output sequence is expanded by inserting a zero-padded postfix ZP, including a guard interval (GI) to allow for fast band switching. Similar to the CP, the ZP aims to combat the dispersion effects of the channel and collect maximum multipath energy while reducing the crest factor of the signal waveform. Since the addition of a ZP increases the overhead in the system, the ZP length is an important design parameter, which must be chosen in a trade-off between robustness against ISI and effective data rate. The GI on the other side ensures sufficient time (9.5 ns) for the frequency synthesizers at both TX and RX to switch between the different sub-bands. The baseband signal is directly converted to the desired RF center frequency provided by the Time-Frequency Interleaving (TFI) block during each symbol slot.

The *receiver architecture* of the proposed MB-OFDM system is based on the so-called Zero-IF topology, in which the RF signal is directly down-converted to baseband, thus minimizing the number of signal processing stages and the overall receiver power consumption [11]. Through complex mixing and subsequent low-pass filtering in the baseband, this architecture is able to suppress nearby interferers, remove the undesired image of the signal and select the desired channel. Despite eliminating the need of Intermediate Frequency (IF) stages and bulky off-chip Image Reject filters, the Zero-IF receiver introduces the challenges of DC-offsets, 1/f-noise, LO leakage and I/Q imbalance.

To overcome these challenges, careful layout design, advanced digital signal processing and/or alternative (e.g. Low-IF) receiver architectures may be considered.

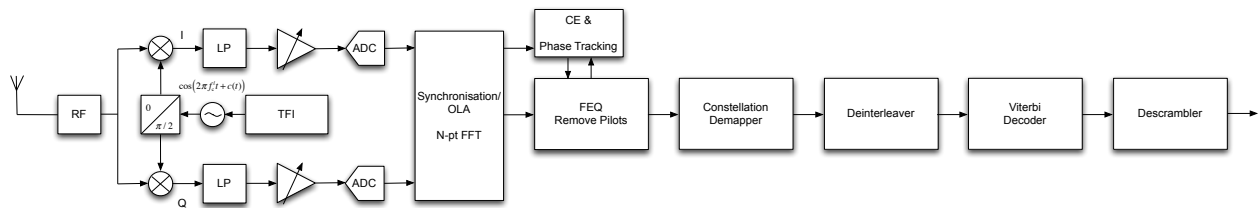


Figure 2.5: MB-OFDM RX architecture

In a MB-OFDM Zero-IF receiver, as shown in Figure 2.5, the received signal $y(t)$ behind the antenna is first passed through the RF analog front-end, consisting of a BP preselect filter and a Low Noise Amplifier. The former serves to suppress out-of-band energy, pre-select the desired frequency band and thus partially reject higher noise frequency components and image band signals. The latter is used to amplify extremely weak signals without introducing additional distortions. The output of the RF block is then directly down-converted to baseband in In-phase (I) and Quadrature (Q) branches. The resulting I- and Q components are further passed in parallel through an LP anti-aliasing filter and an analog-to-digital converter (ADC). The discrete-time signal $y[n]$ is then introduced in parallel to a coarse time/frequency synchronization block, which has to determine the arrival of a packet, as well as to set the boundary of each frame and the proper window for the following FFT operation. After channel estimation and demapping, the information tones are equalized, fed to a constellation demapper, and finally processed by the deinterleaver and channel decoder in the reverse order of transmission.

We next describe the common characteristics of the UWB wireless channel, and provide analytical description of the correlation-based double-directional stochastic channel modelling approach used to verify the developed MIMO schemes in a MATLAB simulation environment.

2.4 UWB Channel Modelling

The accurate design, analysis and validation of any UWB communication scheme require proper characterisation of the propagation environment within the envisioned deployment scenarios. Due to their huge bandwidth occupancy exceeding multiples of GHz, UWB systems need to account for and potentially benefit from the fine time resolution of the arriving multipath components. The rich scattering present in indoor environments further provides an ideal use case for multiple antennas: by opening independent data pipes for capacity improvement; or by offering unique spatial signatures to enable transmit diversity schemes and eventually enhance the system coverage, robustness in terms of error probability, and resilience to interference.

In the following, we briefly describe the modelling and measurement scenarios of the propagation environment used to validate the developed algorithms and system designs described in this work. After a brief overview of the physical properties of the UWB channel, we review the common approaches used to model the large- and small-scale fading characteristics, with special focus on the induced correlation in time-, frequency- and spatial domain when deploying multiple antennas.

For the purpose of system design and algorithm verification, the characteristics of the MIMO-UWB channel have been reflected in three ways: for the majority of algorithm design and verification tasks performed in MATLAB, we adopt the correlation-based stochastic MIMO-UWB channel model described in [12]. We further evaluate the system performance using selected channel sounding data from the measurement campaigns described in [13]. Finally, we verify the proposed MIMO detection algorithms by means of the 4×4 offline MIMO-UWB test-bed over the real-air interface and dedicated baseband signal processing on a Xilinx Virtex6 FPGA platform.

2.4.1 Physical Characteristics of the UWB Channel

In contrast to narrowband channels, where the signal bandwidth rarely exceeds 20 MHz, outdoor and indoor measurement campaigns witnessed several phenomena resulting from the UWB waveform. Due to the large number of scattering objects and obstacles present in indoor environments, the number of resolvable paths, width of the angular spreads, and inter-arrival statistics of the multipath components (MPCs) change significantly as compared to narrowband channels. In particular, as the UWB receiver with its huge bandwidth is able to resolve much higher number of MPCs, the arrival times of these components are no longer continuous, but rather grouped in so called *clusters*, each resulting from various scattering objects such as walls, ceilings, floors, cupboards, desks or any smaller object within the coverage area.

These observations paved the way for the establishment of a channel modelling sub-committee within the IEEE 802.15.3a and IEEE 802.15.4a standardisation groups, which developed common large- and small scale propagation models to characterise the UWB signal behaviour over short distances. The resulting statistical UWB channel model (CM) defines the path-loss, shadowing and small-scaled fading as follows:

The *path loss* is derived from the Friis' equation (free-space path loss), using the geometric mean of the lower and upper band frequencies as a center frequency $f_c = \sqrt{f_L f_U}$, see also Section 4.1.1. For the *shadowing*, a lognormal distribution with standard deviation σ_χ of 3 dB is adopted, i.e.

$$20 \log_{10}(\chi) \propto N(0, \sigma_\chi^2).$$

The *multipath model*, i.e. small-scale fading, is based on a slight modification of the Saleh-Valenzuela (S-V) model for indoor wideband channels [14] to better fit the findings of the conducted UWB channel measurement campaigns. It defines the discrete time impulse response of the channel as

$$h(t) = \chi \sum_{l=0}^L \sum_{k=0}^K \alpha_{k,l} \delta(t - T_l - \tau_{k,l}), \quad (2.4)$$

where $\alpha_{k,l}$ is the lognormally distributed multipath gain coefficient of the k th ray within the l th cluster, T_l the arrival time of the l th cluster, $\tau_{k,l}$ the delay of the k th MPC relative to T_l (by definition $\tau_{0,l} = 0$). The exponential decay of the channel power over the clusters is reflected by the cluster decay factor Γ , whereas the power decay within a cluster is characterised by the ray decay factor γ .

The cluster and multipath (ray) arrival times are modelled as Poisson processes, given the cluster and ray arrivals rates Λ and λ respectively:

$$p_{T_l}(T_l | T_{l-1}) = \Lambda \exp[-\Lambda(T_l - T_{l-1})], \text{ for } l > 0 \quad (2.5)$$

$$p_{\tau_{k,l}}(\tau_{k,l} | \tau_{(k-1),l}) = \lambda \exp[-\lambda(\tau_{k,l} - \tau_{(k-1),l})], \text{ for } k > 0. \quad (2.6)$$

The standard further defines four sets of CM parameters to account for different types on indoor environments, including LOS (CM1 for 0-4 m range) and NLOS (CM2/3 over up to 4/10 m respectively) scenarios, as well as large delay spreads of 25 ns (CM4). The main parameters of the IEEE 802.15.3a UWB channel are summarised in Table 2.1.

Table 2.1: Main parameters of the IEEE 802.15.3a UWB CM1-4 in [16].

Model Parameter	CM1 (0-4 m LOS)	CM2 (0-4 m NLOS)	CM3 (4-10 m NLOS)	CM4 (4-10 m NLOS)
Λ (1/ns)	0.0233	0.4	0.0667	0.0667
λ (1/ns)	2.5	0.5	2.1	2.1
Γ	7.1	5.5	14	24
γ	4.3	6.7	7.9	12

2.4.2 Correlation-based Double-directional Stochastic MIMO-UWB Channel Model

In general, the performance of spatially multiplexed MIMO systems and the potential enhancements in spectral efficiency are substantially degraded in the case of highly correlated sub-channels [17]. To allow for accurate and predictable evaluation of our MIMO detection schemes, a MIMO-UWB channel model has therefore to reflect the spatial correlation among the different signal paths. Simple modelling of the spatial correlation characteristic of the MIMO-UWB channel relies on constant correlation coefficients extracted from measurement data and on the Kronecker model as applied in narrowband and broadband systems [17]-[65]. More sophisticated stochastic approaches take into account the geometry and both angular and temporal statistics of the UWB propagation

channel to reflect the frequency dependence of the spatial correlation function. In the following, we adopt the correlation-based double-directional stochastic MIMO-UWB channel model presented in [12] to allow for deeper insight on the effect of spatial correlation as function of e.g. the antenna spacing and frequency range. According to this model, the impulse response of the sub-channel from TX antenna p to RX antenna q of the MIMO-UWB channel is given as

$$h^{p,q}(t, \theta_T, \theta_R) = \sum_{l=0}^L \sum_{k=0}^K \underbrace{\alpha_{k,l}^{p,q} \delta(t - T_l^{p,q} - \tau_{k,l}^{p,q}) \delta(\theta_T - \theta_{k,l,\text{AoD}}) \delta(\theta_R - \theta_{k,l,\text{AoA}})}_{h_{k,l}^{p,q}}, \quad (2.7)$$

where $\alpha_{k,l}^{p,q}$ is the complex channel coefficient of the k -th ($k = (0, \dots, K)$) ray of the l -th ($l = (0, \dots, L)$) cluster, $T_l^{p,q}$ is the arrival time of the first ray of cluster l , and $\tau_{k,l}^{p,q}$ the corresponding arrival time of ray k within this cluster. The Angle-of-Departure (AoD) and Angle-of-Arrival (AoA) of the k -th ray of cluster l are further denoted by $\theta_{k,l,\text{AoD}}$ and $\theta_{k,l,\text{AoA}}$ respectively. Note that in case of linear TX and RX antenna arrays we omit for brevity the corresponding antenna indices of the AoD and AoA parameters.

The impulse response of the double-directional MIMO channel can thus be constructed as

$$\mathbf{H}(t, \theta_T, \theta_R) = \sum_{l=0}^L \sum_{k=0}^K \mathbf{H}_{k,l} = \sum_{l=0}^L \sum_{k=0}^K \mathbf{A}_{k,l} \circ \delta(t - \mathbf{P}_{k,l}) \delta(\theta_T - \theta_{k,l,\text{AoD}}) \delta(\theta_R - \theta_{k,l,\text{AoA}}), \quad (2.8)$$

with

$$\mathbf{H}_{k,l} = \begin{bmatrix} h_{k,l}^{1,1} & \dots & h_{k,l}^{1,N_R} \\ \vdots & h_{k,l}^{p,q} & \vdots \\ h_{k,l}^{N_T,1} & \dots & h_{k,l}^{N_T,N_R} \end{bmatrix}, \quad \mathbf{A}_{k,l} = \begin{bmatrix} \alpha_{k,l}^{1,1} & \dots & \alpha_{k,l}^{1,N_R} \\ \vdots & \alpha_{k,l}^{p,q} & \vdots \\ \alpha_{k,l}^{N_T,1} & \dots & \alpha_{k,l}^{N_T,N_R} \end{bmatrix} \quad \text{and} \quad \mathbf{P}_{k,l} = \begin{bmatrix} \epsilon_{k,l}^{1,1} & \dots & \epsilon_{k,l}^{1,N_R} \\ \vdots & \epsilon_{k,l}^{p,q} & \vdots \\ \epsilon_{k,l}^{N_T,1} & \dots & \epsilon_{k,l}^{N_T,N_R} \end{bmatrix},$$

standing for the MIMO channel matrix, amplitude- and Time-of-Arrival (ToA) matrices of the k -th ray of the l -th cluster. The elements of the spatially correlated amplitude matrix $\mathbf{A}_{k,l}$ are modelled as

$$\alpha_{k,l} = p_{k,l} \xi_l \beta_{k,l}, \quad \text{with} \quad \xi_l = 10^{v_l/20} \quad \text{and} \quad \beta_{k,l} = 10^{(\mu_{k,l} + v_{k,l}^{p,q})/20},$$

where $p_{k,l} = \pm 1$ accounts for the amplitude inversion due to reflections, ξ_l stands for the fading of cluster l , and $\beta_{k,l}$ corresponds to the fading of ray k within this cluster. The lognormally distributed cluster and ray fading (with mean $\mu_{k,l}$) are generated from zero-mean Gaussian RVs v_l and $v_{k,l}^{p,q}$. These RVs (and thus the elements of $\mathbf{A}_{k,l}$) are derived from an $N_T N_R \times N_T N_R$ correlation matrix $\mathbf{R}_{k,l} = \mathbf{R}_{k,l}^T \otimes \mathbf{R}_{k,l}^R$, which is modelled as the Kronecker product of the spatial correlation matrices at the transmitter and receiver, since the AoDs and AoAs are assumed independent RVs and are thus perfectly separable from each other.

For example, the elements of the $N_T \times N_T$ transmit correlation matrix $\mathbf{R}_{k,l}^T$ are the complex correlation coefficients between two TX antenna elements p_i and p_j separated by the distance d_{p_i,p_j} , i.e.

$$\rho_{k,l}^{p_i,p_j} = \mathbb{E} \left\{ \frac{1}{M} \sum_{m=1}^M \exp \left(j \frac{2\pi f_c}{c} d_{p_i,p_j} \sin(\vartheta_{m,k,l,\text{AoD}}) \right) \right\}, \quad (2.9)$$

where f_c is the center frequency, and $\vartheta_{m,k,l,\text{AoD}}$ is the AoD of the m -th ($m=1,\dots,M$) irresolvable path of the k -th ray of cluster l . With $\rho_{k,l}^{p_i,p_j} = 1$ for all $p_i = p_j$, and $\rho_{k,l}^{p_j,p_i} = (\rho_{k,l}^{p_i,p_j})^*$, the TX correlation matrix $\mathbf{R}_{k,l}^T$ can be written as

$$\mathbf{R}_{k,l}^T = \begin{bmatrix} 1 & \rho_{k,l}^{1,2} & \cdots & \rho_{k,l}^{1,N_T} \\ (\rho_{k,l}^{1,2})^* & 1 & & \rho_{k,l}^{2,N_T} \\ \vdots & & \ddots & \vdots \\ (\rho_{k,l}^{1,N_T})^* & (\rho_{k,l}^{2,N_T})^* & \cdots & 1 \end{bmatrix}. \quad (2.10)$$

Finally, the ToA difference among the antenna array elements depends on the AoD (and AoA) and the antenna spacing d_T (and d_R) of the TX and RX array respectively, as follows

$$\varepsilon_{k,l}^{p,q} = \varepsilon_{k,l}^{1,1} + (p-1) \frac{d_R \sin(\theta_{k,l,\text{AoA}})}{c} + (q-1) \frac{d_T \sin(\theta_{k,l,\text{AoD}})}{c},$$

with c being the speed of light. Further details on modelling the spatial correlation among the entries of $\mathbf{A}_{k,l}$ and $\mathbf{P}_{k,l}$ can be found in [12].

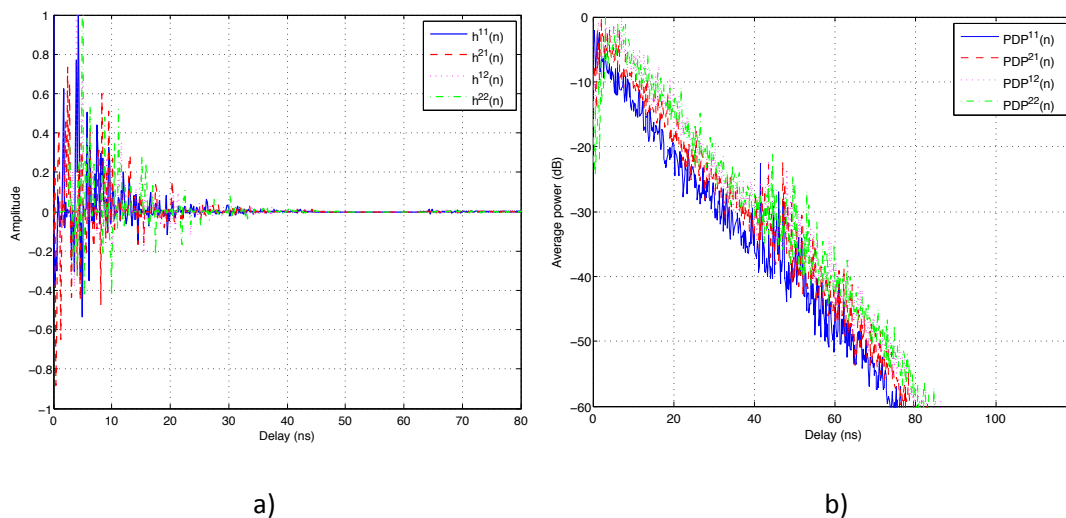


Figure 2.6: Typical realisation of a) the impulse responses, and b) PDPs of a spatially correlated 2×2 MIMO-UWB CM1.

Figure 2.6 shows an example of the impulse responses $h^{p,q}(n)$ of a spatially correlated 2×2 MIMO-UWB based on CM1 scenario (0-4m LOS) for $d_T = 10$ cm, $d_R = 20$ cm and sampling period $T_S = 0.167$ ns. The channel statistics of the presented spatially correlated model prove consistent with the modified Saleh-Valenzuela (S-V) model of IEEE802.15.3a SG in [16], as illustrated by e.g. the cumulative distribution function (CDF) of the mean excess delay (MED) for CM1 shown in Figure 2.7.

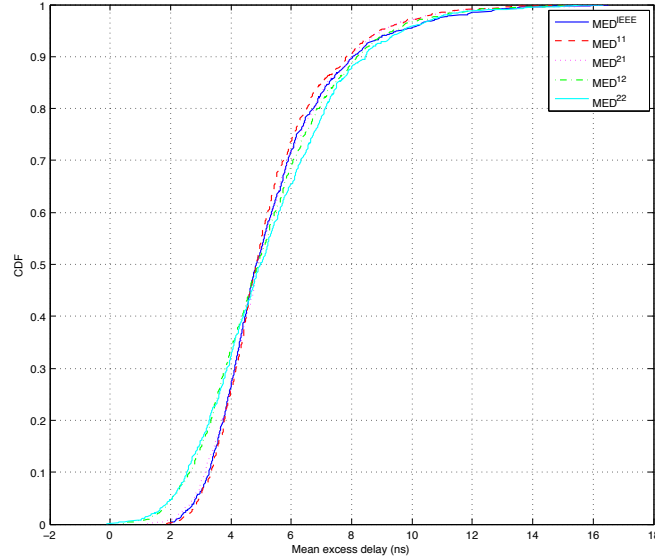


Figure 2.7: CDF of the mean excess delay of the spatially correlated MIMO-UWB channel model.

The spatial correlation characteristics in time and frequency are reflected by the complex correlation coefficients $\hat{\rho}_T(d_R)$ and $\hat{\rho}_F(f, d_R)$, which in the case of a Single-Input Multiple-Output (SIMO) channel are defined as

$$\hat{\rho}_T(d_R) = E \left\{ \frac{\sum_{n=1}^N (h^{1,1}(n) - \bar{h}^{1,1})(h^{1,2}(n) - \bar{h}^{1,2})^*}{\sqrt{\sum_{n=1}^N |h^{1,1}(n) - \bar{h}^{1,1}|^2 \sum_{n=1}^N |h^{1,2}(n) - \bar{h}^{1,2}|^2}} \right\} \text{ and}$$

$$\hat{\rho}_F(f, d_R) = \frac{E \left\{ (H^{1,1}(f) - \bar{H}^{1,1}(f))(H^{1,2}(f) - \bar{H}^{1,2}(f))^* \right\}}{\sqrt{E \left\{ |H^{1,1}(f) - \bar{H}^{1,1}(f)|^2 \right\}} \sqrt{E \left\{ |H^{1,2}(f) - \bar{H}^{1,2}(f)|^2 \right\}}}, \quad (2.11)$$

with $\bar{h}^{p,q} = 1/N \sum_{n=1}^N h^{p,q}(n)$ and $\bar{H}^{p,q}(f) = E \{ H^{p,q}(f) \}$ for $p=1, q=1,2$. Figure 2.8 illustrates the spatial correlation of the channel impulse responses for the 1×2 SIMO case in CM1 depending on the RX antenna separation and sampling period T_S . As expected, the spatial correlation decreases in an oscillating manner with increasing antenna spacing and reaches values below 0.5 for d_R equalling half the maximum wavelength $\lambda_{\max}/2 = c/(2f_{\min}) \approx 4.7$ cm of a MB-OFDM signal transmitted in BG1. However, with decreasing channel resolution and higher sampling period T_S , the spatial correlation increases implying that systems with less bandwidth may not benefit from the channel

diversity to its full extent. In fact, as the sampling period increases, more MPCs fall into the same channel tap, causing higher correlation of the multipath time-of-arrivals (ToAs) among the MIMO sub-channels and reducing the potential for spatial multiplexing systems.

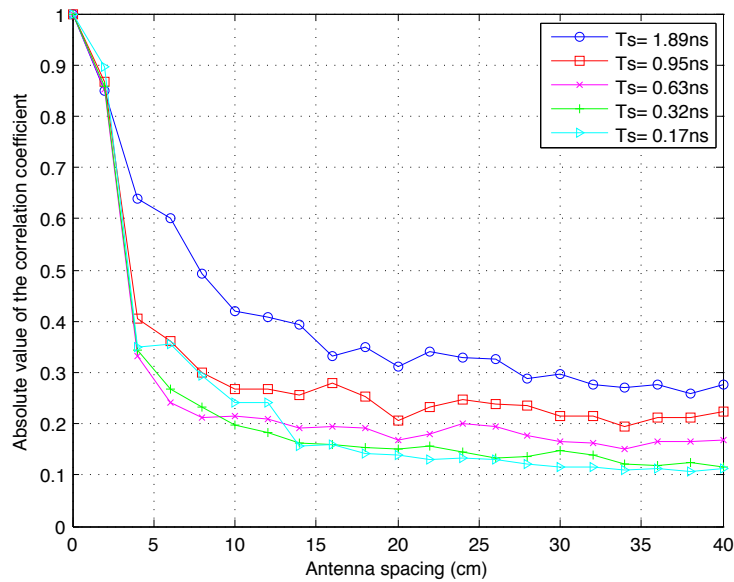


Figure 2.8: Absolute value of the spatial correlation coefficient of the SIMO channel impulse responses.

Figure 2.9 depicts the frequency behaviour of the spatial correlation coefficient for the 1×2 SIMO case in CM1 with variable RX antenna separation and $T_s = 0.167$ ns. Similar to narrowband channels, the spatial correlation decreases for higher antenna spacing and fixed frequency. Over the entire frequency range, the correlation coefficient becomes lower for higher frequencies and fixed antenna spacing as the antenna separation decreases in terms of wavelength. This is also true for the main lobe width of the correlation coefficient that gradually decreases for higher frequencies.

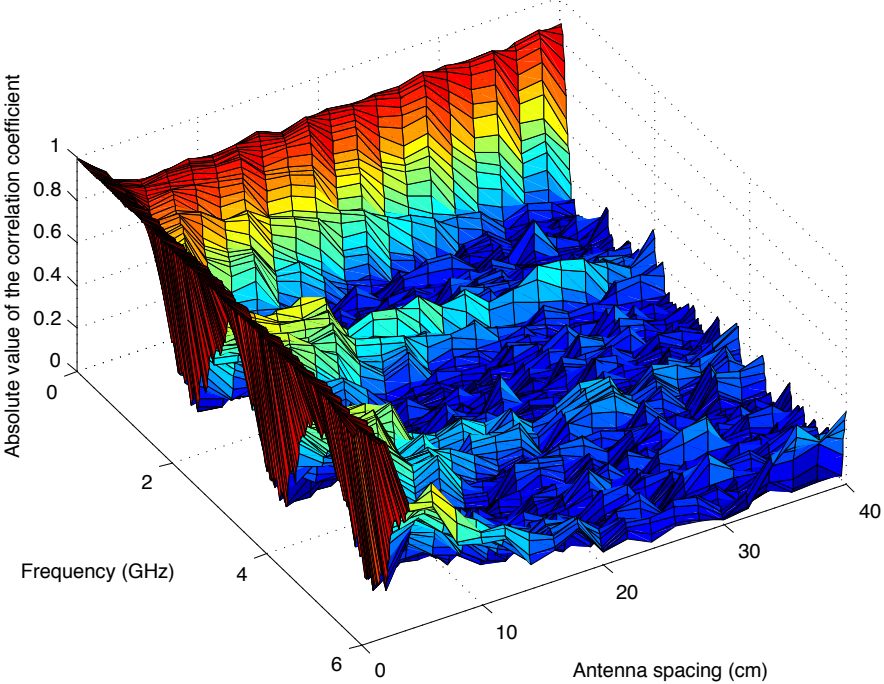


Figure 2.9: Frequency behaviour of the spatial correlation coefficient for varying antenna spacing.

Chapter 3

Multiple-Input Multiple-Output Technology

Multiple-Input Multiple-Output (MIMO) systems have been widely considered a viable solution to overcome the current limits in wireless communication. The application of Ultra-wideband (UWB) to indoor environments, with the rich energy scattering and large angular spreads of the multipath channel, provides an ideal scenario for deploying multiple antennas. By exploiting the *spatial* dimension and thus unclosing additional degree of freedom for communication, MIMO systems can effectively turn multipath propagation, considered initially a drawback in wireless communications, into an advantage so as to linearly increase the capacity of the system, or improve its coverage and robustness in terms of error probability.

The basic idea behind the MIMO approach is to combine the spatial dimension brought by the use of multiple antennas with the time dimension in a way that would exploit the diversity present in a multi-path fading environment to improve the quality of the link or, on the other hand, to increase the spectral efficiency by opening parallel and independent data pipes in the system. The major benefits which could be obtained by deploying multiple-antenna schemes are summarized below:

- *Array gain* - is defined as the average increase in SNR at the receiver due to the coherent combining effect of using multiple antennas at the TX and/or RX side. The resulting enhancement of the signal power leads to an increased range coverage and Quality of Service (QoS). In order to achieve an array gain, MIMO systems typically require perfect channel knowledge either at the transmitter or the receiver, or at both.
- *Diversity gain* - Diversity is the generic concept of introducing redundancy to overcome noise and to increase the robustness of the system, and is typically characterized by the number of independent fading paths in a channel (also referred to as diversity order). According to the dimension which has been exploited, diversity can be categorized into *temporal*, *frequency* or *spatial* diversity gain. In the first case, the transmitted symbols are repeated across time by a combination of channel coding and interleaving schemes. This gain can be exploited provided that the wireless channel has sufficient variations in time, i.e. the channel coherence time is smaller than the duration of the coded interleaved symbol, which will essentially turn into an independent replica of its original version. Frequency diversity on the other hand provides replicas of the transmitted signal in the frequency domain, given that the coherence bandwidth of the channel is smaller than that of the signal. Since in this case different parts of the assigned spectrum will suffer independent fades, the probability that

all signal copies will be in a deep fade simultaneously is rather small. This is effectively exploited by e.g. coded interleaved OFDM systems, in which copies of the information bearing bits are mapped to different, non-adjacent sub-carriers thus reducing the probability of burst errors.

- *Spatial multiplexing gain* - In spatial multiplexing, multiple antennas at both transmitter and receiver side are used to send independent data streams in parallel. In a rich scattering environment, this technique allows to create several spatial data pipes within the same frequency band, which significantly increases data rate and spectral efficiency. The channel capacity increases linearly with the minimum number of transmit/receive antennas, at no additional power consumption or increase in signal bandwidth.
- *Interference suppression* - By exploiting the spatial dimension provided by multiple antenna elements, the receiver is able to suppress interfering signals in a way that is not possible with a single antenna. Hence, the system can be tuned to be less susceptible to interference and leads to an overall improvement of the Signal-to-Interference-plus-Noise-Ratio (SINR) and system capacity.

The use of multiple antennas however implies an increase in hardware costs and computational complexity of the system, as some of the blocks have to be replicated for each antenna branch. The main challenge is therefore to find a reasonable trade-off between the capacity and/or performance gains achieved by using multiple antennas, and the complexity incurred thereby. Moreover, due to the conflicting demands on the spatial degree of freedom, some combination of the above-mentioned benefits may be needed, i.e. a flexible trade-off between the multiplexing and diversity gain needs to be found depending on the specific application requirements and propagation constraints. It has been shown in [18] that for a classical i.i.d. frequency-flat Rayleigh fading MIMO channel with optimal transceiver design, a diversity-multiplexing trade-off can be found along the curve spanned by the equation

$$d(r) = (N_R - r)(N_T - r) \quad (3.1)$$

where $d = 0, 1, \dots, N_T N_R$ is the diversity gain, and $r = 0, 1, \dots, \min\{N_T, N_R\}$ the multiplexing gain respectively. Thus, it is not possible to simultaneously achieve full diversity and multiplexing gain, i.e. maximizing transmission rate always comes at the expense of sacrificing system performance in terms of BER, and vice versa.

While the benefits of MIMO have been widely studied and exploited in broadband MIMO-OFDM wireless communications, the field of real-world implementation and verification of multiple antenna UWB solutions is still unexplored. In this thesis, we have therefore focused on developing and investigating suitable MIMO approaches from the perspective of low-complexity algorithm design

and implementation-level constraints to allow for enhancements in spectral efficiency and potentially highest data rates of the current ECMA-368 PHY/MAC standard.

3.1 MIMO-OFDM System Model

In the following we consider an $N_R \times N_T$ discrete complex MIMO-OFDM signal model in the frequency domain, where the received signal at a certain frequency tone is given by

$$\mathbf{Y} = \mathbf{H}\mathbf{S} + \mathbf{W} \quad (3.2)$$

with $\mathbf{S} = [S_1, \dots, S_{N_T}]^T$ and $\mathbf{Y} = [Y_1, \dots, Y_{N_R}]^T$ being the transmitted and received tone vectors. \mathbf{W} stands for the zero-mean complex white Gaussian noise with variance $\sigma_n^2 \mathbf{I}_{N_R}$, and \mathbf{I}_{N_R} denotes an $N_R \times N_R$ identity matrix. Since the channel coherence bandwidth exceeds the sub-carrier spacing of a MB-OFDM signal, the MIMO channel matrix $\mathbf{H} \in \mathbb{C}^{N_R \times N_T}$ at a given frequency tone k can be considered as frequency flat and has as elements the frequency responses $H_{ji}(k, m)$ of the sub-paths between the i -th transmit and j -th receive antenna at a symbol index m . Note that the above system model applies for each sub-band index l , which has been omitted here for brevity.

3.2 Multiple Antenna Techniques at the Transmitter

3.2.1 Spatial Multiplexing

Traditionally, multiple antennas have been used to obtain maximum diversity gain in order to combat the channel fading caused by multi-path propagation, and thus improve the SNR and system performance in terms of error propagation. In Spatial Multiplexing (SMUX) schemes (as used in e.g. V-BLAST architectures [19]) alternatively, the payload data are demultiplexed into N_T independent sub-streams, which are then simultaneously transmitted on the N_T antennas. At the receiver, after having estimated the MIMO channel, the individual sub-streams are recovered out of the received signal mixture by various decoding algorithms and then multiplexed to the original data stream, as has been schematically depicted in Figure 3.1.

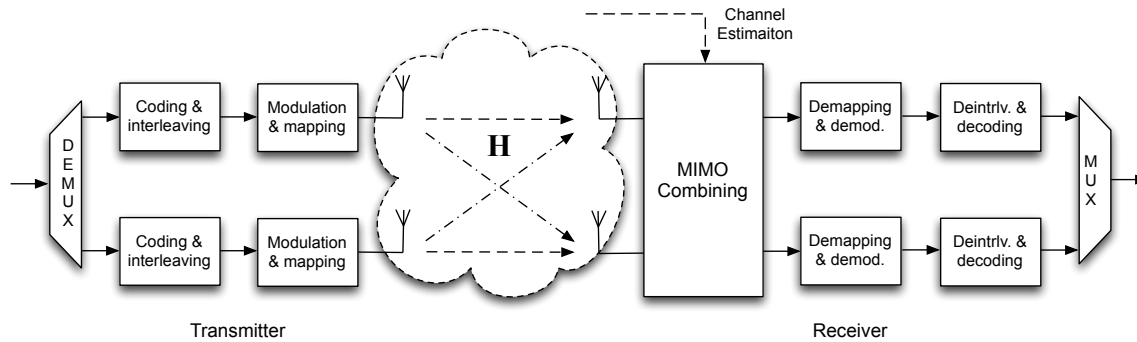


Figure 3.1: Spatial Multiplexing scheme for MIMO Wireless Communications.

While the RX possesses knowledge of the channel and may thus provide some receive diversity, the system cannot achieve any transmit diversity gain since the bit streams are completely independent from each other as they carry different data. In contrast to spatial diversity schemes which attempt to counteract fading, SMUX suggests that fading can in fact be beneficial through increasing the degrees of freedom available for communication. Essentially, if the path gains between individual transmit-receive antenna pairs fade independently, the MIMO channel itself can be sub-divided in multiple spatial data pipes, which then allow for a multiple increase in throughput and data rate. Foschini and Telatar showed in [1][2] that, e.g. in uncorrelated Rayleigh fading channels, the ergodic capacity grows linearly with the minimum of the number of transmit and receive antennas provided that the SNR is sufficiently high. This increase in data rate requires virtually no additional power or system bandwidth, but may be slightly degraded in practical systems due to imperfections and correlation constraints of the wireless channel.

3.2.2 Dual Mode Transmission

The so-called Dual mode operation has been recently considered within the WiMedia Alliance as a candidate for enhancing the current ECMA-368 standard towards Very High Data Rate (VHDR) communications. In contrast to the alternative of doubling the bandwidth and FFT size, the dual mode is based on the existing WiMedia system architecture, preserving the frequency band of 528 MHz and 128-point FFT size. The enhancement in throughput is achieved by *virtually* doubling the system bandwidth through demultiplexing the transmitted signals on two antenna branches, and up-converting them to (not necessarily) adjacent sub-bands. This is illustrated in Figure 3.2, where the receiver has e.g. four antenna elements in order to combine the independent data streams and introduce diversity to the system.

Main advantage of this technique as compared to using an e.g. 256-pt FFT is its back-compatibility to the existing ECMA-368 architecture and data/pilot allocation, the ability to exploit diversity gain through band switching, as well as the more efficient multiple-user support.

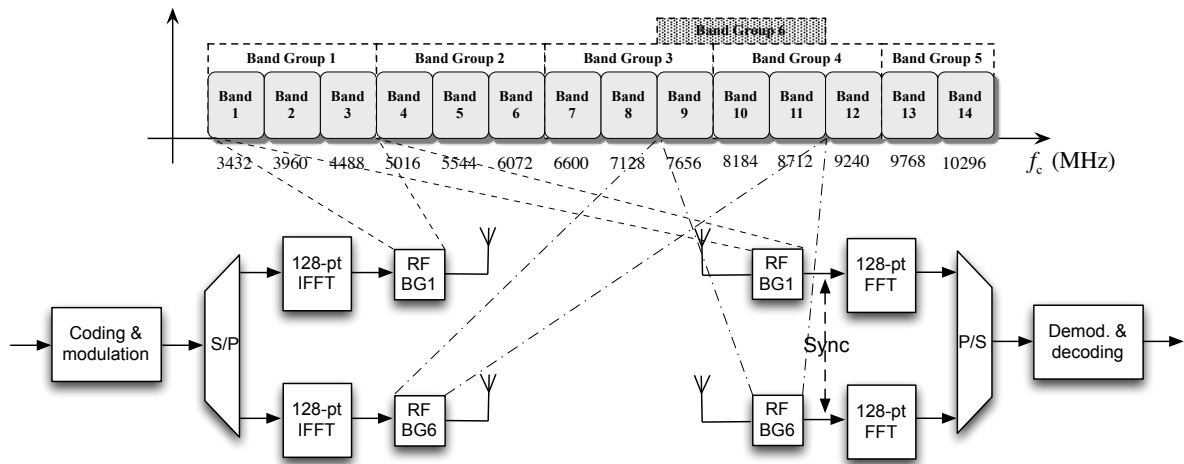


Figure 3.2: Dual mode operation of MB-OFDM with multiple antennas

Another benefit is the reduced non-linearity and dynamic range requirements for the RF circuitry (ADC/DAC, power amplifiers, BP filters), as well as the improved robustness to interference. Moreover, this approach reduces the complexity and power consumption of the IFFT-/FFT blocks compared with the 1056-MHz mode and ensures better backward-compatibility to the current ECMA-368 standard.

Basically, one can exploit dual mode transmission in two ways. Similar to spatial multiplexing, it can double the capacity of the system if the transmit signals on both antenna branches are completely independent. Signal separation and MIMO combining in this case may be performed by pure band-pass filtering of the received signals due to the orthogonality of both frequency band groups. This reduces the complexity of equalization and decoding while further improving the interference suppression and robustness of the system as compared to conventional spatial multiplexing schemes. Alternatively, one may exploit the channelization on different bands in order to add diversity to the system, e.g. by simultaneously transmitting the same user information on the two parallel frequency channels (or even whole band groups).

Regardless of the aforementioned advantages, the dual mode transmission still implies replication of the RF chains in both TX and RX, including separate frequency circuits to control the channel mapping on both band groups. For application scenarios requiring VHDR, e.g. in short-range communication between set-up boxes or HDTV devices, enough space for placing two or even more antennas should be available.

3.2.3 Diversity Schemes in Space, Time and Frequency

Due to the low power emissions of UWB as imposed by regulators and the stringent requirements for interference-free coexistence with incumbent licensed co-located and adjacent band services (e.g. WiMAX, IEEE 802.11a/n, Military and Civil Aeronautical Radars), the coverage of UWB communications is limited to several meters, not exceeding 10 m for the lowest data rates and most

robust error correction schemes. This inevitably motivates the deployment of various diversity schemes to exploit the spatial, time- and/or frequency dimension and enhance the robustness of the communication link (in terms of BER) or the coverage of the system.

While SMUX schemes provide an effective way to linearly increase the capacity of MIMO-UWB, decoding the transmitted constellation points still requires that the number of RX antennas be at least equal to the number of independent data streams. Linear decoding such as ZF or MMSE, or Successive Interference Cancellation (SIC) as used in V-BLAST architectures thus becomes viable only at fixed Access Points (AP) or Base Stations (BS), where the space available, power consumption and processing capabilities allow for placing higher number of RX antennas. For mobile, hand-held devices it may thus be much more reasonable to deploy some sort of diversity schemes, which typically require only a single antenna at the RX, implying that the code rate cannot exceed one.

3.2.3.1 *Time- and Frequency Domain Spreading*

A straightforward way to provide diversity in the system is by repeatedly placing (spreading) the same information on adjacent or consecutive symbols blocks. The ECMA-368 standard already specifies two simple forms of time- and frequency spreading, which are applied depending on the data rate of transmission and the channel conditions.

For data rates lower or equal to 200 Mbps, Time Domain Spreading (TDS) duplicates the k -th subcarrier of an even symbol by swapping the real and imaginary parts, scrambling the outcome and placing it on the $-k$ -th position of the succeeding symbol. Note that this technique provides a diversity order of *two*, and further reduces the correlation between adjacent OFDM symbols, even when frequency hopping is not applied.

Frequency Domain Spreading (FDS) on the other hand is always used in combination with TDS for the lowest data rates (53.3 Mbps and 80 Mbps) supported by the system. The main idea behind FDS is to ensure that a data symbol will be impacted by possibly independent channel fading levels, allowing the RX to reliably extract the data by using e.g. Maximum-Ratio-Combining (MRC) even in the case of deep channel fades. In FDS, a constellation point is placed on two frequency-symmetric subcarriers, i.e. subcarrier $-k$ being the conjugate of subcarrier k , ensuring the OFDM spectrum becomes conjugate-symmetric. This mechanism relaxes the requirements for the digital-to-analog conversion (DAC) at the TX, as the OFDM signal becomes real-valued and the DAC for the quadrature channel can be simply turned off. Note that in this case, TDS simply replicates and scrambles the subcarriers of a symbol to the adjacent symbol in time. Depending on whether the system applies frequency hopping or not, FDS in combination with TDS can achieve a maximum diversity order of *four*, whereas even in a non-hopping case this techniques doubles the energy per bit at the RX, thus improving system performance in terms of error propagation.

3.2.3.2 Orthogonal Space-Time-Frequency Coding

Space-Time-Block coding (STBC) is already well explored and widely implemented in narrowband and broadband wireless systems, including standards such as IEEE 802.11n, WiMAX, or LTE. The most prominent example of STBC is the so-called Alamouti scheme [20] for transmission with two antennas. According to it, every two symbols S_1 and S_2 are grouped together and transmitted simultaneously over the antennas, see Figure 3.3. In the next symbol period, the same information, but orthogonal to the first block, i.e. $-S_2^*$ and S_1^* , is placed on the first and second antenna respectively. This simple but ingenious scheme is known as the only full-rate and full-diversity code for both real and complex signal constellations, for which an efficient *linear* combination algorithm exists. Besides doubling the effective SNR at the output of the decoder, it provides soft-decision output for the succeeding channel decoding stage, thus increasing the reliability of error correction. Finally, it does not require any CSI at the transmitter, i.e. the system can operate in open loop without the need of costly (in terms of bandwidth or throughput) or possibly out-dated feedback from the receiver.

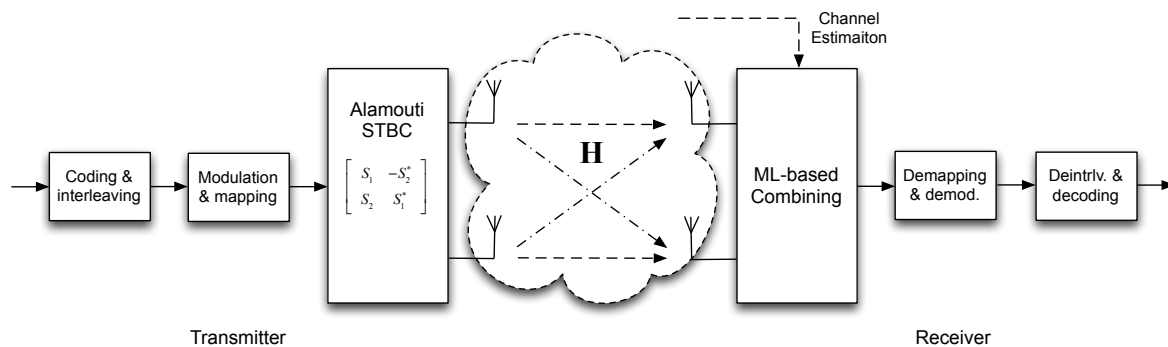


Figure 3.3: Space-Time-Block Coding with Alamouti scheme

Main restriction of the Alamouti code however, is that it applies to only *two* TX antennas. There has been substantial research on more sophisticated coding schemes applicable to MIMO systems with a higher number of antennas using the theory of orthogonal code designs [21]. For MB-OFDM UWB, a complete Space-Time-Frequency (STF) coding framework, profound analysis of system performance and achievable diversity gains is presented in [22]. In Section 5.4, we further provide practical examples of the application of rate 3/4 orthogonal STF codes for 3 and 4 TX antennas to MIMO MB-OFDM. Note that this rate has been proven to be the maximum achievable one for systems with more than two TX antennas. In fact, the coding matrices can be applied either in the time- or frequency domain, the basic prerequisite being that the channel response remain constant at least for the duration of four symbol blocks. This implies that when deployed for MB-OFDM in the time domain, the TX has to operate in Fixed-Frequency Interleaving (FFI) mode, i.e. on a single frequency band, using TFCs 5, 6 or 7 only.

3.2.4 Antenna Subset Selection

In a closed-loop system where some kind of CSI is available at the TX, combining STFC with antenna selection may become a viable solution to save power consumption and reduce error propagation. In case more than two TX antennas are present in the system, the Alamouti code may for example be combined with antenna selection techniques, which rely on full or partial knowledge of the CSI in order to select the best TX antenna pair. This alleviates the power consumption and non-linearity requirements of the TX frontend, as the RF chains unable to provide sufficient link quality can be simply switched off. Such kind of a cognitive system design certainly is of interest for future research on the optimal trade-off between induced complexity and diversity exploitation.

3.3 MIMO Combining at the Receiver

The inherent task of the MIMO receiver is to extract and/or combine the individual data streams out of the mixture of interfering signals at each RX antenna branch. In addition to this, it has to compensate for the multipath fading and additive noise effects that distort the received signal. In case of MIMO systems with spatial multiplexing, the most common detection schemes are based on either sub-optimal linear receivers such as ZF and MMSE, or more sophisticated non-linear algorithms such as V-BLAST and (O)SIC, and Sphere- or K-Best decoding with close-to-ML performance.

In the following, we briefly review the basic features and operation of the abovementioned receivers and compare their BER performances with a reference Maximum Likelihood (ML) decoder with exhaustive search over all possible solutions.

3.3.1 Linear Receivers

Starting with the system model in Eq. (3.2), a straightforward approach to recover the transmitted tone vector \mathbf{S} out of the received mixture \mathbf{Y} is to multiply the latter with an equalizer matrix \mathbf{G} , such that the estimate $\hat{\mathbf{S}} = \mathbf{G}\mathbf{Y}$ is a weighted linear combination of the received signal. The ZF algorithm attempts to perfectly suppress the mutual interference between the N_T parallel layers by directly inverting the MIMO channel, i.e.

$$\mathbf{G}_{\text{ZF}} = (\mathbf{H}^H \mathbf{H})^{-1} \mathbf{H}^H = \mathbf{H}^\dagger, \quad (3.3)$$

where \mathbf{H}^\dagger is the Moore-Ponrose pseudo-inverse of the channel matrix \mathbf{H} . It is well known that the ZF receiver is error-dependent on the covariance matrix of the noise component, which leads to noise amplification and sub-optimal performance.

An MMSE MIMO receiver, on the other hand, searches for an equalizing matrix which minimizes the overall mean-square error due to noise and mutual interference, however at the cost of separation quality of the signals [23]

$$\mathbf{G}_{\text{MMSE}} = (\mathbf{H}^H \mathbf{H} + \frac{1}{\rho} \mathbf{I})^{-1} \mathbf{H}^H, \quad (3.4)$$

where $\rho = \sigma_s^2 / (N_T \sigma_n^2)$ stands for the SNR at the decoder input.

While both linear receivers require nearly the same order of computational effort, their performance becomes very close for OFDM-based transmission und frequency-selective fading channels, especially in the high SNR regime. For low SNR, the MMSE RX is reported to marginally outperform ZF in terms of BER performance, however with the unrealistic assumption of perfect SNR estimation at the RX. Efficient approaches for SNR estimation in the frequency domain may reach its actual value, however often at the price of reduced spectral efficiency or increased complexity of the digital baseband processing. The use of more rough estimates of the signal power (as needed by the AGC) will degrade the quality of the MMSE signal separation and eventually converge its performance to that of ZF [24]. It therefore poses a trade-off between the reduced noise amplification and the worse interference suppression as compared to ZF.

Regarding the computational complexity of linear MIMO receivers like ZF and MMSE, most approaches present in literature aim at an efficient matrix-inversion. Using the Cramer's Rule for efficient computation of a matrix inverse, the computational complexity of ZF and MMSE in a symmetric $N_T \times N_T$ MIMO system is reported to grow exponentially with the number of transmit/receive antennas N_T [85].

3.3.2 Successive Interference Cancellation for V-BLAST Architectures

The basic idea behind Successive Interference Cancellation is that unlike linear receivers the estimates of the transmitted parallel data streams are no longer extracted at once, but rather one after the other. Indeed, the SIC receiver exploits the fact that the decoded symbols belong to the same constellation alphabet, and cancels the contribution of each successively decoded layer out of the received signal mixture before decoding the next layer. Unfortunately, the performance of such a detect-and-cancel strategy is dominated by the stream which is detected first and highly depends on the correct ordering, leading to error propagation in the subsequent stages. The original V-BLAST algorithm is known to find the optimal ordering with respect to the BER performance by minimizing the noise component on the symbol estimate at each detection layer, thus reducing the error propagation in the following stages. Clearly, the nonlinear V-BLAST receiver with both ZF- and MMSE-criterion is able to outperform its linear counterparts, as shown in Figure 3.4. Note that the pre-

processing stage of the V-BLAST algorithm still requires a costly (yet reduced) matrix inversion for every iteration, however its total complexity remains in the order of that of linear receivers [23].

More sophisticated approaches focus on iterative QR-decomposition of the estimated MIMO channel matrix, with no need of matrix inversions. Sorted QR-decomposition open the way for an efficient implementation of various MIMO detection algorithms, starting from simple linear receivers, ordered successive interference cancellation schemes as used in V-BLAST architectures, or close-to-ML tree-search algorithms like sphere decoding. While such iterative approaches add a small penalty in terms of system performance and throughput, they still provide significant performance improvement and high potential for complexity reductions of the baseband MIMO processing. Detailed description of MIMO decoding with (sorted-) QR decomposition is provided in Chapter 5, Sections 5.2 and 5.3.

3.3.3 Close-to-ML Efficient MIMO Processing

Maximum Likelihood has been widely reported to achieve the optimal performance among all MIMO detection algorithms. It tries to find the symbol vector $\hat{\mathbf{S}}$ which has been most likely transmitted by minimizing the squared error from the received signal

$$\hat{\mathbf{S}} = \underset{\mathbf{s}}{\operatorname{argmin}} \left\{ \|\mathbf{Y} - \mathbf{H}\mathbf{s}\|^2 \right\}. \quad (3.5)$$

Although the ML receiver is considered optimal in the sense that it provides a full N_T diversity order and minimum power losses, its exhaustive search over a total of M^{N_T} candidate constellation points (out of an M -ary alphabet) results in an exponential increase of the computational complexity in case of higher modulation schemes. With the exception of BPSK and QPSK modulations, the exhaustive search ML thus becomes prohibitive for both verification and implementation purposes, and has been shown here only as reference. Note that implementation-specific MIMO detection schemes such as K-Best decoding or Sphere Decoding with early termination have been reported in [23] to achieve close-to-ML performance at significant reduction of the computational and implementation complexity.

In order to significantly reduce the receiver complexity and alleviate the requirements to the digital baseband, the MIMO combining block in Figure 3.1 is based on the ZF and MMSE linear receivers, as well as QR-based nonlinear (O)SIC detectors.

In Figure 3.4, we compare the uncoded vs. coded measured BER performance for various types of MIMO combining schemes, including common linear receiver (ZF/MMSE), QRD-based (O)SIC and V-BLAST detectors, as well as sub-optimal K-Best and extensive search ML solutions. As expected, the ML-based solutions clearly outperform the linear and (O)SIC receivers for uncoded transmission. This performance gap however is almost closed in a coded VHDR MB-OFDM system with soft-decision input to channel decoder (see Figure 3.4d)), given the fact that the ML receiver delivers only hard

outputs and thus cannot benefit from the reliability information carried by the Log-Likelihood Ratios (LLRs) in the subsequent processing stage. This result together with the attractive low-complexity of QRD-based receivers has motivated the choice of candidate MIMO schemes for FPGA implementation to the MMSE QRD-based linear and sorted SIC receivers, see Section 5.2 and 5.3 for further details.

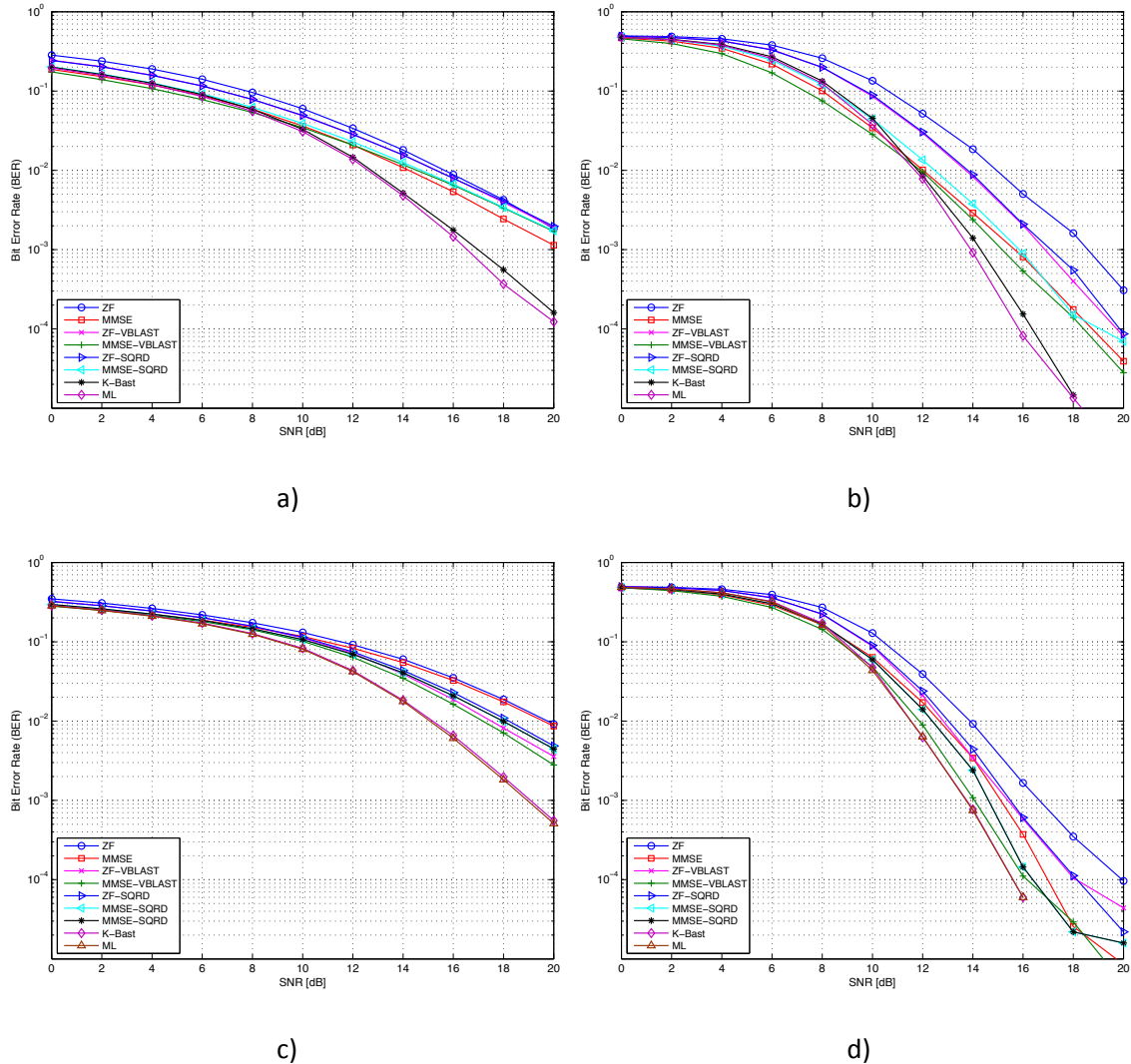


Figure 3.4: Measured BER performance of uncoded vs. coded 3×4 MIMO MB-OFDM with different decoders in 1m LOS a,b) HDR ($R_c = 3/4$, DCM) and c,d) VHDR ($R_c = 1/2$, 16-QAM).

3.3.4 MIMO Decoding for Diversity Schemes

STFC implies that the symbols are usually decoded by a Maximum Likelihood algorithm at the RX, applying an extensive search over all possible combinations of transmitted constellation pairs. While being optimal in terms of achievable performance, the ML becomes prohibitively complex for higher order modulation schemes like 16-QAM, where a total of $16^4 = 65536$ possible constellation pairs have to be searched for in a system with e.g. 4 TX antennas. Another disadvantage of ML is that it provides only hard-decision output, thus preventing the succeeding channel decoder from exploiting any reliability information of the incoming bits.

For orthogonal STFC codes, combining at the receiver is substantially relaxed, as the symbols on a given subcarrier can be decoded independently from all other tones, using mostly simple linear equations, see Section 5.4 for more details. Note that the deployment of STFC schemes to OFDM is straightforward and performed on subcarrier basis, preceding the actual OFDM modulation. Recalling that channel coding in OFDM-based systems essentially introduces frequency diversity, further encoding of the information tones on different independent spatial pipes increases the degree of freedom proportional to the product of the number of TX and RX antennas.

Chapter 4

System Design of a MIMO MB-OFDM System

4.1 Concept of a Modular MIMO-UWB System

The general concept of a MIMO-UWB wireless system is based on an ECMA-368 MB-OFDM conform data-path simulator and an offline MIMO-UWB test-bed featuring multiple antennas on both sides of the communication link. The block diagram of this modular system including digital signal processing in MATLAB and real-air interface via the test-bed is shown in Figure 4.1.

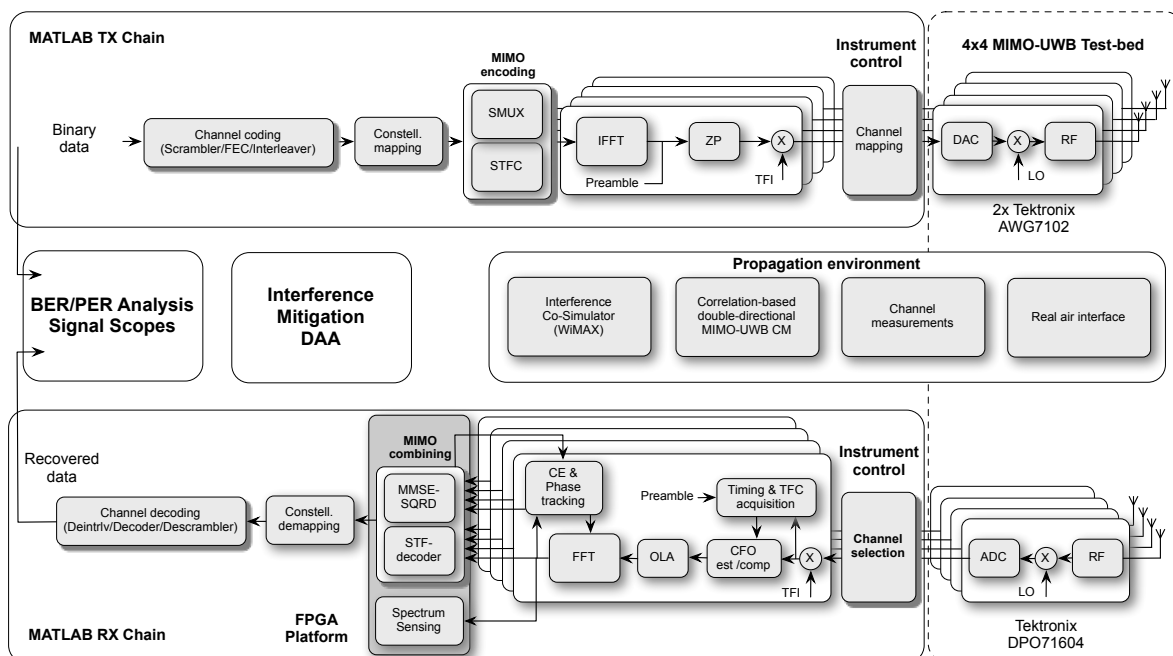


Figure 4.1: General concept of a modular MIMO MB-OFDM system.

Depending on the specific deployment scenario, the selected MIMO scheme can thus be developed under the common MATLAB environment, easily uploaded to the MIMO test-bed, transmitted over the air, and finally verified under the effects of real-world constraints. While this approach preserves the flexibility and modularity of algorithm development, it facilitates the extensive research on and evaluation of the achievable performance gains by employing multiple antennas under realistic propagation conditions.



In the evolved set-up of the MIMO-UWB test-bed, the transmitter is composed of two Tektronix AWG7102 arbitrary waveform generators (AWGs), each one supporting two channels with up to 10 GSPS, 5.8 GHz analog bandwidth and 32 mega sample (MS) waveform length per channel. The AWG enables the direct generation of RF signals, via the DAC, up to the effective frequency of 5.8 GHz and offers the capability to add real world signal imperfections. The direct generation of IF or RF signals avoids I/Q degradations and time-consuming adjustments associated with traditional methods using I/Q modulators.

On the receiver side, a Tektronix DPO71604 digital phosphor oscilloscope (DPO) provides 4 channels with up to 50 GSPS per channel and 16 GHz analog frequency span. Among its time-, spectral and PSD testing capabilities, the DPO has been mainly utilized to reliably capture the transmitted MIMO waveforms for further offline processing and algorithm verification in MATLAB.

In case of spatial multiplexing, multiple independent data lines are generated in the transmitter and uploaded to the AWGs in order to linearly increase the spectral efficiency of the system. The waveform generator directly converts the input I/Q streams to IF/RF signals to be synchronously transmitted over the channel. These signals are then acquired by up to four receive UWB antennas, band-pass filtered, amplified, sampled by the high-speed ADCs of the DPO, and transferred back to MATLAB for further processing. Linear receivers such as Minimum Mean Square Error (MMSE), non-linear Ordered Successive Interference Cancellation (O-SIC) receivers, or optimized solutions thereof (e.g. MMSE-based Sorted QR-Decomposition) can thus be easily integrated and evaluated under common programming environment. Alternatively, if one chooses to verify a MIMO diversity scheme like Space-Time-Frequency Coding (STFC) or Singular Value Decomposition (SVD) based power allocation as described in [25], no further hardware changes have to be applied to the test-bed and only the appropriate encoding/decoding algorithm has to be loaded. In addition, modular FPGA platforms featuring designated MIMO algorithms can be easily integrated into the existing MATLAB chain in order to evaluate their performance under realistic channel conditions and HW imperfections.

For such hardware-in-the-loop simulations, we have selected the Xilinx ML605 development board, see Figure 4.2, featuring high-speed Virtex6 FPGA (XC6VLX240T) with sufficiently large memory and convenient interface to the MATLAB host PC. This approach allows considerably faster processing of the selected algorithms on FPGA, irrespective of the slow MATLAB computations in the rest of the signal chain. The proposed MIMO detection algorithms in Chapter 5 have been implemented by partner VTT of the EUWB FP-7 Integrated Project, using the VHDL language and Xilinx System Generator. The design exploits the hardware-friendly parallel fixed-point logic and deep pipelining to maximize the throughput of the system. Notes on the implementation complexity and resource utilization are summarized in Section 5.6.4 and revealed in detail in [26].



Figure 4.2: Xilinx ML605 development board with Virtex 6 XC6VLX240T FPGA.

4.1.1 System Level Considerations

4.1.1.1 Link Budget and Coverage of MIMO MB-OFDM

The successful design of any high data rate wireless system relies on the careful examination of the various factors and technical requirements which should be traded off to realize a given cost and level of reliability for a communications link. Given the worldwide UWB regulations, the selection criteria and the Ultra-wideband indoor *Path-Loss Model* specified by the IEEE 802.15.3a TG channel modelling committee [15], the link budget of the proposed MIMO MB-OFDM system takes into account the allowed power level of transmission for UWB devices, the path-loss attenuation and possible implementation losses at the RX side. The total transmit power within e.g. Band Group 1 (3.168 GHz to 4.752 GHz) can be adopted directly from the FCC and European spectrum regulations, which restrict the PSD of the transmitted UWB signal in 1-MHz bandwidth to -41.25 dBm

$$P_T = -41.25 + 10 \log_{10}(f_U - f_L), \quad [\text{dBm}] \quad (4.1)$$

with f_L and f_U being the lower and upper frequency of the instantaneous frequency band of transmission. Note that according to current regulation in Europe, frequency-hopping UWB devices are allowed to transmit with the maximum allowed power of -9.3 dBm in the mandatory Band Group 1, provided they are able to apply flexible Detect-And-Avoid (DAA) techniques.

According to Friis' transmission equation, the *free-space path loss* describes the large scale fading of the transmitted power

$$PL(f_g, d) = 20 \log \left(\frac{4\pi f_g d}{c} \right), \quad (4.2)$$

where $f_g = \sqrt{f_L f_U}$ is the geometric mean of f_L and f_U , d is the distance between TX and RX, and c is the speed of light. It is obvious that the path loss is directly proportional to the distance d

raised to a path loss exponent γ , which in the case of free space equals 2. In general, the path loss is given as

$$PL(d) = PL_0 + 10\gamma \log_{10}\left(\frac{d}{d_0}\right) + S(d), \quad [\text{dB}], \quad (4.3)$$

where PL_0 is the fixed intercept point of the path loss at $d_0=1$ m, and $S(d)$ is the lognormal shadowing fading component.

The statistical path loss model derived in [15] further treats the path loss exponent $\gamma \propto \mathcal{N}(\mu_\gamma, \sigma_\gamma)$ and shadowing standard deviation $\sigma \propto \mathcal{N}(\mu_S, \sigma_S)$ as normally distributed random variables, which can be modelled depending on the propagation environment (LOS or NLOS) and indoor location: $\gamma = \mu_\gamma + n_1\sigma_\gamma$, $\sigma = \mu_S + n_3\sigma_S$ and $S = n_2\sigma$, where $n_1, n_2, n_3 \propto \mathcal{N}(0,1)$ are zero-mean Gaussian variables. Table 4.1 summarizes the main parameters of the statistical path loss model in (4.3).

Table 4.1: Main parameters of the WPAN IEEE 802.15.3a statistical path loss model in [15].

Parameter	LOS	NLOS
PL_0 (dB)	47	50.5
μ_γ	1.7	3.5
σ_γ	0.3	0.97
μ_S	1.6	2.7
σ_S	0.5	0.98

Assuming further isotropic antennas with zero transmit and receive antenna gain ($G_T = G_R = 0$ dBi), the received signal power in dBm is

$$P_R = P_T + G_T + G_R - PL(d). \quad [\text{dBm}] \quad (4.4)$$

The link budget of the MIMO MB-OFDM system can therefore be derived from the definition of the Noise Figure (NF) of the receiver, i.e.

$$NF = 10 \log_{10} \left(\frac{SNR_{in}}{SNR_{out}} \right), \quad [\text{dB}] \quad (4.5)$$

where $SNR_{in} = P_R / P_N$ is the Signal-to-Noise Ratio (SNR) at the receive antenna input, and $SNR_{out} = (E_b R_{bit}) / (N_0 W)$ is the required SNR necessary for the RX to achieve the required level of reliability in terms of BER. Note that for MIMO transmissions, the value of SNR_{in} is typically $10 \log_{10}(N_T)$ dB lower than that of the corresponding of a single-antenna system.

The term $P_N = kTB$ stands for the thermal noise power at the RX with $k = 1.38 \times 10^{-23} \text{ J/K}$ being the Boltzman's constant, $T = 290\text{K}$ the system room temperature. The instantaneous channel- and signal bandwidth are denoted by B and W , respectively. Note that the primary sources for the NF are the Low Noise Amplifier (LNA) and mixer at the receiver RF front-end. Including the losses associated with the pre-select band-pass filter and transmit/receive switch, a typical NF of the proposed system accounts for 6.6 dB [7].

Assuming the measured channel bandwidth equals the system bandwidth ($B = W$), the receiver sensitivity $P_{R,\min}$ is given as

$$P_{R,\min} = 10 \log_{10} \left(\frac{E_b}{N_0} \right) + 10 \log_{10}(kT) + 10 \log_{10}(R_{bit}) + NF + I, \quad [\text{dBm}] \quad (4.6)$$

where the Implementation Loss (I) component has been included to account for the losses due to ZP overhead, front-end filtering, clipping of the DAC, channel estimation, clock frequency mismatch, carrier offset recovery and further imperfections at the receiver [7].

The ratio E_b / N_0 of the energy per bit to noise power spectral density is calculated based on the SNR (average power of the OFDM waveform divided by the noise power) as

$$\frac{E_b}{N_0} = SNR \frac{f_s}{R_b} \frac{N_{\text{info}}}{N_{\text{info}} + N_{\text{pil}}} G_{\text{TFC}} G_{\text{MIMO}} = SNR \frac{G_{\text{TDS}} G_{\text{FDS}}}{m R_c} \frac{N_{\text{FFT}} + N_{\text{ZP}}}{N_{\text{info}} + N_{\text{pil}}} G_{\text{TFC}} G_{\text{MIMO}}, \quad (4.7)$$

where m is the number of bits per modulated tone, R_c is the code rate after puncturing, R_b the data rate, G_{TDS} and G_{FDS} are the time- and frequency domain spreading factors. The number of user data and pilot sub-carriers in a MB-OFDM symbol is denoted by N_{info} and N_{pil} respectively, whereas N_{FFT} and N_{ZP} stand for the length of the FFT and ZP. The factors G_{TFC} and G_{MIMO} reflect the gains due to frequency hopping and MIMO coding ($G_{\text{MIMO}} = 3/4$ in case of STFC with $N_T = 3, 4$, and $G_{\text{MIMO}} = 1$ otherwise) in the system.

Finally, the Link Margin (M) of the system is calculated as the difference of the actual received signal strength and the receiver sensitivity

$$M = P_R - P_{R,\min} \quad [\text{dB}] \quad (4.8)$$

and corresponds to the degree of freedom, or excess signal strength available in the system, which is required to perform reliable detection and overcome the losses due to multipath fading. Figure 4.3 shows the PER performance of 160 Mbps HDR Mode in CM1 as function of the maximum achievable distance and number of antennas in a spatially multiplexed system. Note that the distance has been calculated using the path loss model described above and the minimum required E_b / N_0 to achieve a Frame Error Rate (FER) of 8% over the best 90% of 100 CM1 realizations. While the coverage of

symmetric MIMO systems is decreased as compared to the SISO case due to the lower instantaneous SNR, each additional receive antenna delivers both array gain and substantial diversity gains. These reduce the sensitivity level of the MIMO system and therefore allow for significantly improved coverage, whereas spatial multiplexing still provides the linear increase in spectral efficiency.

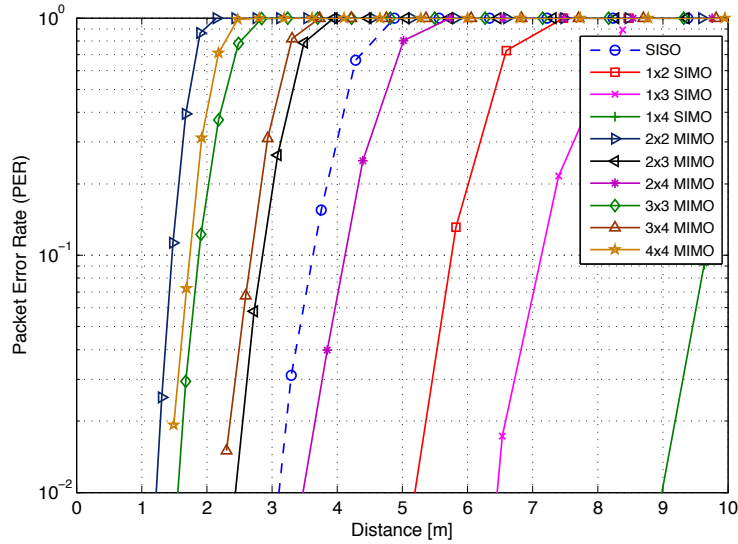


Figure 4.3: PER of MB-OFDM as function of the achievable distance in CM1 for different antenna configurations ($R_c = 1/2$, QPSK).

Table 4.2 summarizes the main results of the link budget analysis for various HDR modes in AWGN channel. It can be concluded that the excess link margin and RX sensitivity levels for the different data rate modes are sufficiently high to guarantee reliable detection at the receiver.

Table 4.2: Link budget of HDR MB-OFDM in AWGN

Data rate R_b (Mbps)	160	200	320	400	480
Total TX Power P_T (dBm)	-9.3	-9.3	-9.3	-9.3	-9.3
Path Loss $PL(d)$ (dB)	64.2 @10m	56.2 @4m	56.2 @4m	56.2 @4m	56.2 @4m
RX Power P_R (dBm)	-73.5	-65.5	-65.5	-65.5	-65.5
Total Noise Power (dBm)	-85.3	-84.4	-82.3	-81.4	-80.6
RX Noise Figure NF (dB)	6.6	6.6	6.6	6.6	6.6
Required E_b/N_0 (dB)	6.9	7.4	7.0	7.4	7.7
Implementation Loss I (dB)	2.5	2.5	2.5	2.5	2.5
RX Sensitivity $P_{R,min}$ (dBm)	-75.9	-74.5	-72.8	-71.5	-70.4
Link Margin M (dB)	2.5	9.0	7.3	6.0	4.9
Maximum distance d_{max} for $M = 3$ dB	9.4	8.0	6.6	5.7	5.0

Table 4.3 summarizes the main results of the link budget calculation for VHDR MB-OFDM under real MIMO channel conditions over 1m LOS and 800 Mbps, 960 Mbps, and 1280 Mbps data rate per antenna branch. It can be concluded that the excess link margin and RX sensitivity levels for the different data rate transmission modes are sufficiently high to guarantee reliable detection at the receiver.

Table 4.3: Link budget of VHDR MB-OFDM in 1m LOS

Data rate R_{bit} (Mbps)	800	960	1280
Total TX Power P_T (dBm)	-11	-11	-11
Path Loss P_L at 1m (dB)	44	44	44
RX Power P_R (dBm)	-55	-55	-55
Total Noise Power (dBm)	-85	-84	-83
RX Noise Figure NF (dB)	7	7	7
Required E_b/N_0 (dB)	10	11	12
Implementation Loss I (dB)	3	3	3
RX Sensitivity $P_{R,min}$ (dBm)	-65	-63	-61
Link Margin M (dB)	10	8	6

4.1.2 System Parameters and Frame Structure

In VHDR mode operation, the system bandwidth can be virtually increased in two ways. One approach is to double the FFT size and number of information tones per symbol, while preserving the symbol duration and length of the ZP [27]. With the aim to increase the capacity of the existing WiMedia standard, the instantaneous bandwidth and FFT size of the VHDR MB-OFDM mode has been doubled to 1056 MHz and 256-pt respectively. This combined scaling of the main parameters of the HDR mode (528 MHz and 128-pt FFT) preserves the frequency separation between the sub-carriers as well as the overall time duration of the MB-OFDM signal and ZP part of it.

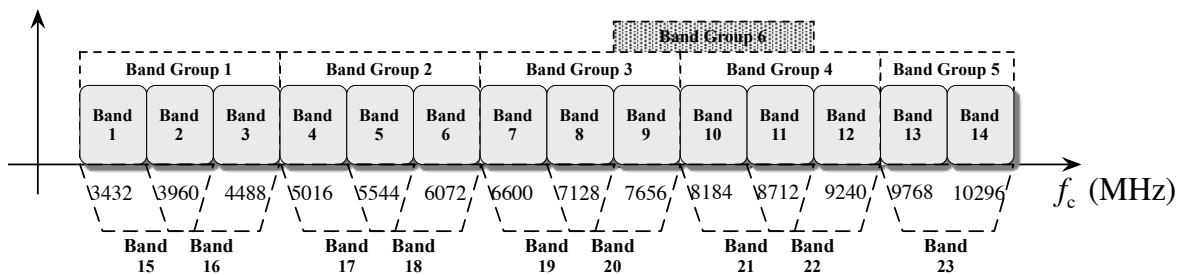


Figure 4.4: VHDR frequency band plan

Table 4.4 gives an overview of the core parameters of the described MB-OFDM system. Because of the doubled bandwidth of the system, an extended VHDR MB-OFDM frequency band plan has been proposed. In this way, two adjacent sub-bands are grouped together in 1-GHz-wide overlapping bands within a BG, as illustrated in Figure 4.4. Note as well that the VHDR mode assumes no frequency hopping.

Further, the preamble structure of the proposed MIMO VHDR MB-OFDM has been adopted from the HDR mode of the ECMA-368 PHY by doubling the size of the MB-OFDM symbol to 330 samples. Each frame consists of a preamble part, a PLCP header and payload data. The preamble itself comprises 21 time domain packet synchronization (PS) symbols to aid the coarse time acquisition at the receiver, 3 fine frame synchronization (FS) and 6 symbols for channel estimation (CE). The 330-samples long PS symbols are constructed in the time domain either by resampling the HDR PS symbols, each generated from a PN sequence of 8x16 samples with the corresponding ZP, by factor 2. The PS sequence has to exhibit good autocorrelation properties and is uniquely specified for each TFC, i.e. logical channel.

Table 4.4: Timing- and rate dependent parameters of HDR/VHDR MB-OFDM

Parameter	HDR mode						VHDR mode					
Symbol rate (Msymb/s)	3.2						6.4					
Channel bit rate (Mbps)	640						1280			2560		
Information rate (Mbps)	106.7	160	200	320	400	480	640	800	960	1280	1600	1920
Code rate	1/3	1/2	5/8	1/2	5/8	3/4	1/2	5/8	3/4	1/2	5/8	3/4
TDS/FDS factor	2/1			1/1			1/1					
Modulation	QPSK			DCM			QPSK			16-QAM		
Instantaneous BW (MHz)	528						1056					
FFT size (pt)	128						256					
Number of data tones	100						200					
Number of pilot ones	12						24					
Number of guard ones	10						20					
Samples per OFDM symbol	165						330					
ZP samples	37						74					
Subcarrier spacing (MHz)	4.125						4.125					
ZP duration (ns)	70.08						70.08					
Guard interval (ns)	9.5						9.5					
FFT period (ns)	242.42						242.42					
MB-OFDM symbol duration (ns)	312.5						312.5					

As described in Section 3.2.2, *dual mode* is an effective scheme to virtually double the instantaneous bandwidth of the system, by interleaving the data signals on two independent RF branches and up-converting them to different (not necessarily adjacent) sub-bands or even whole band groups. In compliance with worldwide regulations on frequency allocation for UWB devices in Europe, the developed MIMO VHDR MB-OFDM system supports dual mode transmission in two parallel band groups. The lower BG1 (3168 MHz – 4752 MHz) is the mandatory frequency band for operation of Mode 1 WiMedia devices, while BG6 (7392 MHz – 8976 MHz) is intended to enable worldwide support for next-generation UWB devices.

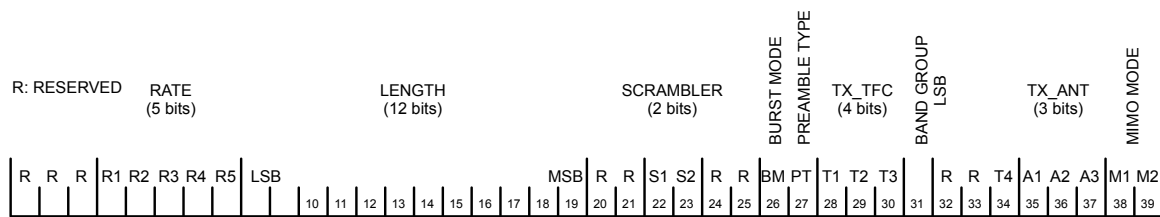


Figure 4.5: PHY Header bit assignment

Figure 4.5 depicts the extended PHY header assignment proposed to support MIMO transmission. Depending on the data rate (RATE), we propose to set the reserved bits R1-R5 according to the values given in Table 4.5. The motivation behind modifying the PHY header of the ECMA-368 standard lies in the fact that the RX has to acquire the number of TX antennas before MIMO combining. Alternative approach is to define orthogonal preamble sequences for each TX antennas and correlate them in parallel during synchronization in order to obtain the number of transmit branches.

Table 4.5: Bit assignment for rate-dependent parameters

Rate (Mbps)	Transmission mode	R1- R5
53.3	HDR	00000
80	HDR	00001
106.7	HDR	00010
160	HDR	00011
200	HDR	00100
320	HDR	00101
400	HDR	00110
480	HDR	00111
640	VHDR	01100
800	VHDR	01101
960	VHDR	01110
1280	VHDR	01111
1600	VHDR	10000
1920	VHDR	10001

In Table 4.6, the supported MIMO configurations and PHY header bit assignment for the HDR and VHDR mode are specified.

Table 4.6: Supported MIMO modes

Mode (ID)	N_T	N_R	A1-A3 (R35-R37)	M1-M2 (R38-R39)	Data rate		Remark
					HDR	VHDR	
1	1	1	000	00	480	960	Reference mode
2	2	2	100	00	960	1920	Dual mode
3	3	4	010	00	1440	2880	SMUX
4	4	2	110	10	480	960	STFC

4.1.2.1 Standard Frame Structure and MIMO Preamble Design

The ECMA-368 PHY layer specification defines two types of PPDU frames structures for *standard* and *burst* mode transmission, respectively. Each frame in standard (burst) mode consists of a 30 (12) symbol long PLCP preamble part, a PLCP header and payload data. The standard frame structure of MB-OFDM transmissions is shown in Figure 4.6.

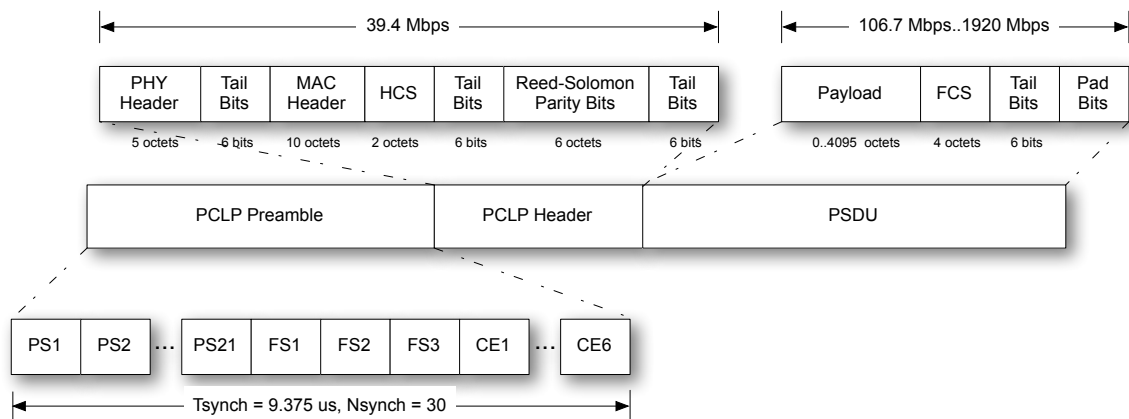


Figure 4.6: Standard PPDU frame structure

In standard mode, the preamble comprises $N_{PS} = 21$ time-domain packet synchronization (PS) symbols to aid coarse time acquisition at the receiver, $N_{FS} = 3$ fine frame synchronization (FS) and $N_{CE} = 6$ symbols for channel estimation (CE). For burst mode, the value of N_{PS} is equal to 9. The PS sequence has to exhibit good autocorrelation properties and is uniquely specified for each TFC, i.e. logical channel, such that the RX is able to reliably determine the TFC by means of e.g. matched filtering.

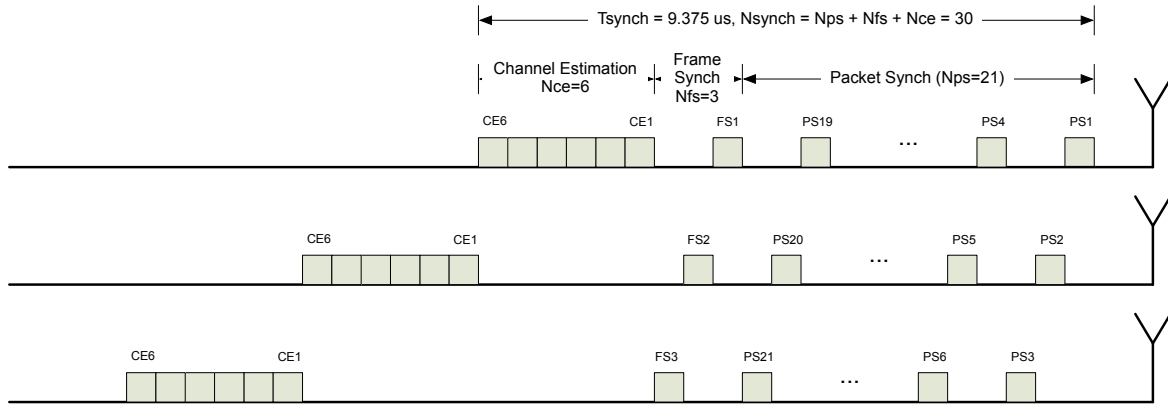


Figure 4.7: MIMO PLCP preamble transmission

Since any OFDM-based system is very sensitive to time-drifts and especially to frequency offsets which disturb the orthogonality of its carriers, robust and quick synchronization at the receiver is a prerequisite for good quality of the communication link.

To estimate the wireless MIMO channel and ensure that the separate channels between each antenna pair can be reliably estimated, the CE symbols to be transmitted over different antennas should be orthogonal and shift-orthogonal. One simple way to achieve this is to adopt an orthogonal transmission scheme in one or more dimensions, e.g. in time, as shown in Figure 4.7. This approach may be interpreted as TX antenna switching during preamble transmission.

In order to estimate the channel effect and possible frequency offsets for each sub-band and channel link, a periodicity in the preamble is also desired to provide time-delayed versions of the same preamble symbol for better estimation of the phase rotation and CFO. The proposed long preamble sequence of length $N_{PS} + N_{FS} + N_T N_{CE}$ is a concatenation of the standard $N_{PS} + N_{FS}$ synchronization sequence and N_T channel estimation sequences, at least two per sub-band and MIMO link. Due to the induced overhead, one may further consider e.g. complementary or space-frequency encoded CE sequence.

4.1.2.2 Supported Frequency Range

Since most of the envisioned UWB applications described in Chapter 5 are supposed to operate world-wide, the MIMO (V)HDR system must preferably support operation within overlapping frequency bands. Following the current regulatory status and frequency allocation for UWB MB-OFDM-based devices across the world [10], see Figure 4.8, we have chosen two separate Band Groups for test and measurements using the MIMO-UWB test-bed as described in Section 6.1. The lower one, Band Group 1 (3168 MHz – 4752 MHz), is the mandatory frequency band for operation of Mode 1 WiMedia devices. Due to the huge analog bandwidth (5.8 GHz) of the arbitrary waveform generators on the transmit side, this lower Band Group can be covered using RF direct signal synthesis, without an additional up-conversion circuitry.

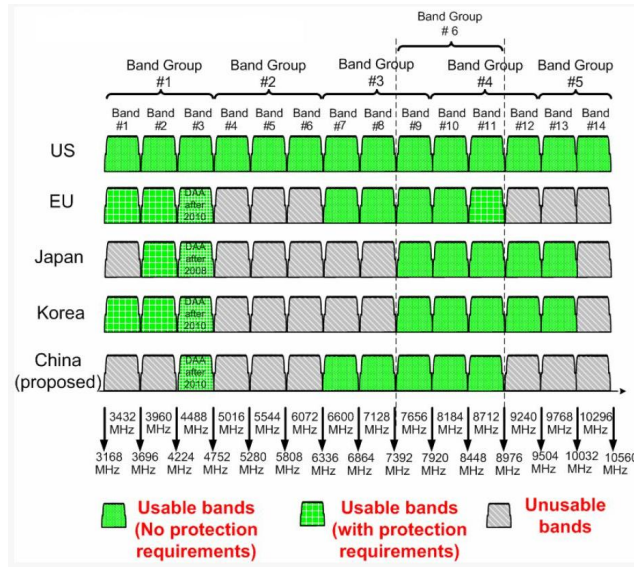


Figure 4.8: Worldwide frequency allocation for UWB devices according to [10]

On the other hand, Band Group 6 (7392 MHz – 8976 MHz) is intended to enable worldwide support for next-generation UWB devices. Signal generation using our arbitrary waveform generators in this frequency band requires additional up-conversion and RF front-ends. By covering both band groups we ensure conformity with state-of-the-art measurement set-ups for WiMedia devices, as well as enable test and verification capabilities for next-generation UWB solutions and dual mode operation.

Table 4.7: Band group allocation for BG1 and BG6

Band Group	Band ID	Lower frequency (MHz)	Center frequency (MHz)	Upper frequency (MHz)
1	1	3168	3432	3696
	2	3696	3960	4224
	3	4224	4488	4752
6	9	7392	7656	7920
	10	7920	8184	8448
	11	8448	8712	8976

The supported Band Groups and Time-Frequency Codes are adopted from the ECMA-368 PHY standard and are listed in Table 4.7 and Table 4.8 respectively.

Table 4.8: Supported Time-Frequency Codes for BG1 and BG6.

TFC	Band ID for TFC in BG1						Band ID for TFC in BG6					
	1	1	2	3	1	2	3	9	10	11	9	10
2	1	3	2	1	3	2	9	11	10	9	11	10
3	1	1	2	2	3	3	9	9	10	10	11	11
4	1	1	3	3	2	2	9	9	11	11	10	10
5	1	1	1	1	1	1	9	9	9	9	9	9
6	2	2	2	2	2	2	10	10	10	10	10	10
7	3	3	3	3	3	3	11	11	11	11	11	11
8	1	2	1	2	1	2	9	10	9	10	9	10
9	1	3	1	3	1	3	9	11	9	11	9	11
10	2	3	2	3	2	3	10	11	10	11	10	11

4.2 Basic Signal Processing Blocks

In this section, we describe the basic signal acquisition and baseband processing blocks comprising the MIMO MB-OFDM receiver. Special attention has been paid to the analysis and development of reliable time- and frequency acquisition schemes, including algorithms for estimation and digital compensation of incurred RF frontend imperfections.

4.2.1 Robust Synchronization of Time-Frequency Interleaved Signals

While OFDM systems in general are known to efficiently collect the multipath energy and enable ISI-free detection, they are still sensitive to synchronization errors, which can degrade the orthogonality of the sub-carriers and lead to detrimental Inter-Carrier Interference (ICI). In addition, frequency-hopping systems require fast and robust synchronization of the RX local oscillator (LO) switching circuit, as locking to a false TFC may fully degrade the system performance. In the following, we therefore analyse and provide specific implementation notes on the robust synchronization of time-frequency interleaved signals, including TFC- and timing acquisition.

The inherent task of the synchronization block in Figure 4.1 is to detect the arrival of a transmitted packet by correlating the received preamble symbols with the unique packet synchronization (PS) sequence for each TFC. Besides detecting the presence of a signal, it has to provide coarse estimates of the symbol and frame boundaries, as well as to acquire the TFC of transmission. In particular, the synchronization and CFO estimation blocks have to provide estimates of the symbol timing offset (STO), frequency hopping offset (FHO) and Carrier Frequency Offset (CFO), so that the receiver can properly adjust its oscillator and FFT window for successive payload demodulation. Here, the FHO is defined as the timing offset of the actual RX LO hopping sequence with regards to the ideal (transmit) time-interleaving pattern, see Figure 4.9. The STO on the other hand corresponds to the

timing delay (in samples) caused by the multipath propagation channel or any latency introduced by the TX/RX front-ends.

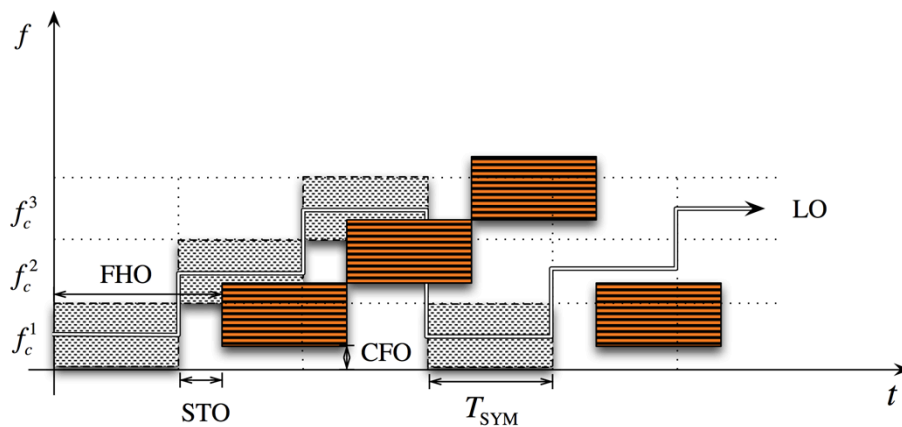


Figure 4.9: Synchronization of time-frequency interleaved signals.

The majority of coarse time-synchronization algorithms for OFDM-based systems rely on the auto-correlation between two adjacent symbols (or in general two identical parts of a preamble symbol, e.g. in case of a cyclic prefix) of the preamble sequence [28], [29]. These approaches, however, need to be adapted for use in MB-OFDM systems as the RX may have no a-priori knowledge of the frequency hopping pattern, e.g. during the beaconing period or when a new device joins a piconet. Synchronization schemes based on differential auto-correlation metric as in [30]-[32] can therefore be applied only after the RX LO has been aligned to the correct time-interleaving sequence and FHO. The TFC acquisition therefore still requires additional parallel correlation blocks for all possible TFCs or preceding cross-correlation with the known PS sequence. Otherwise, in the worst case of a FHO equalling multiple of the symbol duration T_{SYM} , the RX baseband can ‘see’ only small or no portions of preamble, leading to synchronization failure or locking to a false TFC. In such a case, the two adjacent MB-OFDM symbols (or symbol parts) may not be both correctly down-converted to baseband causing degradation of the decision metric.

The main requirements and challenges for the robust synchronization of a non-trivial time-frequency interleaved MB-OFDM are summarized below:

- reliable acquisition of the TFC and FHO,
- fast synchronization and switching of the LO center frequency within the PLCP preamble duration and prior to channel estimation,
- low receiver sensitivity and higher noise immunity,
- feedback from baseband to the RF circuit to control the time-frequency interleaving,
- low digital HW complexity – due to hopping, several parameters shall be estimated for each sub-band separately, for example: automatic gain control (AGC), channel state information

(CSI), group delays and CFOs. Other parameters may be jointly estimated, but must be corrected per band, for example frequency- or timing drifts.

Figure 4.10 shows the flow chart of the proposed coarse timing and TFC acquisition per RX antenna branch. Here, we strictly differentiate among the following acquisition stages:

- *down-conversion* to baseband - in the non-trivial case of unknown TFC, the RX LO switches every T_{SYM} seconds randomly across the center frequencies of the sub-bands within a Band Group to minimize the probability of ‘hidden’ symbols. In fact, one may define a fixed hopping pattern for the LO switching, which highly correlates with all possible TFCs during preamble reception.
- introducing *imperfections* at RX down-conversion branch – these include e.g. phase noise, I/Q mismatch, CFO as described in Section 4.2.4.
- *TFC detection and coarse time acquisition* using a cross-correlation approach – in case the TFC is unknown, the preamble symbols are correlated with the PS sequence of all candidate TFCs for a given BG and the TFC with the highest metric exceeding a normalized threshold is selected. In case of successful TFC acquisition, the coarse STO is determined as the position of the highest metric. Once the TFC and coarse symbol timing have been found, the RX can start with the CFO estimation and search for the optimal frame border. Otherwise, the synchronization proceeds with the next preamble symbol and stays within the TFC detection loop until successful TFC acquisition or detection failure have been declared, or the preamble length has been exceeded.
- *fine symbol- and frame synchronization* – after TFC and STO acquisition, the coarse symbol timing has to be refined and the border of the received frame needs to be detected. This can be achieved by e.g. auto-correlating two correctly down-converted symbols of the same sub-band and tracking the polarity of the correlation metric to match the cover sequence of the detected TFC. The differential metric proposed in [29],[32] suits well for this tasks, as it avoids a plateau in the correlation output and minimizes the ambiguity in detecting the first multipath component in case of highly dispersive NLOS channels. Successful frame synchronization automatically corrects any hopping misalignment (FHO) and guarantees proper down-conversion and CFO compensation of the CE-, header and payload part of the frame.
- *CFO compensation* – once the frame has been synchronized and a coarse estimate of the CFO has been acquired, the data symbols are multiplied by the complex term $e^{j2\pi n\hat{\Delta f}_l T_s}$, where $\hat{\Delta f}_l$ stands for the coarse estimate of the CFO for a given sub-band l .

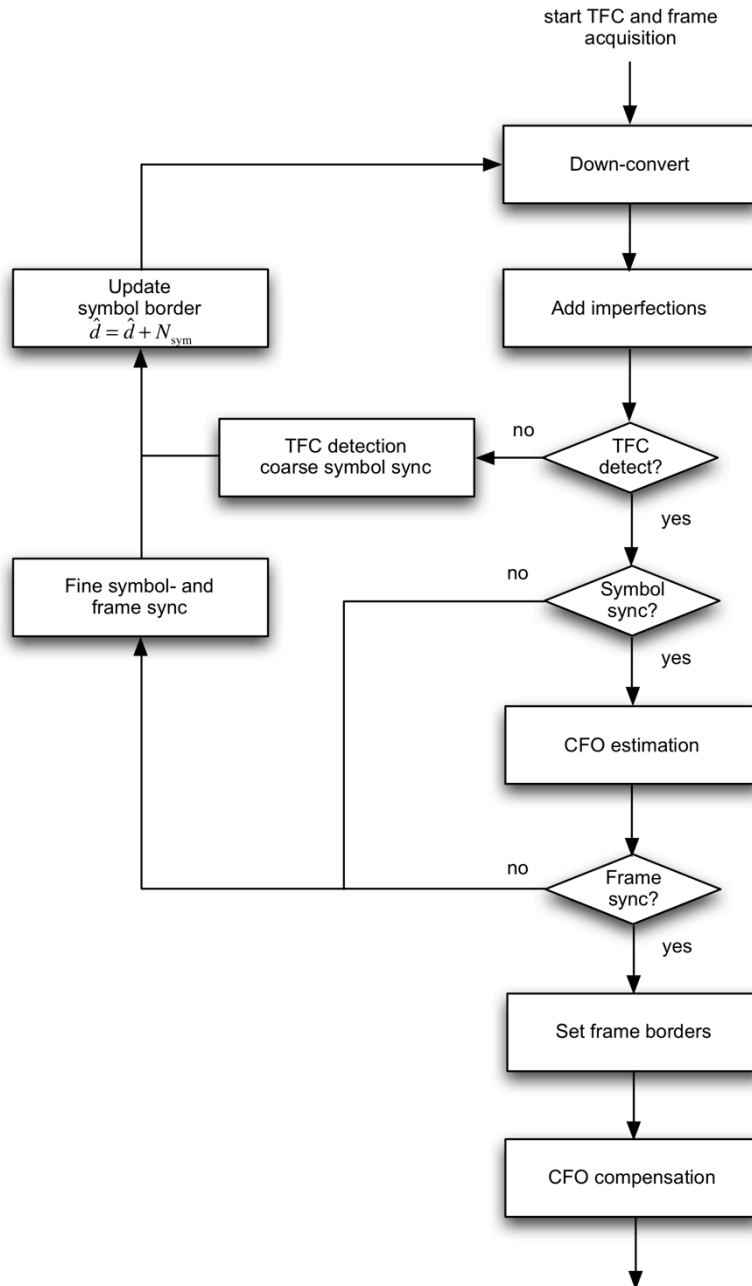


Figure 4.10: Coarse time- and TFC acquisition per RX branch.

Since the PS preamble symbols are uniquely defined for a given TFC, the PS and FS sequences not only serve to determine a coarse estimate of the frame boundary, but also contain the information necessary to acquire the time-frequency hopping pattern of the received signal. Due to this property, we design our synchronization block based on the cross-correlation function (CCF) of a received preamble with the known PS sequence. The CCF metric has been normalized by the power metric of the combined PS symbols for each candidate TFC k as

$$0 \leq M_k(d) = \frac{|A_k(d)|^2}{B_k^2(d)} \leq 1 \quad (4.9)$$

$$\text{with } A_k(d) = \sum_{n=0}^{N-1} s_k^*(d) r_k(d+n) \text{ and } B_k(d) = \sum_{n=0}^{N-1} |r_k(d+n)|^2.$$

The term $A_k(d)$ corresponds to the cross-correlation of the combined received preamble symbol \mathbf{r}_k with the known transmitted PS symbol \mathbf{s}_k for a given TFC k . The moving power meter $B_k(d)$ is calculated over a correlation window length equalling the size of the FFT N . In the case of pure noise at the input of the cross-correlator (transmitted signal is not present), the numerator of the above metric will tend to zero. And vice versa, if the channel is ideal and noiseless, the values of the numerator and denominator will become approximately equal. Figure 4.11 shows the block diagram of the CCF metric calculation circuit.

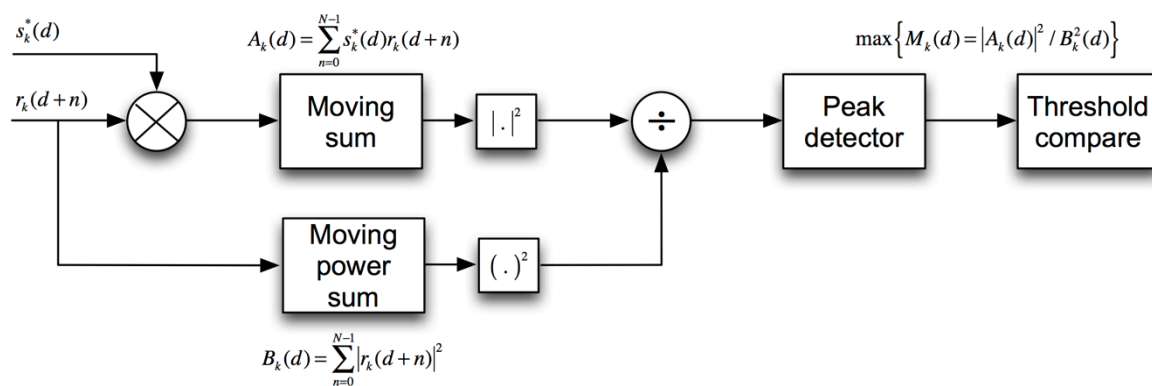


Figure 4.11: Block diagram of CCF metric calculation

As mentioned before, the CCF metric has to be calculated for each candidate TFC, i.e. the preamble coefficients of each TFC have to be correlated with the received symbol, and the TFC leading to the best correlation metric should be chosen as the most probable frequency-hopping pattern of transmission. Figure 4.12 illustrates the data and control flow during TFC detection.

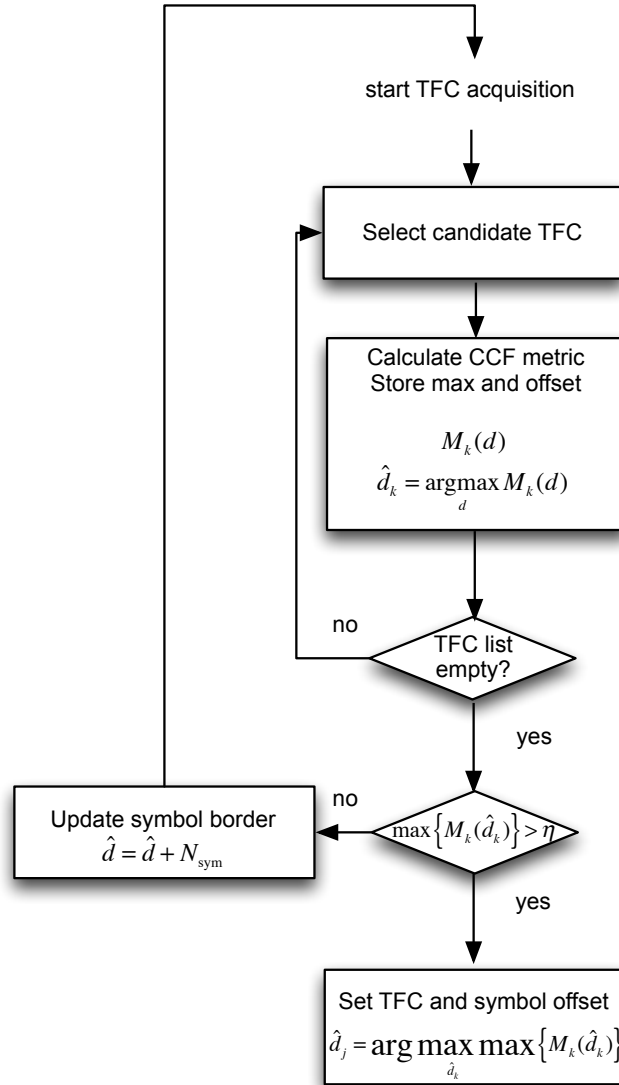


Figure 4.12: Proposed TFC acquisition in a frequency-hopping MB-OFDM system.

At the beginning of TFC acquisition, a candidate TFC k is selected out of a sub-set of possible TFCs matching the frequency band of the current down-converted symbol. After calculating and storing the normalized CCF metric, the TFC detector proceeds with the next possible hopping sequence until the list of candidate TFCs becomes empty. While the maximum of the metric across all k 's stays below a threshold η , the next symbol will be down-converted (possibly from a different sub-band) and the TFC acquisition performed again until $\max\{M_k(\hat{d}_k)\} > \eta$ or the preamble end is reached and detection failure is declared.

After the CCF metric has been calculated, a *metric combiner* (MC) collects the outputs $M_j = \max\{M_k(\hat{d}_k)\}$ and \hat{d}_j from each RX branch j and compares the individual branch metrics in order to set the detected TFC and frame border. In a conventional OFDM system, a simple decision device at the output of the correlator would compare the value of the given metric with a pre-set threshold. This direct approach can be further expanded to benefit from the receive diversity offered

by the use of multiple antennas and alleviate the timing acquisition in severe SNR environments. A straightforward way to achieve this would be to combine the metrics from the N_R receiver synchronization blocks in a uniform or selective manner. Applying e.g. a selection rule, the output of the MC is chosen as the maximum of the metric values found on each antenna branch, i.e. the coarse estimate of symbol timing offset corresponds to

$$\hat{d} = \underset{\hat{d}_j}{\operatorname{argmax}} \{M_j(\hat{d}_j)\}.$$

At this point, the frequency-hopping controller will deliver the detected TFC to the TFI block, and proceed with the fine timing acquisition and frame synchronization.

Although the presented cross-correlation approach introduces more complexity to the system compared to common OFDM synchronization schemes based on auto-correlation, it ensures correct detection of the TFC when the latter is unknown during preamble reception, or when frequency hopping is applied in a HDR transmission.

4.2.2 Synchronization Performance

The performance evaluation of the proposed time- and TFC acquisition is based on the conditional probabilities of *False Alarm* (P_{FA}), *Missed Detection* (P_{MD}) and proper *Detection* (P_{det}), and the following events from [30]

Table 4.9: Conditional probabilities of frame acquisition

Event	Description
U_0	Synchronization block (SYNC) declares <i>free</i> during preamble reception
U_1	SYNC declares <i>busy</i> during preamble reception
G_0	MB-OFDM preamble is <i>not present</i> at the receiver
G_1	MB-OFDM preamble is <i>present</i> at the receiver
$U_1 G_0$	SYNC declares <i>busy</i> , although <i>no</i> preamble has been received, i.e. <i>False alarm</i>
$U_0 G_0$	SYNC declares <i>free</i> while <i>no</i> preamble has been received
$U_0 G_1$	SYNC declares <i>free</i> , although a preamble has been received, i.e. <i>Missed Detection</i>
$U_1 G_1$	SYNC declares <i>busy</i> while a preamble has been received

The conditional performance probabilities are defined as

$$P_{\text{MD}} = P(U_0 | G_1)$$

$$P_{\text{FA}} = P(U_1 | G_0)$$

$$P_{\text{det}} = P(U_1 | G_1)P(G_1) + P(U_0 | G_0)P(G_0),$$

where P_{MD} is the probability that the SYNC block will fail to detect the arrival of a frame, P_{FA} corresponds to the case when it erroneously declares the arrival of a frame, and P_{det} is the probability of error-free frame acquisition. In order to maximize P_{det} , it must be ensured that the values of P_{MD} and P_{FA} are sufficiently low, i.e. P_{det} is greater than a certain level of reliability for a given threshold range $\Delta\eta$, for which more than e.g. 90 % of the frames are detected correctly

$$\Delta\eta = \max\{\eta | P_{\text{det}}(\eta) \geq 0.9\} - \min\{\eta | P_{\text{det}}(\eta) \geq 0.9\}.$$

Note that while P_{det} may not fully reflect the synchronization performance because of its time consuming calculation for values close to 1, the threshold range $\Delta\eta$ provides an easy measure of the functional improvement or degradation of the synchronization block due to minor changes in the system.

As mentioned before, the calculation of P_{det} would require finding the intersection point of the P_{FA} and P_{MD} curves, which is only possible for very large number of simulated frames. This point can also provide the optimal initial level η_0 of the threshold, as it corresponds to the mean of the value for which P_{det} is maximized.

The detection probability curves shown in Figure 4.13 are derived for 10^4 preamble transmissions of size 40 byte, averaged over 100 channel realizations and threshold levels between 0 and 1. In Figure 4.13a), we illustrate the improvement in the threshold range and therefore in the synchronization robustness when deploying multiple antennas in the system. This gain is mainly owed to the reduced uncertainty in finding the maximum correlation peaks across all RX branches, as well as to the intrinsic array gain obtained by the use of multiple antennas. A comparison of the time acquisition performance under harsh SNR conditions and different channel models is further shown in Figure 4.13b). For all CM1-4, the proposed synchronization algorithm is able to reliably (with minimum 90% probability) detect the arrival of a frame well below 0 dB SNR, even for highly dispersive channels such as CM4.

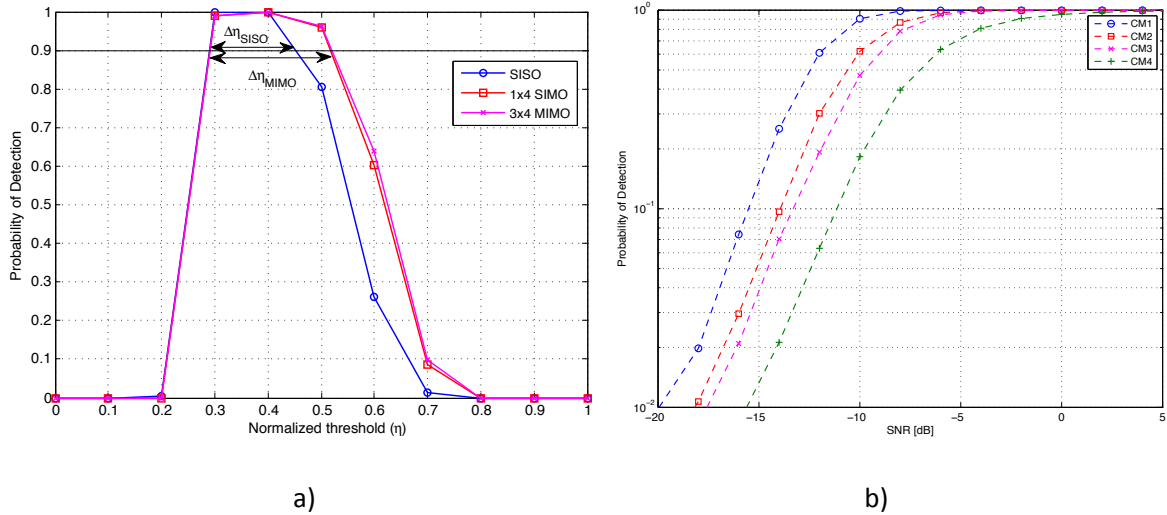


Figure 4.13: Probability of detection for different a) antenna configurations in CM1, and b) channel models CM1-4 (TFC6, SNR=0 dB).

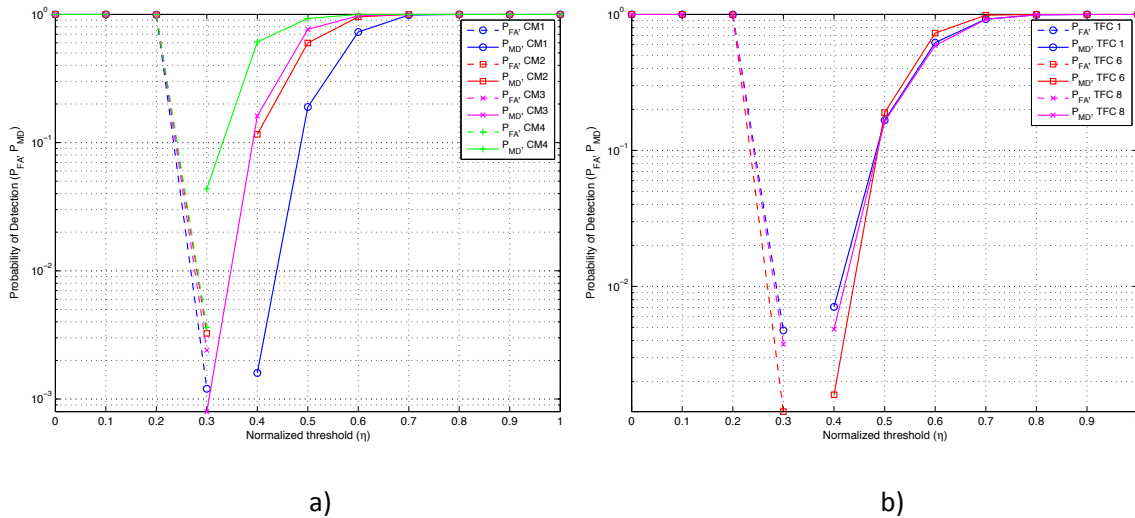


Figure 4.14: Probabilities of false alarm and missed detection a) in CM1-4 for TFC6, and b) in CM1 for different TFCs (SNR=0 dB).

Figure 4.14a) shows the probabilities of false alarm and missed detection for the proposed synchronization scheme in CM1-4 as function of the normalized threshold for a given TFC. In both short-range LOS and NLOS environments, the probability of false alarm and missed detection reach sufficiently low levels for SNR=0 dB. As the TFC is varied in CM1, see Figure 4.14b), the synchronization performance is slightly degraded as the number of sub-bands increases but still ensures reliable detection for a wide range (between ca. 0.2 and 0.6) of threshold values.

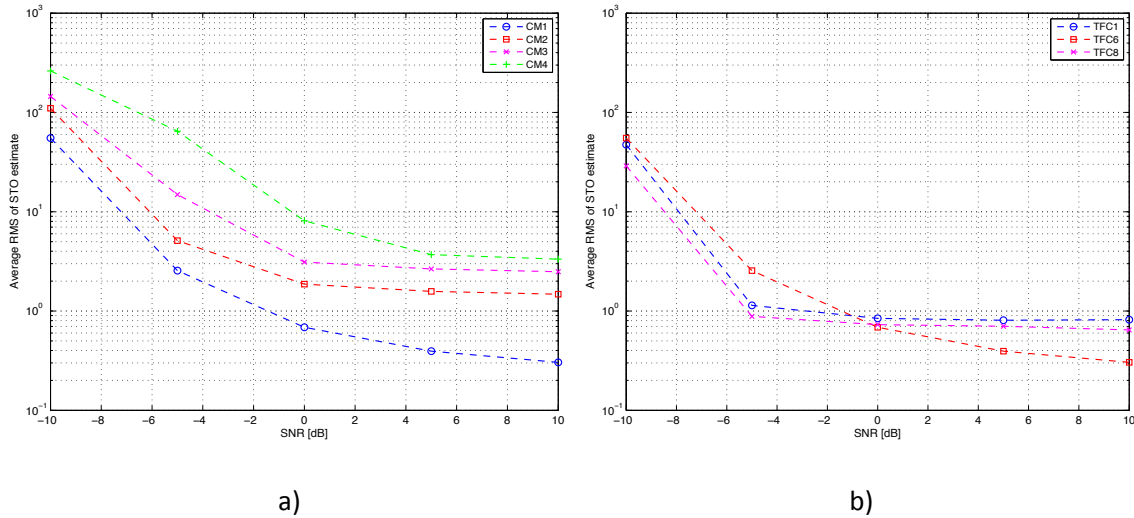


Figure 4.15: Average RMS of STO estimate a) in CM1-4 for TFC6, and b) in CM1 for different TFCs.

In Figure 4.15a), the average root-mean-square (RMS) value of the STO estimate is drawn as function of the received SNR and CM used. For SNR values above 0 dB, the STO does not exceed a few samples even for highly dispersive channels such as CM4. As expected, the synchronization performance is optimal for fixed frequency interleaved systems (e.g. for TFC6), whereas the average STO in frequency-hopping transmission mode exhibits a saturation floor for SNR values above -5 dB, see Figure 4.15b). This is due to the induced uncertainty carried by the different frequency bands, since the synchronization block selects the maximum metric across all RX antennas corresponding to the strongest multipath component, which may not necessarily be the direct path.

4.2.3 Channel Estimation in Frequency-Hopping MIMO-UWB Systems

After successful time- and frequency synchronization, the RX has to estimate the MIMO multipath channel. Since the coherence bandwidth of the UWB channel is reported to be much less than the subcarrier spacing of the OFDM modulated signal, the channel estimation (CE) can be performed on a subcarrier basis using the known CE sequence within the preamble. In addition, due to the coherent nature of a frequency-hopping OFDM system, the amplitude and phase distortion incurred by the channel has to be estimated at the beginning of the acquired MB-OFDM frame for each sub-band and multiple antenna propagation path.

Applying the time-orthogonal MIMO preamble described in Section 4.1.2.1 and denoting the k -th subcarrier of a CE symbol $m = 1 \dots N_{\text{CE}}$ as $D_{ji}(k, m) = D(k)$ for $\forall(i, j, m)$, we rewrite the system model in Eq. (3.2) as

$$\mathbf{Y}(k, m) = \mathbf{H}(k, m)\mathbf{D}(k) + \mathbf{W}(k, m) \quad (4.10)$$

$$\text{with } \mathbf{Y}(k,m) = \begin{pmatrix} Y_1(k,m) & Y_1(k,m+N_{\text{CE}}) & \dots & Y_1(k,m+(N_{\text{T}}-1)N_{\text{CE}}) \\ Y_2(k,m) & Y_2(k,m+N_{\text{CE}}) & \ddots & Y_2(k,m+(N_{\text{T}}-1)N_{\text{CE}}) \\ \vdots & \ddots & Y_j(k,m+(i-1)N_{\text{CE}}) & \vdots \\ Y_{N_{\text{R}}}(k,m) & Y_{N_{\text{R}}}(k,m+N_{\text{CE}}) & \dots & Y_{N_{\text{R}}}(k,m+(N_{\text{T}}-1)N_{\text{CE}}) \end{pmatrix},$$

$$\mathbf{H}(k,m) = \begin{pmatrix} H_{11}(k,m) & H_{12}(k,m) & \dots & H_{1N_{\text{T}}}(k,m) \\ H_{21}(k,m) & H_{22}(k,m) & \ddots & H_{2N_{\text{T}}}(k,m) \\ \vdots & \ddots & H_{ji}(k,m) & \vdots \\ H_{N_{\text{R}1}}(k,m) & H_{N_{\text{R}2}}(k,m) & \dots & H_{N_{\text{R}}N_{\text{T}}}(k,m) \end{pmatrix},$$

$$\mathbf{D}(k) = \begin{pmatrix} D(k) & 0 & \dots & 0 \\ 0 & D(k) & \ddots & 0 \\ \vdots & \ddots & \ddots & \vdots \\ 0 & 0 & \dots & D(k) \end{pmatrix} \text{ and}$$

$$\mathbf{W}(k,m) = \begin{pmatrix} W_1(k,m) & W_1(k,m+N_{\text{CE}}) & \dots & W_1(k,m+(N_{\text{T}}-1)N_{\text{CE}}) \\ W_2(k,m) & W_2(k,m+N_{\text{CE}}) & \ddots & W_2(k,m+(N_{\text{T}}-1)N_{\text{CE}}) \\ \vdots & \ddots & W_j(k,m+(i-1)N_{\text{CE}}) & \vdots \\ W_{N_{\text{R}}}(k,m) & W_{N_{\text{R}}}(k,m+N_{\text{CE}}) & \dots & W_{N_{\text{R}}}(k,m+(N_{\text{T}}-1)N_{\text{CE}}) \end{pmatrix}.$$

The N_{T} columns of matrix $\mathbf{Y}(k,m)$ are composed of the N_{R} received training symbols that are N_{CE} apart as imposed by the time-orthogonal MIMO preamble design. Note that due to the periodicity of the hopping-pattern (TFC) and the assumption of a *quasi-static* MIMO-UWB channel during the transmission of a single frame, the relation $H_{ji}(k,m) = H_{ji}(k,m+N_{\text{CE}})$ holds. We can thus completely describe the time-frequency hopping behaviour of the system by estimating the MIMO channel matrix across the number of CE symbols N_{CE} within the preamble. The mapping of the CE symbol index m to the sub-band index l (Band-ID) is straightforward and depends only on the current TFC and Band-ID vector with elements $\{l_m\}$, see for example Table 4.8.

Due to the diagonal structure of the CE sequence matrix $\mathbf{D}(k)$, the Least-Squares Estimate (LSE) of the MIMO channel matrix requires only an element-wise multiplication of the received training matrix $\mathbf{Y}(k,m)$ with the conjugate value of the known CE symbol of unit power ($\|D(k)\|^2 = 1$), i.e.

$$\hat{\mathbf{H}}_{\text{LSE}}^l(k,m) = \mathbf{Y}(k,m)\mathbf{D}^{-1}(k) = \mathbf{Y}(k,m) \frac{D^*(k)}{\|D(k)\|^2} = \mathbf{Y}(k,m)D^*(k). \quad (4.11)$$

The accuracy of the LS channel estimation can be improved by repetition of the training symbols at the transmitter and subsequent averaging over the corresponding received symbols. Since the

number of CE symbols ($N_{\text{CE}} = 6$) is twice the maximum number of sub-bands within a Band Group, it is possible to average the channel estimate across at least two symbols as

$$\hat{\mathbf{H}}_{\text{av,LSE}}^{l_m}(k,m) = \frac{1}{O(L)} \sum_{\substack{l_\mu \in L \\ l_\mu = l_m}} \mathbf{H}_{\text{LSE}}^{l_\mu}(k,m), \quad (4.12)$$

where the set L contains all the sub-band indices $\{l_\mu\}$ matching the current symbol m for a given TFC such that $l_\mu = l_m$.

Alternatively, a straightforward extension of (4.11) to an MMSE-based channel estimate can be applied as

$$\hat{\mathbf{H}}_{\text{MMSE}}^{l_m}(k,m) = \mathbf{Y}(k,m) \frac{D^*(k)}{\|D(k)\|^2 + \sigma_n} = \mathbf{Y}(k,m) \frac{D^*(k)}{1 + \sigma_n}, \quad (4.13)$$

where σ_n^2 is the estimate of the noise power averaged over the number of receive antennas. However, the performance of both LSE and MMSE-based CE schemes is highly dependent on the SNR (and the quality of its estimation). Error propagation in the channel estimates and the subsequent MIMO combining can be further alleviated through phase tracking using the pilot subcarriers within the data payload.

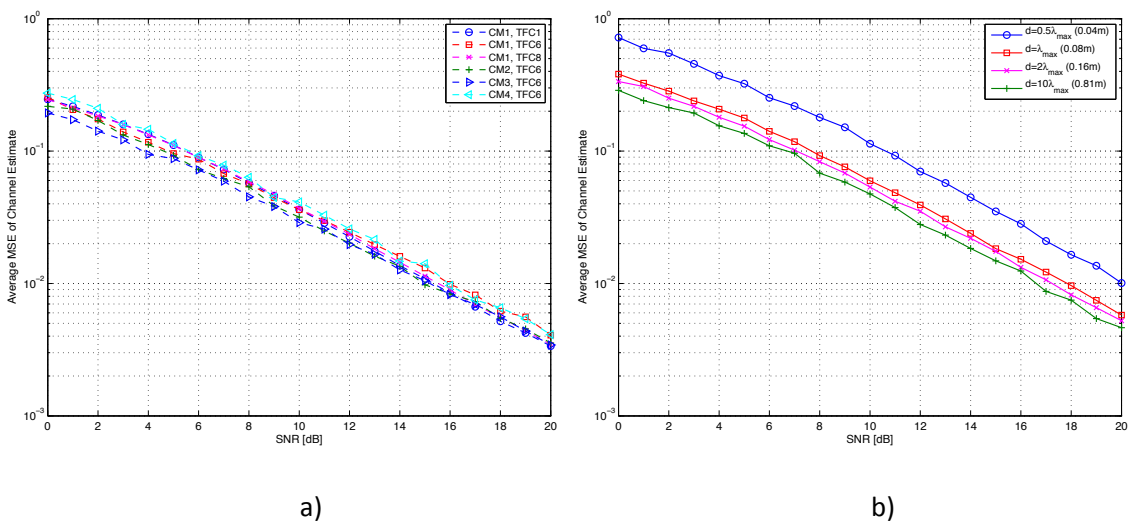


Figure 4.16: Average MSE of channel estimation for a) SISO in CM1-4 with different TFCs, and b) 3×4 MIMO with different antenna spacing in CM1 with TFC6.

Figure 4.16 shows the average mean squared error (MSE) of LS channel estimation for different TFCs and antenna configurations. Comparing the CE performance of fixed- and hopping systems in CM1 to CM4, we notice only negligible degradation as the channel becomes more dispersive and the number of multipaths increases. In Figure 4.16b), the effect of spatial correlation on the channel estimates is

demonstrated in CM1 for different antenna spacing. Due to the time-orthogonal preamble design, each additional TX antenna degrades the quality of the LS estimates only marginally as the received SNR during channel estimation is equivalent to that of SISO case. However, while the antenna elements become more closely separated, the correlation among the spatial paths increases, amounting in up to 3 dB degradation as compared to the nearly uncorrelated case of $d = 10\lambda_{\max}$.

4.2.4 Modelling, Impact and Compensation of Impairments

Although OFDM-based systems prove to be effective in combating the multipath fading, they are very vulnerable to impairments in the analog front-ends of both TX and RX that distort the orthogonality of the sub-carriers and thus limit the overall performance of the system. Among these are mainly imperfections of the local oscillators and up-/down-conversion circuit – phase noise (PN), DC-offsets, I/Q imbalance – as well as non-linearities of the power amplifiers at the TX.

4.2.4.1 Phase Noise

Due to thermal noise, any RF oscillator exhibits deviations from its ideal delta-function-like PSD around the desired center frequency. While the disturbances in mean amplitude of the LO output are negligible, the random deviations in the excess phase, referred to as PN, proves to be a major problem in systems with low implementation costs and very high center frequencies [33]. According to the two-step modelling approach in [34], the influence of PN on the received baseband signal itself corresponds to a deterministic phase rotation $e^{j\varphi}$ common to all sub-carriers of a given symbol, and to a combined Inter-Carrier Interference (ICI) contribution of all other tones on sub-carrier k , as modelled by the parameter $\Psi(k)$. In order to distinguish between TX and RX front-end impairments ($\Psi_T(k)$ and $\Psi_R(k)$), these are typically modelled separately and irrespective of the symbol index m and sub-band index l , leading to

$$\check{Y}(k) = \left(e^{j\varphi_T} + e^{j\varphi_R} \right) H_{\text{eff}}(k) \left(D(k) + \Psi_T(k) \right) + \Psi_R(k) + W(k). \quad (4.14)$$

Figure 4.17 illustrates the effects of PN on the received QPSK constellation points at the output of the FFT for ideal noiseless transmission. It can be noted that the impaired signal on a sub-carrier $\check{Y}(k)$ is rotated by a common phase shift φ from its reference tone $Y(k)$ within an additive noise cloud $\Psi(k)$.

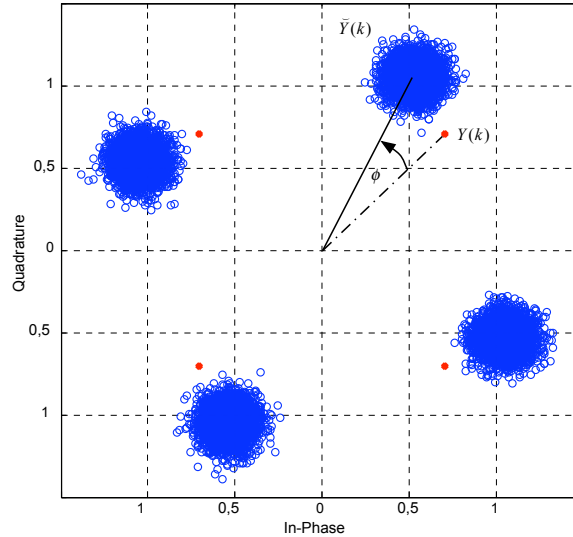


Figure 4.17: Effect of phase noise on the received QPSK constellation.

Since designing a stable oscillator especially in low-cost systems is quite challenging, most techniques for the compensation of PN effects concentrate on the use of digital signal processing in the RX baseband. The approaches presented in literature can be sub-divided into two main categories – one based on data-aided estimation, and the other depending on already detected data symbols [35]. The former technique exploits known pilot sub-carriers, which are evenly inserted among user data tones to avoid that all pilots fall in the same channel fade. The phase rotation of these pilots is common for all sub-carriers of a given symbol and is therefore a good measure of the Common Phase Error (CPE) caused by PN. For a given set P of pilot sub-carriers within a MB-OFDM symbol, this rotation is given by

$$\tilde{\varphi} = \angle \left(\sum_{k \in P} \tilde{P}(k) P^*(k) \right) \quad (4.15)$$

where $\tilde{P}(k)$ are the estimates, before slicing to the nearest constellation point, of the actually transmitted pilot sub-carriers $P(k)$. It should be noted that the value of $\tilde{\varphi}$ is in general different for each received symbol and sub-band of transmission, and includes the phase rotation on both TX and RX side. A simple technique to compensate for this common phase shift is to multiply the complex valued sub-carriers of the corresponding symbol with the complex factor $e^{-j\tilde{\varphi}}$. Since in the proposed MIMO VHDR MB-OFDM system the TX/RX architectures share a common oscillator, the estimation of the CPE can be performed for all antenna branches, right after the MIMO equalization. While this common estimation implies reduced complexity of the RX, it is sensitive to errors in the estimates of the received pilots, which could degrade the quality of CPE compensation. The correction of this rotational effect however should be done separately for each antenna RX antenna branch during the phase tracking phase.

4.2.4.2 I/Q Imbalance

Another drawback of the deployed Zero-IF RX architecture and its down-conversion circuit is the possible mismatch between the amplitudes of the In-phase (I) and Quadrature (Q) signal paths, known as I/Q imbalance. Due to limited accuracy in the implementation of the RX front-end and imperfect shifting of the LO output by 90° , these gain and phase errors limit the inherent image rejection and deteriorate the receiver performance. Figure 4.18 illustrates the influence of I/Q mismatch for two sub-carriers ($-k$ and k) of the received RF (upper), and received baseband (lower) OFDM signal.

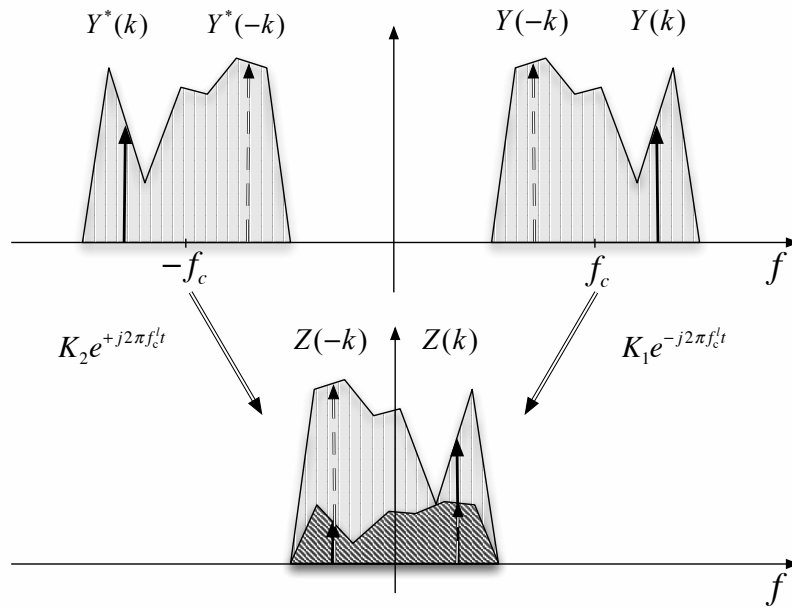


Figure 4.18: Influence of I/Q imbalance on the received sub-carriers of the: up) RF signal, and down) baseband OFDM signal.

Due to the frequency selective fading channel, the tones of the received RF signal are attenuated to a different extent, e.g. tone k has deeper fade than tone $-k$. In case the proposed MIMO Zero-IF receiver structure exhibits I/Q imbalance, the image will not be fully rejected and will thus distort the desired baseband signal. This is illustrated in the lower part of the figure, where tone k experiences a leakage from its mirror tone $-k$, and vice versa. It can further be shown that the effects of I/Q imbalance on the signal constellation are characterized by an additive rotation and decrease of amplitude [36], [37].

In the proposed MIMO MB-OFDM system, the I/Q Imbalance and CFO at the RX down-conversion circuit have been modelled for a single RX antenna branch, as shown in Figure 4.19. Here, the output of the LO

$$\tilde{z}_{\text{LO}}(t) = \cos(2\pi f_c^l t + c(t)) - jg_{\text{R}} \sin(2\pi f_c^l t + c(t) + \phi_{\text{R}}) = K_1 e^{-j(2\pi f_c^l t + c(t))} + K_2 e^{j(2\pi f_c^l t + c(t))}, \quad (4.16)$$

is distorted by an amplitude gain g_R , phase mismatch ϕ_R and phase offset due to CFO $c(t) = c_0 + 2\pi(f_{LO} - f_c^l)t$. The factors $K_1 = (1 + g_R e^{-j\phi_R})/2$ and $K_2 = (1 - g_R e^{j\phi_R})/2$ model the I/Q imbalance. After low-pass filtering the received analog baseband signal can be written as

$$z(t) = \text{LP}\{y(t)\tilde{z}_{LO}(t)\} = K_1 y(t)e^{-jc(t)} + K_2 y^*(t)e^{jc(t)}, \quad (4.17)$$

where the RX antenna index q has been omitted. Figure 4.20 depicts the influence of I/Q mismatch ($g_R = 85\%$ and $\phi_R = 5^\circ$) on the received DCM constellation points for an ideal noiseless channel. It can be concluded that an I/Q mismatch distorts the signal by an additive constellation of lower amplitude and a rotation common to all sub-carriers. This is caused by the leakage of the mirror carrier $-k$, where the rotation and reduced amplitude are due to the imbalance parameter K_2 . On the other hand, the minor rotation and decrease in amplitude of the whole constellation result from the multiplication of the desired signal (on subcarrier k) with the imbalance factor K_1 .

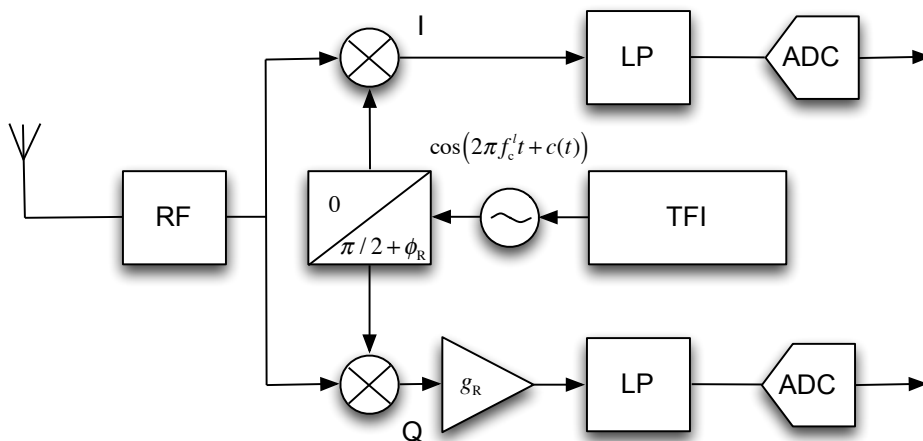


Figure 4.19: I/Q imbalance at a single RX antenna branch

One approach to circumvent these distortions of the I- and Q signal paths is to use a more accurate mixer structure, which would increase the implementation cost of the RX. Alternative techniques rely therefore on I/Q imbalance compensation in the digital baseband, based either on data-aided or *blind* parameter estimation [36].

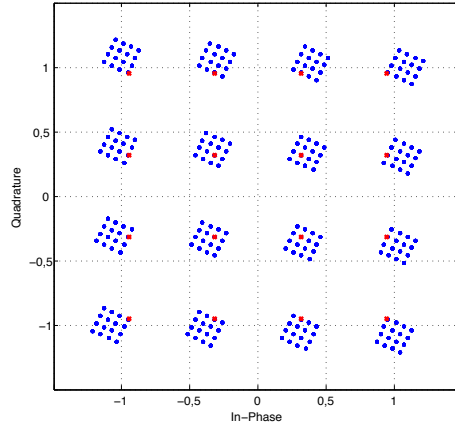


Figure 4.20: Impact of I/Q imbalance on the received DCM constellation.

The latter indicates that the estimation of K_1 and K_2 is based only on the received corrupted sub-carriers. While the symbols used for estimation are unknown to the RX, this method is still reference-based, as it requires a pre-defined preamble such that a robust I/Q estimation is possible even in noisy, frequency selective environment. Neglecting for the moment the influence of CFO, the corrupted baseband signal $z(t)$ can be expressed on a sub-carrier level at the output of the FFT as

$$\begin{pmatrix} Z(k) \\ Z^*(-k) \end{pmatrix} = \begin{pmatrix} K_1 & K_2 \\ K_2^* & K_1^* \end{pmatrix} \begin{pmatrix} Y(k) \\ Y^*(-k) \end{pmatrix} = \mathbf{K} \begin{pmatrix} Y(k) \\ Y^*(-k) \end{pmatrix}, \quad (4.18)$$

where the imbalance matrix \mathbf{K} is always invertible for realistic imbalance parameters.

According to [36], the blind estimation of I/Q imbalance can be performed in two steps: estimation of the product $K_1 K_2$, followed by the derivation of the inverse parameter matrix \mathbf{K}^{-1} . The first one is found by averaging over multiple pairs of uncorrelated sub-carriers, preferably over time:

$$\hat{K}_1 \hat{K}_2 = \frac{\mathbb{E}\{Z(k)Z(-k)\}}{\mathbb{E}\{|Z(k) + Z^*(-k)|^2\}} \quad (4.19)$$

In reverse order, the imbalance gain and phase error are then estimated as

$$\hat{g}_R = \sqrt{1 - 4\Re\{\hat{K}_1 \hat{K}_2\}} \quad \text{and} \quad \hat{\phi}_R = \arcsin\left(-\frac{2}{\hat{g}_R} \Im\{\hat{K}_1 \hat{K}_2\}\right) \quad (4.20)$$

The inverse compensation matrix $\hat{\mathbf{K}}^{-1}$ is now easily found with $\hat{K}_1 = (1 + \hat{g}_R e^{-j\hat{\phi}_R})/2$ and $\hat{K}_2 = (1 - \hat{g}_R e^{j\hat{\phi}_R})/2$ as

$$\hat{\mathbf{K}}^{-1} = \frac{1}{|\hat{K}_1|^2 - |\hat{K}_2|^2} \begin{pmatrix} \hat{K}_1^* & -\hat{K}_2 \\ -\hat{K}_2^* & \hat{K}_1 \end{pmatrix}, \quad (4.21)$$

and can be applied to compensate the corrupted sub-carriers:

$$\begin{pmatrix} \hat{Y}(k) \\ \hat{Y}^*(-k) \end{pmatrix} = \hat{\mathbf{K}}^{-1} \begin{pmatrix} Z(k) \\ Z^*(-k) \end{pmatrix} = \hat{\mathbf{K}}^{-1} \mathbf{K} \begin{pmatrix} Y(k) \\ Y^*(-k) \end{pmatrix}. \quad (4.22)$$

The block diagram of I/Q imbalance estimation and compensation per antenna branch is depicted in Figure 4.21.

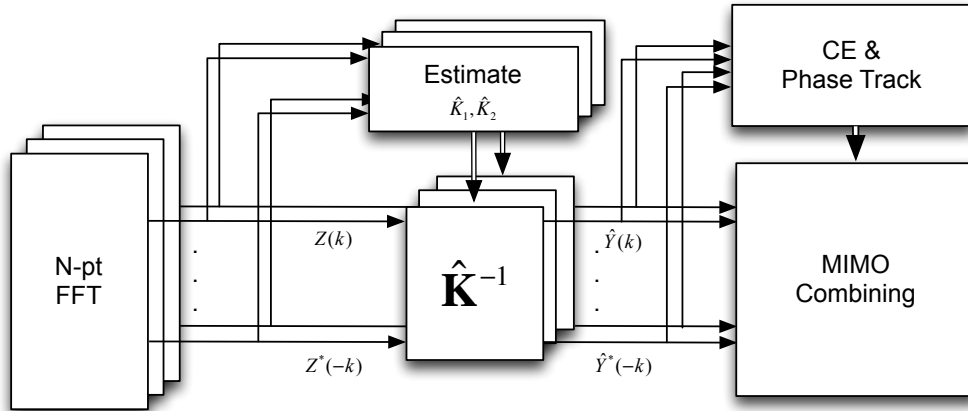


Figure 4.21: I/Q imbalance estimation and compensation per antenna branch.

Although the TX/RX architectures of the described MIMO MB-OFDM system share a common oscillator (thus exhibit common phase error), the estimation of the I/Q imbalance should be performed for each antenna branch separately, right after the FFT operation. This is imposed by the fact that the antenna branches may have different gain mismatches, which would call for different I/Q mismatch estimation parameters $K_1 K_2$ and therefore increased complexity of the compensation.

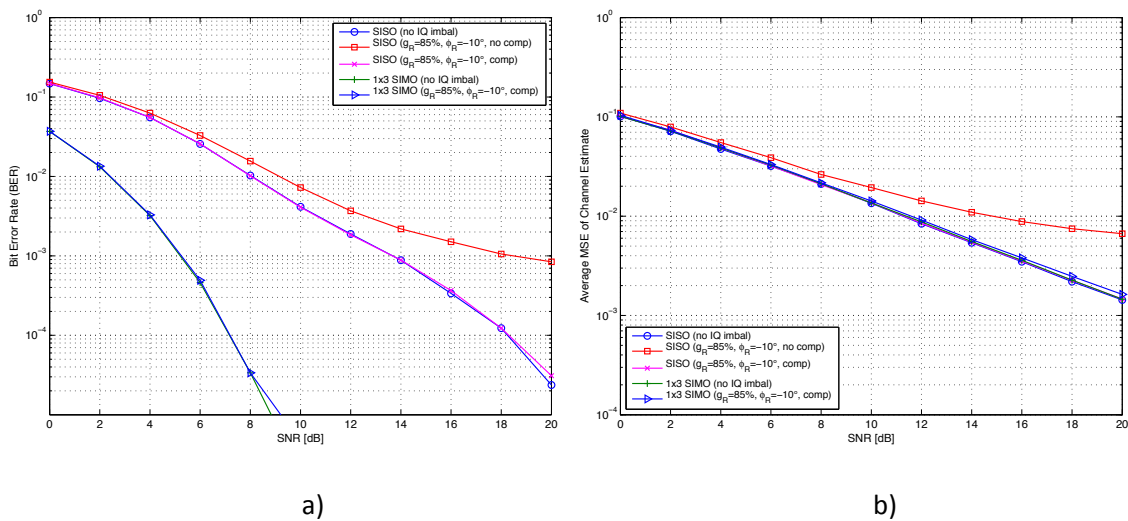


Figure 4.22: Effect of I/Q imbalance on the a) uncoded BER performance, and b) average MSE of channel estimation of 480 Mbps MB-OFDM (1m LOS, TFC8).

As shown in Figure 4.22, an I/Q imbalance at the RX down-conversion with amplitude mismatch of 85% and phase distortion of -10° leads to almost 2 dB degradation in the measured BER performance of the 480 Mbps mode in 1m LOS environment. This effect is mostly compensated for both SISO and SIMO transmissions, with marginal deviation from the ideal case of no I/Q imbalance.

We next describe a closed-loop approach for the estimation of CFO based on the auto-correlation function (ACF) metric of two adjacent symbols.

4.2.4.3 Carrier Frequency Offset

As mentioned above, the difference between the oscillating frequencies of the transmitter and receiver is defined as the CFO Δf_l , which regardless of a shared LO among the antennas may vary for each sub-band l . The estimation and compensation of CFO has therefore to be performed independently per sub-band, but can be shared among the RX antenna branches. As any frequency offset translates to a CPE and irreversible ICI among the sub-carriers of an OFDM signal, the coarse CFO estimation is crucial for the quality of the post-FFT equalization and shall be completed prior to channel estimation and payload demodulation.

Figure 4.23 depicts the structure of an iterative CFO estimator based on the ACF metric of two adjacent (on the same sub-band l) preamble symbols [30]

$$A_l(d) = \sum_{n=0}^{N-1} r_l^*(d+n)r_l(d+n+p_l N_s) \quad (4.23)$$

where $r_l(n)$ is the received preamble symbol on sub-band l and p_l is the distance between two adjacent symbols in terms of the symbol length N_s .

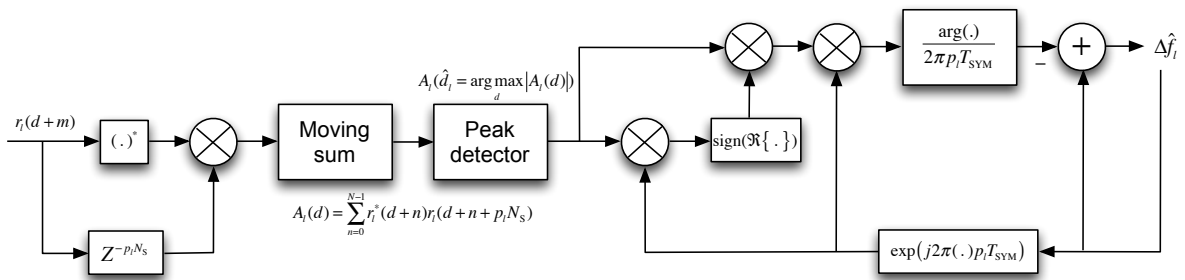


Figure 4.23: Block diagram of an iterative CFO estimator

The initial value of the CFO is calculated from the phase estimate of the ACF close to its maximum

$$\angle \left(A_l \left(\hat{d}_l = \operatorname{argmax}_d |A_l(d)| \right) \right)$$

and further refined by subtracting the residual error of the previous CFO estimates.

Due to the changes in the polarity of the PS symbols during preamble transmission, the CFO estimation may become ambiguous and unstable if the frame is not yet synchronized. In particular, the value of the ACF at its maximum changes polarity depending on the current pair of correlated symbols, yielding sign-inverted estimates of the CFO. To avoid this ambiguity and error propagation in the CFO estimates, we multiply the peak value of the ACF by the sign of real part of its phase-shifted counterpart.

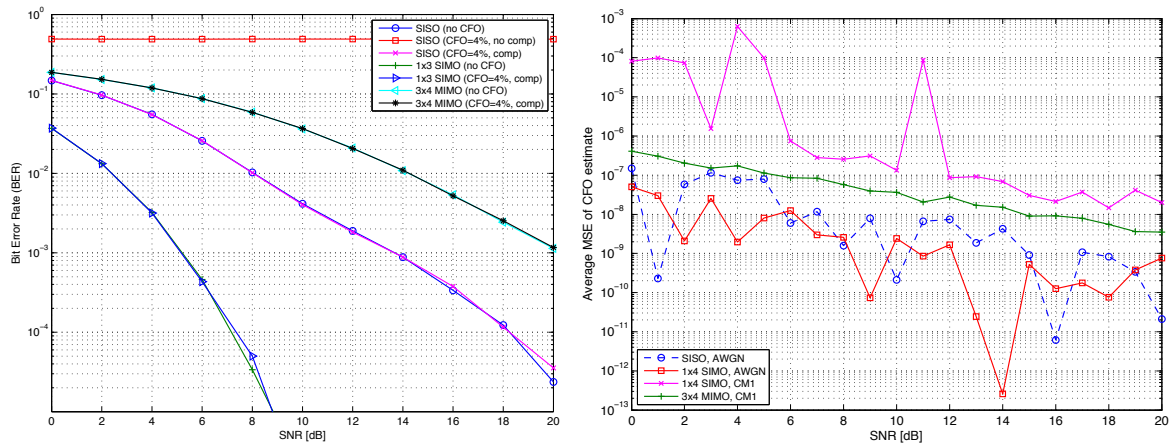


Figure 4.24: Performance of CFO estimation and compensation in terms of the a) measured uncoded BER for QPSK in 1m LOS, and b) normalized average MSE of CFO estimation in AWGN and CM1 for CFO=4%.

Once the frame has been synchronized and a coarse estimate of the CFO has been acquired, the data symbols are multiplied by the complex term $e^{j2\pi n\hat{\Delta}_l^c T_s}$, where $\hat{\Delta}_l^c$ stands for the coarse estimate of the CFO for a given sub-band l . In Figure 4.24a), we compare the uncoded BER performance of SISO, SIMO and MIMO MB-OFDM after CFO compensation for QPSK modulation in measured 1m LOS environment. For all antenna configurations, the average performance degradation remains marginal, with 3×4 MIMO outperforming both SISO and SIMO due to increased diversity present in the system. Figure 4.24b) further depicts the performance of the proposed CFO estimator in terms of normalized mean squared error (MSE) of the CFO estimate in AWGN and frequency selective CM1, with normalized CFO equal to 4% of the sub-carrier spacing. The estimator exhibits stable performance for both frequency flat and selective fading, whereas the fluctuations in the normalized errors for the 3×4 MIMO case over 90% of best 100 CM1 realizations are minimized at most due to the induced receive diversity and thus reduced uncertainty of the estimation.

4.3 Conclusions

This chapter has presented the general concept of a modular system design of a flexible MIMO MB-OFDM simulator combined with an experimental offline test-bed and hardware-in-the-loop FPGA platform. This approach provides direct access to the wireless channel as well as solid reference for

real-time implementation of selected MIMO algorithms, which allows for impact analysis and evaluation of HW-specific resource consumption of selected MIMO schemes.

Furthermore, we have defined extensions to the parameter set and frame format of the current ECMA-368 standard to enable VHDR by doubling the system bandwidth. System design aspects such as link budget and optimal parameter selection have been considered. Finally, algorithms for robust synchronization in time and frequency, as well as for the estimation and compensation of RF frontend imperfections have been investigated, developed and verified under real measurement constraints.

Chapter 5

Advanced Deployment Schemes for MIMO MB-OFDM

As described in Chapter 3, the use of multiple antennas can provide substantial gains in terms of improved performance, capacity and/or coverage of the system. The linear increase in spectral efficiency in SMUX systems however comes at the expense of higher power consumption and more complex signal processing, even in the case of trivial linear decoders. It is well known that in terms of complexity the most challenging part of a spatially multiplexed system is the MIMO decoder at the RX. The major challenge to MIMO implementation is therefore the design of efficient low-complexity receiver algorithms and corresponding architectures that meet the harsh latency and power consumption requirements of upcoming UWB applications [23].

In general, MIMO detection schemes can be subdivided in two categories with respect to the applied strategy: maximum likelihood (ML-) nonlinear methods based on exhaustive search over all possible candidate symbols, and non-ML algorithms which lead to sub-optimal performance yet having reduced computational complexity. Among the latter are zero forcing (ZF-) and minimum mean square error (MMSE-) based linear detectors, as well as successive interference cancellation (SIC) receivers and iterative tree search methods like K-best and sphere decoding (SD) with early termination [38]. Depending on the application requirements, a fundamental trade-off has to be found between the improved capacity offered by the use of multiple antennas and the induced higher complexity of signal processing. In terms of performance, sub-optimal linear receivers and SIC schemes are preferred in spatially multiplexed systems with higher modulation orders and number of antennas, whereas near-ML tree search algorithms become suitable for lower throughput modes at comparable complexity.

To verify the performance of the proposed MIMO-UWB system deploying spatial multiplexing, we first describe a low-complexity MMSE linear detection algorithm based on QR-decomposition (QRD) of the extended channel matrix. Further, we propose two computationally efficient schemes for V-BLAST architectures, based on successive interference cancellation with MMSE-based sorted QR-decomposition (MMSE-SQRD). Finally, we propose an efficient differential algorithm for FFT-based spectrum sensing and interference detection as well as simple DAA schemes to improve the co-existence behaviour of the system.

5.1 Deployment Scenarios and Performance Requirements

In Figure 5.1, we point out the envisioned deployment scenarios and briefly comment on the appropriate MIMO schemes and potential gains that can help meet the performance requirements of these applications.

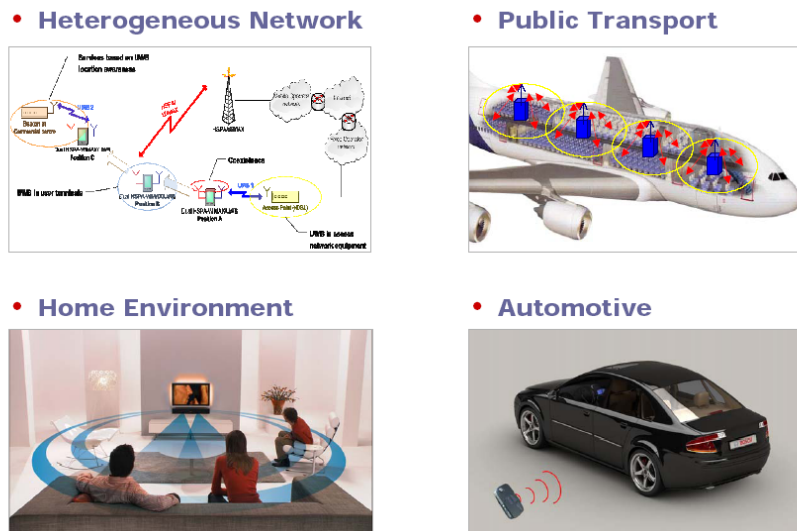


Figure 5.1: Deployment scenarios of the FP7 IP EUWB [39][40].

EHDR in Home Entertainment

- multiband/multimode (VHDR UWB and Dual Mode transmission) wireless streaming of uncompressed high definition video content in a Home Theatre System. Here, multiple independent antenna branches can linearly improve the spectral efficiency of the system in order to reach data rates exceeding 2 Gbps
- cable replacement between the an ambisound system and the surrounding audio boxes.

Multi-user Support in Public Transportation

- wireless cabin management system (CMS) – aim is to enable wireless connectivity for fixed installed or mobile devices within the cabin. Here, MIMO diversity schemes like STFC or Dual Mode can provide improved coverage, robustness to interference and link redundancy. SDMA techniques can further offer better power efficiency of the access points and reduced multi-user or inter-cell interference
- passenger communication and in-flight entertainment (IFE) – spatial multiplexing schemes can help meet the high demands on data distribution capacity by supporting high-speed multiple A/V streams and multi-user enhancements
- mobile maintenance terminals – beamforming with multiple antennas can support extended functions for the crew, by e.g. improved localization or interference suppression.

Enhanced Robustness in Automotive Environment

- localization of dedicated tag inside and outside a car with different number of antennas to improve the coverage and quality of detection
- intrusion sensing - invasion alarm, children/dog protection, marten detection, luggage space sensor
- occupancy sensing - activating of seat belt pretension
- wireless data communication - remote connection of UI elements to dashboard, sensor to electronic control unit, CAN bus replacement.

In the following, we describe in detail the advanced MIMO schemes, which are capable of meeting the above-mentioned requirements and of exploiting the various performance and capacity gains provided by MIMO.

5.2 Linear MMSE Receiver with QR-Decomposition

Starting with the MIMO system model in Eq. (3.2), linear detection schemes try to solve the input-output relation with respect to the least-squares (e.g. ZF receiver) or MMSE criterion to detect the transmitted symbols \mathbf{S} . While ZF aims to perfectly separate the data streams by trying to directly revert the effect of the channel and force the interference streams to zero, it is known to suffer from noise enhancement. The MMSE equalizer matrix \mathbf{G}_{MMSE} on the other hand takes the noise into consideration by trying to minimize the post-processing error $E\{(\mathbf{S} - \mathbf{G}\mathbf{Y})^2\}$. The Wiener solution for \mathbf{G}_{MMSE} is known as

$$\mathbf{G}_{\text{MMSE}} = \left(\mathbf{H}^H \mathbf{H} + \frac{1}{\rho} \mathbf{I}_{N_T} \right)^{-1} \mathbf{H}^H, \quad (5.1)$$

where $\rho = \sigma_s^2 / (N_T \sigma_n^2)$ stands for the SNR at the RX, σ_s^2 and σ_n^2 are the signal- and noise power respectively, and \mathbf{I}_{N_T} denotes an $N_T \times N_T$ identity matrix.

One computationally efficient scheme to revert the channel effect is QRD which decomposes the channel \mathbf{H} into a unitary matrix \mathbf{Q} and an upper-triangular matrix \mathbf{R} . To perform QR decomposition with respect to the MMSE criterion, the channel matrix \mathbf{H} and received vector \mathbf{Y} are extended as

$$\tilde{\mathbf{H}} = \begin{pmatrix} \mathbf{H} \\ \sqrt{N_T} \sigma_n \mathbf{I}_{N_T} \end{pmatrix} = \tilde{\mathbf{Q}} \tilde{\mathbf{R}} = \begin{pmatrix} \mathbf{Q}_1 \\ \mathbf{Q}_2 \end{pmatrix} \tilde{\mathbf{R}} = \begin{pmatrix} \mathbf{Q}_1 \tilde{\mathbf{R}} \\ \mathbf{Q}_2 \tilde{\mathbf{R}} \end{pmatrix} \quad \text{and} \quad \tilde{\mathbf{Y}} = \begin{pmatrix} \mathbf{Y} \\ 0 \end{pmatrix}, \quad (5.2)$$

where \mathbf{Q}_1 and \mathbf{Q}_2 are both unitary matrices [41], [67]-[68]. The equivalent square-root formulation of the MMSE-based solution thus allows for efficient calculation of the equalizer matrix

$$\mathbf{G}_{\text{MMSE}} = \frac{\mathbf{Q}_2 \mathbf{Q}_1^H}{\sqrt{N_T \sigma_n}}, \quad (5.3)$$

as well as matrix-vector multiplication without the need of any matrix inversion.

In the following, we demonstrate the performance of the proposed linear MMSE receiver based on QRD in both simulated and measured propagation environments.

A direct comparison of the measured uncoded vs. coded BER performance of VHDR MIMO MB-OFDM with QR-based MMSE receiver is shown in Figure 5.2, in which the number of TX/RX antenna elements is varied in 1m LOS environment. Starting with the worst case of a symmetric 2×2 MIMO system, the uncoded system is unable to achieve reliably low error rates as the strong LOS component in such a short range becomes dominant, leading to a bad-conditioned channel matrix of lower rank. Furthermore, the reliability of the noise power estimates diminishes and thus degrades the quality of MMSE QR decomposition. An immediate enhancement of the system performance is obtained by deploying additional RX antennas, which not only introduce an intrinsic array gain, but also increase the degree of freedom in estimating the noise power component and in determining the equalizer matrix \mathbf{G}_{MMSE} . Because of the frequency selective nature of the UWB channel, coding across the frequency tones becomes inevitable in order to combat deep fades in the propagation path. For OFDM based systems, this task is perfectly achieved by applying channel coding and interleaving to the input binary stream, thus ensuring that strongly attenuated or zeroed signal components can still be recovered at the RX. Moreover, as channel coding takes part before the actual OFDM modulation, i.e. in the frequency domain, the information redundancy added directly translates to extra frequency diversity of the system. This fact is visible in Figure 5.2b), where not only a typical coding gain, but also a significant improvement of the slope of the BER curves is achieved.

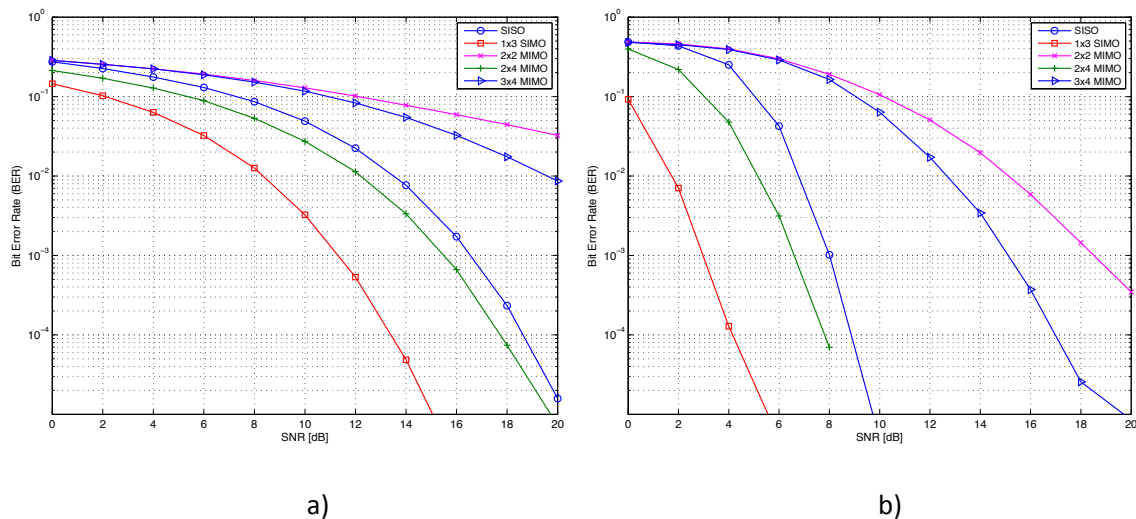


Figure 5.2: Measured BER performance of VHDR MB-OFDM with 16-QAM for different MIMO configurations and a) uncoded, and b) $R_c = 1/2$ coded transmission in 1m LOS.

Next, we illustrate the effect of spatial correlation on the coded BER performance of 3×4 MIMO MMSE for both HDR and VHDR mode, see Figure 5.3a). Conforming to results in literature, adjusting the antenna spacing to half the maximum wavelength of the MB-OFDM signal proves sufficient to drive the spatial correlation coefficient below 0.5, and close the gap to the system performance with widely separated antenna elements. The well reported performance gain of ca. 3 dB in required SNR obtained by providing soft-decision inputs to the Viterbi decoding is further verified in Figure 5.3b).

Note that in the envisioned dominant LOS measurement scenario over rather short distance of 1 m, the number of multipath components reduces to several strong paths (including the direct MPC) as the angular spreads of TX and RX arrays are relatively narrow. In fact, this may be qualified as a worst-case scenario for the deployment of MIMO, since multiple antennas are known to best benefit from highly dispersive, frequency selective channels where the spatial signatures of the diverse channel links can provide both multiplexing and diversity gains.

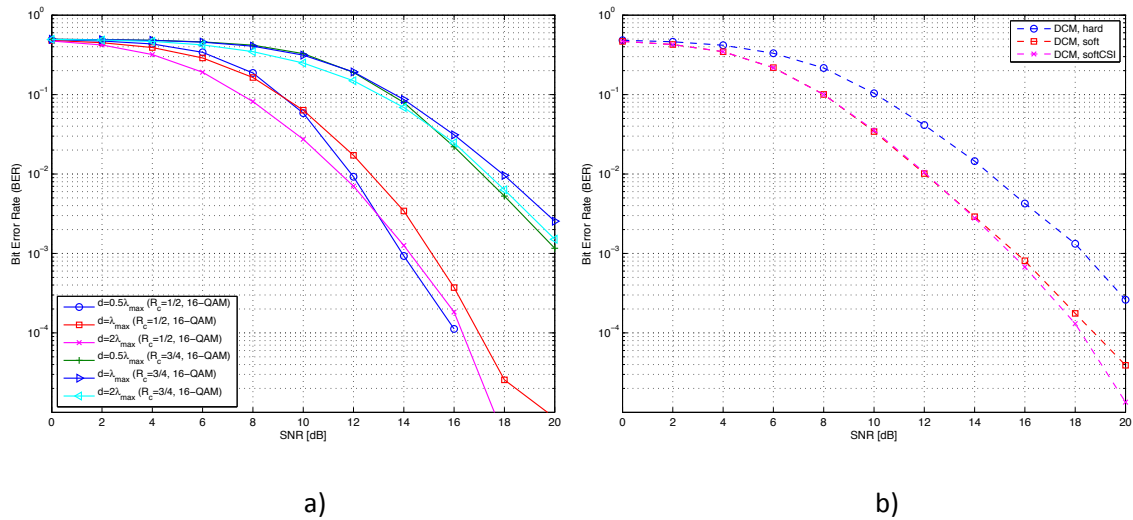


Figure 5.3: Measured performance of 3×4 MIMO (V)HDR MB-OFDM as function of the a) antenna spacing, and b) soft/hard decision metric in 1m LOS.

The proposed linear MMSE receiver can be directly applied to recover the transmitted signals during SMUX or Dual Mode operation. Figure 5.4 shows the measured BER performance of 2×2 MIMO with dual-polarized antennas as function of the vertical antenna orientation for different modulation schemes. Finally, in Figure 5.5 we demonstrate the performance gains of Dual Mode parallel transmission over Band Groups 1 and 6, in measured LOS/NLOS environment as compared to 2×2 MIMO SMUX. For both HDR and VHDR transmission, orthogonalizing the independent signal paths in either the polarisation or frequency domain can provide substantial gains in the BER performance of symmetric MIMO systems. This important result is owed to the highly minimised cross-interference of the TX-RX antenna links, which essentially diagonalizes the structure of the MIMO channel matrix and significantly alleviates its inversion at the MMSE decoder. As shown in Figure 5.4a), optimal vertical antenna orientation can improve the required SNR for a target BER by more than 9 dB as compared to common SMUX schemes using single-polarised antenna arrays. Similar improvement has been verified also for Dual Mode transmission with 2 RX antennas (see Figure 5.5) that further simplifies MIMO decoding as discussed in Section 3.2.2, since the signal paths can be bandpass filtered and processed in parallel RX branches, each featuring a single MMSE equalizer.

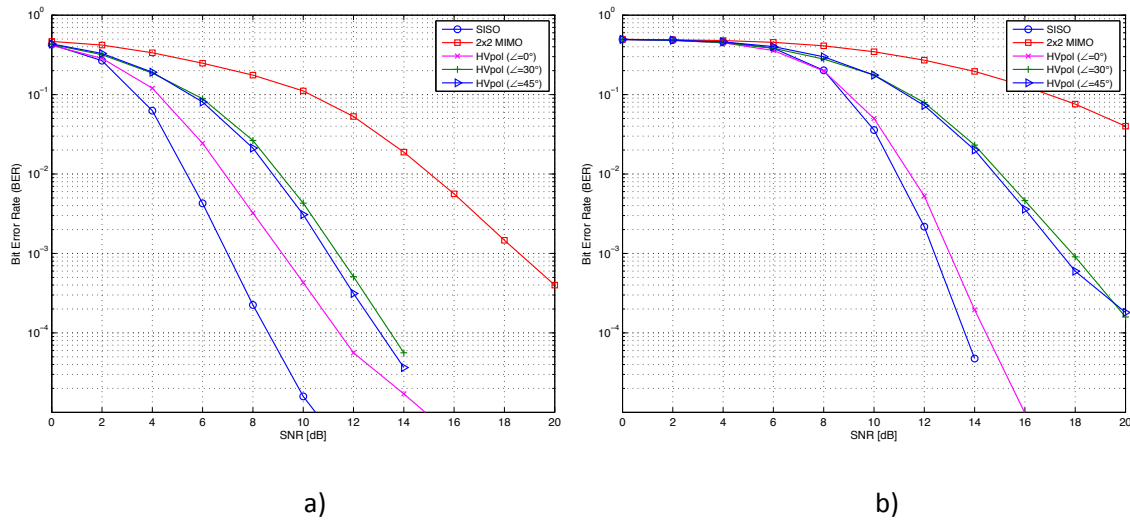


Figure 5.4: Measured BER performance of 2×2 MIMO in LOS with dual-polarized antennas as function of the vertical antenna orientation for $R_c = 3/4$ and a) DCM, and b) 16-QAM mapping.

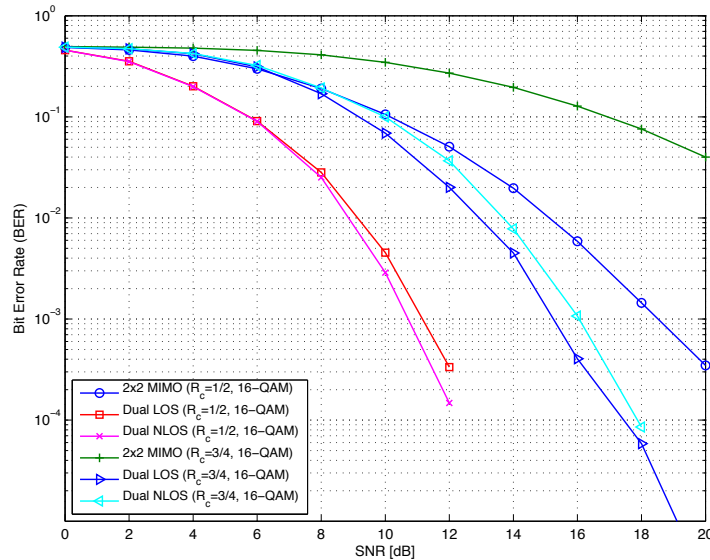


Figure 5.5: Measured BER performance of Dual Mode in LOS/NLOS for different data rates.

5.3 Ordered SIC Receiver with MMSE-based Sorted QR-Decomposition

This section describes a computationally efficient algorithm for MIMO detection in V-BLAST architectures with respect to the MMSE criterion. It utilizes a sorted QR decomposition of the estimated channel matrix before applying successive interference cancellation. Unlike linear receivers such as ZF and MMSE, the performance of a SIC receiver is strictly dominated by the stream which is detected first and therefore error propagation has considerable impact on the detection quality of the subsequent streams. An ordered SIC starts rearranging the columns of the channel matrix by attempting to identify the stream which is most likely to yield no detection errors in the first iterations. Although the ordering of the original V-BLAST algorithm in [19] is optimum with

respect to BER performance, it still requires multiple calculations of the pseudo-inverse, becoming a computationally expensive task. The sorted QR decomposition has been proposed in [41] to reduce the overall complexity to the order of linear receivers while sacrificing on 1 dB in terms of BER as compared to conventional V-BLAST schemes.

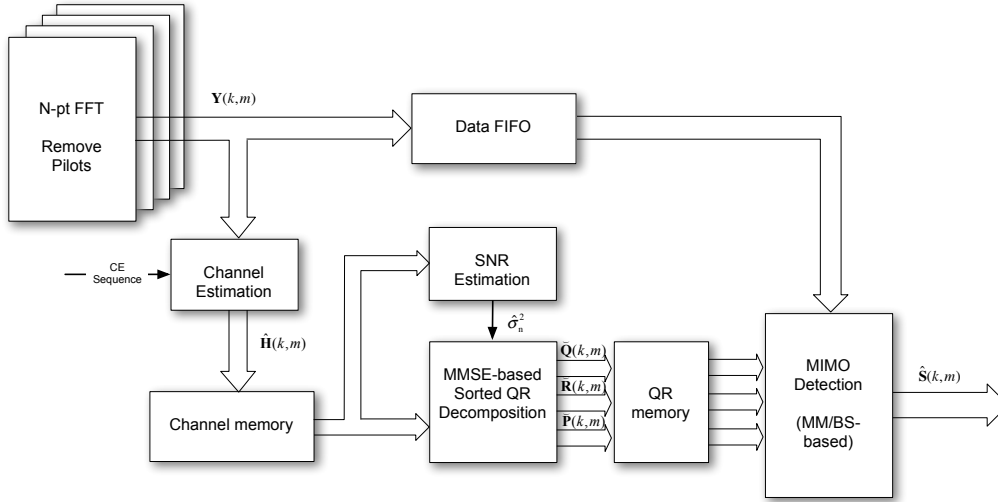


Figure 5.6: Block diagram of MIMO detection with MMSE-based Sorted QR Decomposition

Figure 5.6 shows the block diagram of a MIMO receiver with MMSE-based sorted QR-decomposition of the channel matrix. After channel estimation, a pre-processing block decomposes the MIMO channel matrices for every sub-carrier and feeds the resulting matrices to the MIMO detection block, which extracts the transmitted tones based on either matrix-multiplication (MM) in case of linear MMSE detection, or Back-Substitution (BS) for SIC receivers.

5.3.1 Sorted MMSE-based QR Decomposition

As shown in the previous section, we extend the channel matrix \mathbf{H} and the received vector \mathbf{Y} in order to perform QR decomposition with respect to the MMSE criterion as

$$\tilde{\mathbf{H}} = \begin{pmatrix} \mathbf{H} \\ \sqrt{N_T} \sigma_n \mathbf{I}_{N_T} \end{pmatrix} = \tilde{\mathbf{Q}} \tilde{\mathbf{R}} = \begin{pmatrix} \mathbf{Q}_1 \\ \mathbf{Q}_2 \end{pmatrix} \tilde{\mathbf{R}} \quad \text{and} \quad \tilde{\mathbf{Y}} = \begin{pmatrix} \mathbf{Y} \\ 0 \end{pmatrix}. \quad (5.4)$$

With the relation $\mathbf{Q}_1^H \mathbf{H} + \sqrt{N_T} \sigma_n \mathbf{Q}_2^H = \tilde{\mathbf{R}}$, the least-square solution of the extended input-output relation $\tilde{\mathbf{Y}} = \tilde{\mathbf{H}} \mathbf{S} + \tilde{\mathbf{W}}$ can be obtained by Back-Substitution (BS) from

$$\mathbf{Q}_1^H \mathbf{Y} = \tilde{\mathbf{R}} \mathbf{S} + \mathbf{Q}_1^H \mathbf{W} - \sqrt{N_T} \sigma_n \mathbf{Q}_2^H \mathbf{S}. \quad (5.5)$$

The last term in Eq. (5.5) constitutes the remaining interference that cannot be removed by successive interference cancellation [41]. The optimum detection sequence now maximizes the SINR on each layer, yielding minimum estimation error per iteration.

The most computationally expensive part of the proposed algorithm is the QR decomposition of the extended channel matrix $\check{\mathbf{H}}$. It is well known that unitary transformations based methods (e.g. Givens rotations) are more numerically stable than the Gram-Schmidt procedure. However, when one considers an FPGA based implementation, multiplication-intensive algorithms such as the modified Gram-Schmidt QR decomposition are usually more desirable than CORDIC-intensive Givens rotations [23].

The sorted version of the MMSE detection is basically an extension of the modified Gram-Schmidt procedure by reordering the columns of the channel matrix prior to each orthogonalization step. The basic idea is that the diagonal elements of the extended $N_T \times N_T$ upper triangular matrix $\check{\mathbf{R}}$ are minimized in the order in which they are computed $(1, \dots, N_T)$. Starting with the norm of the first column of $\check{\mathbf{H}}$, the first row of $\check{\mathbf{R}}$ is determined. Next, the second diagonal element and corresponding row of $\check{\mathbf{R}}$ is calculated in the same manner from the remaining $N_T - 1$ orthogonalized vectors and so forth until the extended channel matrix is transformed into an unitary ordered $(N_T + N_R) \times N_T$ matrix $\check{\mathbf{Q}}$. Note that the column norms have to be calculated only once in the beginning and can be easily updated afterwards, resulting in less computational overhead due to sorting. A description of the MMSE-based Sorted QR Decomposition (pseudo code), with $\check{\mathbf{Q}}_i$ denoting column i of $\check{\mathbf{Q}}$ and $\check{\mathbf{P}}$ a permutation matrix of the columns of $\check{\mathbf{H}}$, is given below [41]:

- (1) Initialize: $\check{\mathbf{R}} = \mathbf{O}$, $\check{\mathbf{Q}} = \check{\mathbf{H}}$, $\check{\mathbf{P}} = \mathbf{I}_{N_T}$
- (2) for $i = 1, \dots, N_T$
- (3) $\mathbf{norm}_i = \|\check{\mathbf{Q}}_i\|^2$
- (4) end
- (5) for $i = 1, \dots, N_T$
- (6) $k_i = \operatorname{argmin}_{l=i, \dots, N_T} \mathbf{norm}_l$
- (7) exchange columns i and k_i in $\check{\mathbf{R}}$, $\check{\mathbf{P}}$, \mathbf{norm}_i and in the first $N_R + i - 1$ rows of $\check{\mathbf{Q}}$
- (8) $\check{R}_{i,i} = \sqrt{\mathbf{norm}_i}$
- (9) $\check{\mathbf{Q}}_i := \check{\mathbf{Q}}_i / \check{R}_{i,i}$
- (10) for $m = i + 1, \dots, N_T$
- (11) $\check{R}_{i,m} = \check{\mathbf{Q}}_i^H \check{\mathbf{Q}}_m$
- (12) $\mathbf{norm}_m = \mathbf{norm}_m - \check{R}_{i,m}^2$
- (13) end
- (14) end

Note that the MMSE-SQRD receiver does not necessarily lead to the optimum detection sequence, but in many cases of interest the performance degradation is negligible (below 1 dB) as compared to the reduced complexity.

5.3.2 Ordered SIC Detection with Back Substitution

The Back Substitution algorithm solves linear system of equations of the form

$$\mathbf{QY} = \mathbf{RS}, \quad (5.6)$$

provided that \mathbf{R} is an upper-triangular matrix. By setting $\hat{\mathbf{Y}} = \mathbf{QY} = \mathbf{Q}_1^H \mathbf{Y}$ and $\mathbf{R} = \{R_{i,j}\} = \check{\mathbf{R}} - \sigma_n \mathbf{Q}_2^H$, the BS can be directly applied in the detection stage of the SIC detector. In order to adapt the BS-based linear detection stage to perform SIC, a slicing operation $Q(\cdot)$ is introduced to obtain the following iteration for $i = N_T, \dots, 1$:

$$(1) \quad \hat{X}_i = \hat{Y}_i / R_{i,i}$$

$$(2) \quad \hat{S}_i = Q(\hat{X}_i)$$

$$(3) \quad \hat{\mathbf{Y}}^{(i-1)} = \hat{\mathbf{Y}}^{(i)} - \mathbf{R}_i \hat{S}_i,$$

where the vectors $\hat{\mathbf{Y}}_{i-1}^{(i)}$ and \mathbf{R}_i denote the first $i-1$ entries of $\hat{\mathbf{Y}}^{(i)}$ and the corresponding entries of the i -th column of \mathbf{R} respectively. In fact, both the multiplication and division in (1) can be avoided by absorbing the corresponding normalization in the slicing operation and simply changing the decision boundaries [23].

In the following, the performance of the proposed MMSE-SQRD algorithm has been verified for a MB-OFDM system with different number of multiple antennas and modulation schemes.

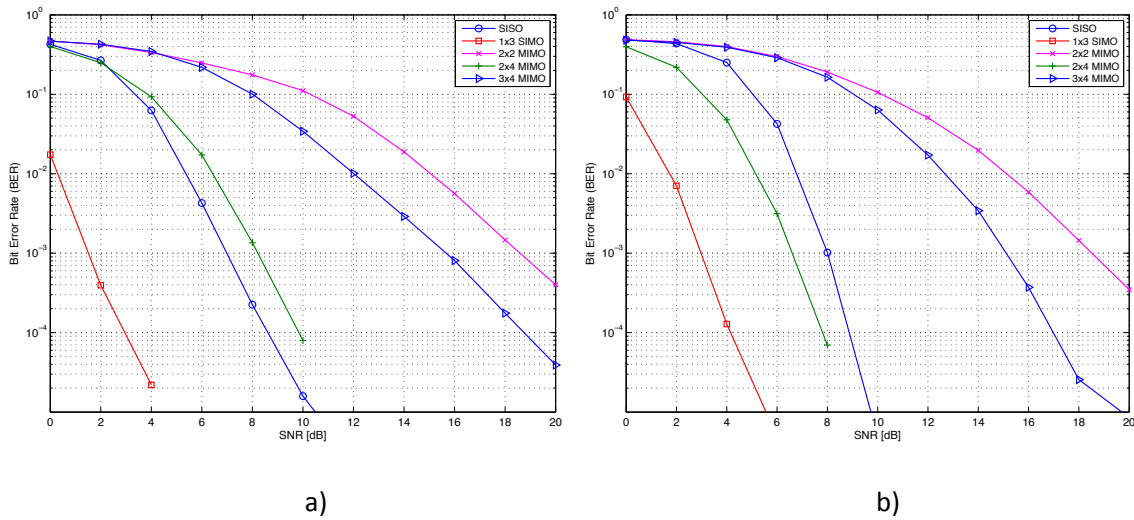


Figure 5.7: Measured BER performance of a) HDR ($R_c=3/4$, DCM, TFC8) and, b) VHDR mode ($R_c=1/2$, 16-QAM, TFC11) in 1m LOS for different antenna configurations.

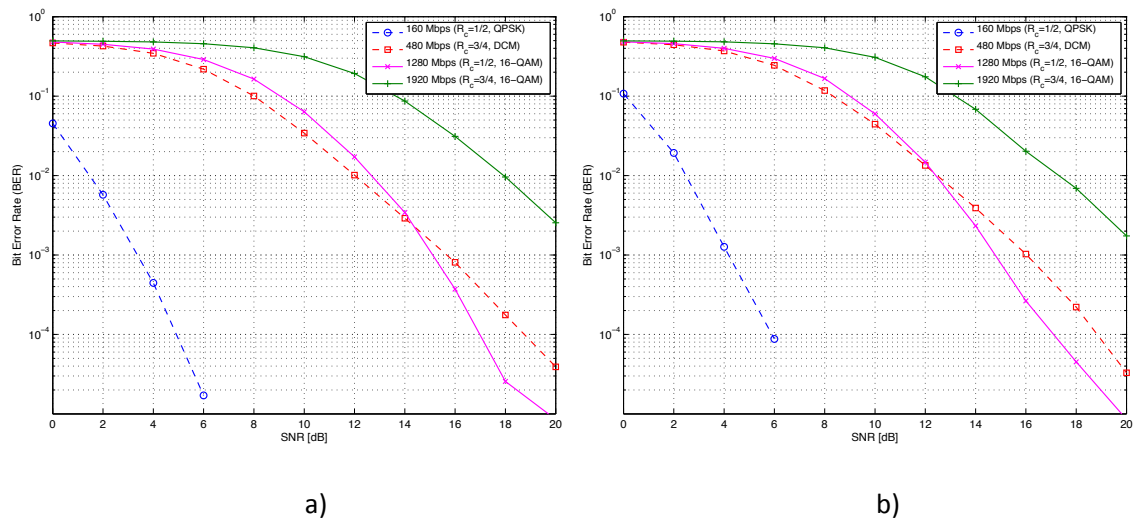


Figure 5.8: Measured BER performance of 3×4 MIMO MB-OFDM in 1m LOS for a) QRD-based MMSE, and b) O-SIC with MMSE-based SQRD receiver.

In Figure 5.7, the measured performance of different MIMO configurations and modulation schemes has been verified in 1m LOS for HDR and VHDR transmissions. Similar to the QRD-based linear MMSE RX, the O-SIC with MMSE-based SQRD is able to achieve robust BER performance at the envisioned operation point of 15 dB SNR. For bad-conditioned symmetric 2×2 MIMO channels with strong LOS component, the quality of decomposition of the channel matrix as well as of the noise power estimates highly affects the performance of the system. An attractive way to circumvent this kind of uncertainty could be the use of e.g. dual-polarised antennas or Dual Mode transmission, or, if possible, of additional antennas at the RX. The direct comparison of both MMSE-based receivers with (sorted-) QRD demonstrates their very similar performance, whereas the O-SIC outperforms the

linear MMSE RX only marginally. In fact, an optimal ordering of the columns in the decomposition matrices $\tilde{\mathbf{R}}$ and $\tilde{\mathbf{Q}}$ turns out beneficial especially for frequency selective channels. This performance gain almost vanishes when the channel coefficients become approximately equal, as is the case in strong LOS short-range scenarios.

5.4 Orthogonal STF Decoder with Scaled LLR Demodulation

Besides the constantly increasing demand for higher throughputs, the requirements for improved link robustness, reduced power consumption and extended coverage of emerging UWB devices call for efficient and low-complexity system design able to exploit possibly all degrees for communication. While spatial multiplexing schemes are not limited in the number of TX antennas and typically require simple MMSE-based linear receivers or optimized V-BLAST decoders, the minimum number of RX antennas is still bounded by the number of independent transmit streams. Recall that ML decoding becomes prohibitively complex for modulation schemes higher than QPSK and is unable to provide soft-decision reliability information to the succeeding channel decoding stage.

Diversity schemes, as introduced in Section 3.2.3, are exempted from this constraint and thus allow for MIMO transmission schemes and low-complexity receivers (such as mobile or hand-held devices) to still exploit the diversity gains offered by the spatial, time- and/or frequency dimension, and to improve the effective SNR at the input of the decoder. This concept is currently adopted by modern standards like IEEE 802.11n, WiMAX, or LTE, in which the transmitting Base Stations are equipped with multiple antennas and perform more complex diversity or beamforming algorithms in the downlink, whereas end-user devices typically deploy no more than two RX antennas in order to keep battery life long and their size/area low. Simple Alamouti- or orthogonal STF coding schemes bring the advantage of full-diversity gain and full-rate (in case of Alamouti scheme) transmission, with typically no CSI required at the TX, and of efficient *linear* ML-based combining at the RX. Prerequisite for the latter is an orthogonal (or quasi-orthogonal) structure of the diversity code, as well as constant channel characteristics for the duration of the code block. The orthogonality of the code ensures that each transmitted symbol can be decoded independently of the other transmitted symbols within the code word, thus providing viable options for deploying higher modulation schemes and parallelization at the RX.

In fact, the receiver has to possess knowledge only of at least one channel estimate per TX-RX link in order to extract the transmitted symbols. This requirement is met by the time-orthogonal preamble design and the assumption of quasi-static channel during the transmission of a frame. Further, the MIMO decoder has to be aware of the number of TX antennas (N_T) used in order to correctly estimate the channel matrix and perform MIMO detection. This information is provided by setting the corresponding TX_ANT bits in the PHY header, as shown in Section 4.1.2.1 (see Figure 4.5). Note

that since the length of the PS/FS part of the PLCP preamble remains unchanged, synchronization at the receiver can be performed without the knowledge of N_T , just before the PHY header decoding.

In the following, we provide the framework for the deployment of STFC diversity encoding and efficient combing in MIMO MB-OFDM, including some conceptual considerations on the calculation of LLR and the succeeding channel decoding. Besides the full-rate Alamouti scheme, we propose orthogonal 3/4-rate codes for three and four TX antennas based on [42] that have been applied in the time domain. This implies that at least four consecutive MB-OFDM symbols have to be transmitted over the same sub-band, i.e. the proposed schemes are applicable to FFI systems (TFC 5 to 7). Due to the frequency selective nature of the UWB channel, the encoded symbols (tones) within the code word experience different channel fading for each MB-OFDM symbol period, thus benefitting from frequency diversity. Note that for complex constellations and more than two TX antennas, rate 3/4 has been proven in [43][44] as the maximum achievable rate for orthogonal codes.

5.4.1 MIMO Coding Framework

Now we consider a MIMO MB-OFDM system equipped with 4 TX antennas and apply three alternative STF codes: the *Alamouti* code, as well as the 3/4-rate orthogonal codes for *three* and *four* active TX antennas. From Eq. (3.2), we rewrite the signal model as $\mathbf{Y} = \mathbf{H}\mathbf{S}_{K_T} + \mathbf{W}$, where \mathbf{S}_{K_T} stands for the code matrix, and the subscript K_T corresponds to the number of deployed (selected) TX antennas. The modulated data tones within an OFDM symbols are denoted by $S(k, m)$, where k is the subcarrier and m the OFDM symbol index.

It is well known that the full-rate *Alamouti* code is feasible only for two TX antennas, but arbitrary number of RX antennas. In case of more than two antennas at the TX, one may apply antenna selection according to e.g. capacity maximization criterion, and leave the remaining antennas idle depending on the availability of CSI. The symbol vector for the transmitting antenna pair during the first MB-OFDM symbol period m is constructed as $[\mathcal{S}_1 \ \mathcal{S}_2] = [S(k, m) \ S(k, m+1)]$, and the Alamouti code matrix is given as [20]

$$\mathbf{S}_2 = \begin{bmatrix} \mathcal{S}_1 & -\mathcal{S}_2^* \\ \mathcal{S}_2 & \mathcal{S}_1^* \end{bmatrix},$$

where the transmission on each TX antenna branch occurs row-wise at two OFDM symbol instants.

In the case of three active TX antennas, one of the four branches remains idle. The idle antenna can be adaptively selected after transmitting four OFDM symbols depending on the availability of CSI.

The symbol vector is denoted by $[S_1 \ S_2 \ S_3 \ 0] = [S(k,m) \ S(k,m+1) \ S(k,m+2) \ 0]$, and the code matrix according to [45] is

$$\mathbf{S}_3 = \begin{bmatrix} S_1 & -S_2^* & -S_3^* & 0 \\ S_2 & S_1^* & 0 & -S_3^* \\ S_3 & 0 & S_1^* & S_2^* \end{bmatrix},$$

where three symbols are transmitted row-wise over four symbol instants.

When all four TX antennas are deployed, again only three symbols are transmitted over the four symbol instants. Thus, with $[S_1 \ S_2 \ S_3 \ 0] = [S(k,m) \ S(k,m+1) \ S(k,m+2) \ 0]$, the code matrix according to [45] is given as

$$\mathbf{S}_4 = \begin{bmatrix} S_1 & -S_2^* & -S_3 & 0 \\ S_2 & S_1^* & 0 & -S_3^* \\ S_3 & 0 & S_1^* & S_2^* \\ 0 & S_3 & -S_2 & S_1 \end{bmatrix}.$$

Note that the transmit power per antenna branch has been equally scaled down by $10\log_{10}(\mathbf{S}_{K_T})$ dB to ensure same power constraint as for the SISO case.

5.4.2 MIMO Combining

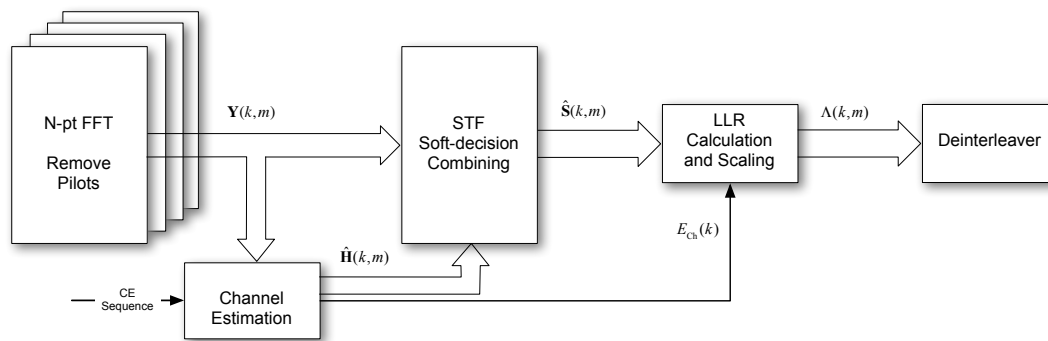


Figure 5.9: Block diagram of STF soft-decision combining with scaled LLR calculation.

As mentioned before, main advantage of the orthogonal STF coding is the low complexity of combining at the receiver (as compared to pure ML solutions), which typically implies linear processing similar to the Alamouti simple algebraic combining. Due to the orthogonality of the MIMO code, decoding of a transmitted symbol can be performed independently of all other symbols within the code word. It is further shown in [25],[46] that providing soft-decision information to the succeeding channel decoding may improve the reliability of error correction. In fact, extracting the Log-Likelihood Ratios (LLRs) out of the decoded symbols and scaling them by the channel energy

ensures that the highest post-processing SNR is obtained and that the FEC decoder can find the ML code word. This approach is illustrated in Figure 5.9, where the soft outputs $\hat{S}(k,m)$ of the MIMO combining block are used to calculate the scaled LLRs $\Lambda(k,m)$ and delivered to the deinterleaver and FEC decoder. Further details on the calculation of the scaled LLRs are given in Section 5.4.3 and [46].

In the following, we provide the algebraic combining rules for the considered three coding schemes.

For Alamouti transmission, the MIMO combiner calculates the soft estimates over two successive time instances $[\hat{S}_1 \ \hat{S}_2]=[\hat{S}(k,m) \ \hat{S}(k,m+1)]$ out of the received symbols $Y_j(k,m)$ and $Y_j(k,m+1)$ as

$$\begin{aligned}\hat{S}_1 &= \frac{\sum_{j=1}^{N_R} Y_j(m)H_{j1}^* + \sum_{j=1}^{N_R} Y_j^*(m+1)H_{j2}}{\sum_{j=1}^{N_R} \sum_{i=1}^2 H_{ji}^* H_{ji}}, \\ \hat{S}_2 &= \frac{\sum_{j=1}^{N_R} Y_j(m)H_{j2}^* - \sum_{j=1}^{N_R} Y_j^*(m+1)H_{j1}}{\sum_{j=1}^{N_R} \sum_{i=1}^2 H_{ji}^* H_{ji}}.\end{aligned}\quad (5.7)$$

Because of the assumption of a quasi-static channel during the transmission of a frame, the relation $H_{ji}(k) = H_{ji}(k,m) = H_{ji}(k,m+l)$ holds true. Without losing generality, we have omitted the subcarrier index k for brevity.

In the case of three TX antennas being deployed, and having received the symbols $Y_j(k,m) \dots Y_j(k,m+3)$, the combined estimates of the transmitted symbols are

$$\begin{aligned}\hat{S}_1 &= \frac{\sum_{j=1}^{N_R} Y_j(m)H_{j1}^* + \sum_{j=1}^{N_R} Y_j^*(m+1)H_{j2} + \sum_{j=1}^{N_R} Y_j^*(m+2)H_{j3}}{\sum_{j=1}^{N_R} \sum_{i=1}^3 H_{ji}^* H_{ji}}, \\ \hat{S}_2 &= \frac{\sum_{j=1}^{N_R} Y_j(m)H_{j2}^* - \sum_{j=1}^{N_R} Y_j^*(m+1)H_{j1} + \sum_{j=1}^{N_R} Y_j^*(m+3)H_{j3}}{\sum_{j=1}^{N_R} \sum_{i=1}^3 H_{ji}^* H_{ji}}, \\ \hat{S}_3 &= \frac{\sum_{j=1}^{N_R} Y_j(m)H_{j3}^* - \sum_{j=1}^{N_R} Y_j^*(m+2)H_{j1} - \sum_{j=1}^{N_R} Y_j^*(m+3)H_{j2}}{\sum_{j=1}^{N_R} \sum_{i=1}^3 H_{ji}^* H_{ji}}.\end{aligned}\quad (5.8)$$

Finally, when MIMO coding with all four TX antennas is applied, the combined estimates of the transmitted symbols are calculated from the received tones $Y_j(k, m) \dots Y_j(k, m+3)$ as

$$\begin{aligned}
\hat{S}_1 &= \frac{\sum_{j=1}^{N_R} Y_j(m)H_{j1}^* + \sum_{j=1}^{N_R} Y_j^*(m+1)H_{j2} + \sum_{j=1}^{N_R} Y_j^*(m+2)H_{j3} + \sum_{j=1}^{N_R} Y_j(m+3)H_{j4}^*}{\sum_{j=1}^{N_R} \sum_{i=1}^4 H_{ji}^* H_{ji}}, \\
\hat{S}_2 &= \frac{\sum_{j=1}^{N_R} Y_j(m)H_{j2}^* - \sum_{j=1}^{N_R} Y_j^*(m+1)H_{j1} - \sum_{j=1}^{N_R} Y_j(m+2)H_{j4}^* + \sum_{j=1}^{N_R} Y_j^*(m+3)H_{j3}}{\sum_{j=1}^{N_R} \sum_{i=1}^4 H_{ji}^* H_{ji}}, \\
\hat{S}_3 &= \frac{\sum_{j=1}^{N_R} Y_j(m)H_{j3}^* + \sum_{j=1}^{N_R} Y_j(m+1)H_{j4}^* - \sum_{j=1}^{N_R} Y_j^*(m+2)H_{j1} - \sum_{j=1}^{N_R} Y_j^*(m+3)H_{j2}}{\sum_{j=1}^{N_R} \sum_{i=1}^4 H_{ji}^* H_{ji}}.
\end{aligned} \tag{5.9}$$

As in Alamouti combining, also the estimators for three and four TX antenna MIMO are unbiased and maximize the post-processing SNR of the estimates. The denominator term in (5.7), (5.8) and (5.9) reflects the channel energy per subcarrier and will be used as scaling factor for the LLR calculation described below.

5.4.3 Bitwise LLR Demodulation

The basic idea behind the bitwise LLR demodulation is to deliver the reliability information contained in the soft outputs of the STF combining all the way down to the FEC decoder. The Log-Likelihood Ratio λ_q expresses the probability of a given transmitted bit on position q being equal to one versus zero, and is defined as

$$\lambda_q = \ln \left(\frac{\Pr(b_q = 1 | \hat{S})}{\Pr(b_q = 0 | \hat{S})} \right).$$

With the assumption of Gaussian distributed noise of zero mean and variance σ_n^2 , the LLR becomes the difference of two exponents that can be further approximated by taking into account only the two closest constellation points with opposite b_q . It has been shown in [46] that with separate bit mapping onto the real and imaginary part of a Gray-mapped constellation, the approximate LLR reduces to a linear function in the distance between the received symbol and the midpoint of those two constellation points along the given (real or imaginary) dimension. Note that the noise variance along a dimension reduces then to $\sigma_1^2/2 = \sigma_Q^2/2 = \sigma_n^2/2$.

For QPSK with unity average power, the components of the LLR vector $\left[\lambda_1 \quad \lambda_0 \right]$ are given by

$$\lambda_1 = \frac{\sqrt{2}}{\sigma_n^2} \hat{S}_1 \quad \text{and} \quad \lambda_0 = \frac{\sqrt{2}}{\sigma_n^2} \hat{S}_Q, \quad (5.10)$$

where \hat{S}_1 is the I-coordinate, and \hat{S}_Q is the Q-coordinate of the estimated symbol.

For normalized 16-QAM, the approximations of the elements of the LLR vector $\left[\lambda_3 \quad \lambda_2 \quad \lambda_1 \quad \lambda_0 \right]$ are calculated as [46]

$$\begin{aligned} \lambda_3 &\approx \frac{2 \hat{S}_1}{\sqrt{10} \sigma_n^2}, & \lambda_2 &\approx \frac{-2}{\sqrt{10} \sigma_n^2} \left(|\hat{S}_1| - \frac{2}{\sqrt{10}} \right), \\ \lambda_1 &\approx \frac{2 \hat{S}_Q}{\sqrt{10} \sigma_n^2}, & \lambda_0 &\approx \frac{-2}{\sqrt{10} \sigma_n^2} \left(|\hat{S}_Q| - \frac{2}{\sqrt{10}} \right). \end{aligned} \quad (5.11)$$

This approximation tends to be very close to the true values and proves to have a negligibly small impact on the error performance. Furthermore, as the noise samples are essentially divided by the channel attenuation during signal equalization, their variance is called the channel energy. In order to obtain the correct noise variance in each LLR estimate, we scale it back by first setting the noise power to unity, and then multiplying it with the channel energy term $E_{\text{ch}}(k) = \sum_j \sum_i H_{ji}^*(k) H_{ji}(k)$.

Neglecting this scaling would lead to suboptimal soft decisions if the channel fluctuations become large.

We next compare the measured BER performance of the proposed STF combing schemes at the output of the channel decoder. The measurements have been performed in 1m LOS environment on BG1 with TFC6, using linear patch antenna arrays and varying the number of TX and RX antennas. In order to obtain fair comparison among the different STF coding schemes, we set the total code rate to approximately 1/2, as for the full-rate Alamouti scheme with rate $R_c = 1/2$ channel coding. Therefore, for the 3/4-rate orthogonal schemes with QPSK and 16-QAM modulation, we select modes with channel code rate $R_c = 3/4$ to achieve total code rate of $3/4 R_c = 18/32$, which is close enough to 1/2.

The performance results in Figure 5.10a) indicate that the orthogonal STF codes for three or four TX antennas are able to outperform the Alamouti code for equal total rate in the system. However, due to imperfect channel estimation and the resulting error propagation in the decoding stages of the RX, the diversity gain brought by using multiple antennas on both ends of the link diminishes. This becomes evident especially for higher order modulations (e.g. 16-QAM) with shorter distance between the constellation points, where using an erroneous channel estimate affects the correct demapping of a higher number of bits, see Figure 5.10b).

In Figure 5.11a), the measured performance of 4×2 orthogonal STF decoding is depicted as function of the decision type of the channel decoding block. As expected, soft decision input to the Viterbi decoder provides an SNR improvement of ca. 2 to 2.5 dB to the system, whereas an additional 1 dB due to the scaling of the LLR metric is observed. Finally, in Figure 5.11b), we investigate the performance of the 4×2 STF decoder for different antenna spacing. It can be concluded that separating the array elements by half the maximum wavelength of the signal results in lower values of the spatial correlation and therefore less error propagation in the channel estimation and equalization.

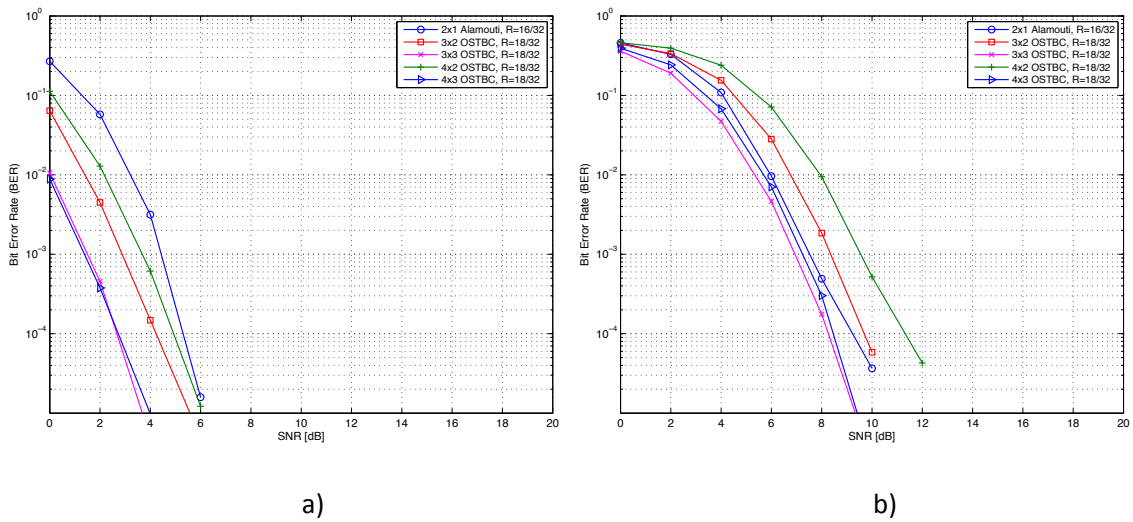


Figure 5.10: Measured BER performance of orthogonal STFC (total rate $R=18/32$, TFC6) for different antenna configurations and modulations: a) QPSK, and b) 16-QAM.

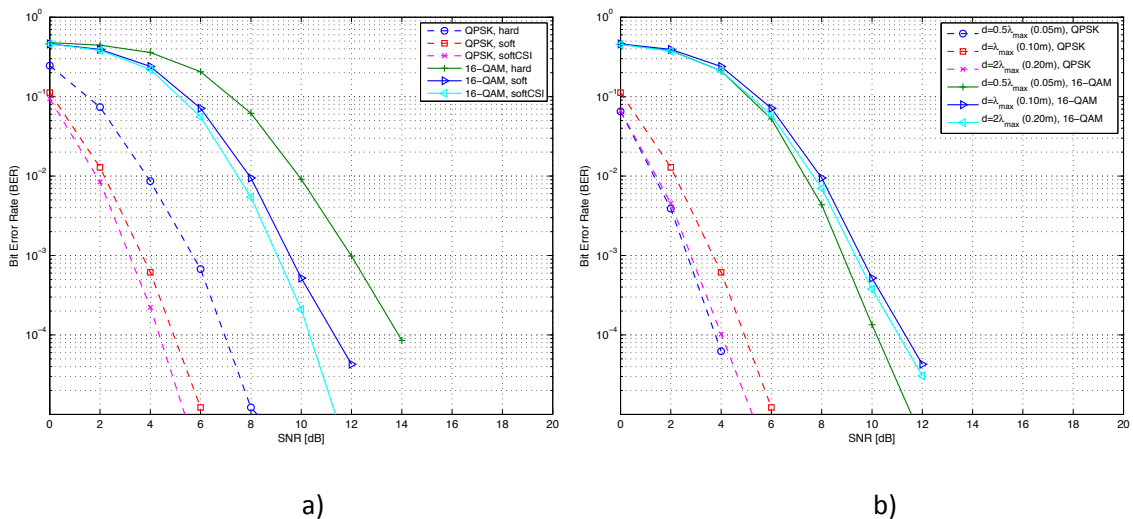


Figure 5.11: Measured BER performance of 4×2 orthogonal STFC (total rate $R=18/32$, TFC6) for different data rates as function of the a) decision type, and b) antenna spacing d .

5.5 Differential Algorithm for Interference Detection and Mitigation

Due to its “underlay” nature, UWB technology has to ensure the coexistence with other services operating in the same frequency range. This implies that the UWB system has to be able to detect and potentially avoid such primary users, as well as to adjust its parameters respectively so that no harmful interference is caused at victim receivers. Besides common co-existence techniques such as Low Duty Cycle (LDC), Transmit Power Control (TPC) and lower TX emission masks, regulatory bodies in Europe have imposed the use of the so-called Detect-And-Avoid (DAA) protection mechanism for Band Group 1. According to it, a UWB device should immediately switch to another sub-band or zero/null its corresponding tones of transmission, once an incumbent is detected in its band of operation. In case the device is not capable of performing DAA, it shall reduce its EIRP power emission to a rather prohibitive (in term of reliable communication) PSD level, see Figure 2.1.

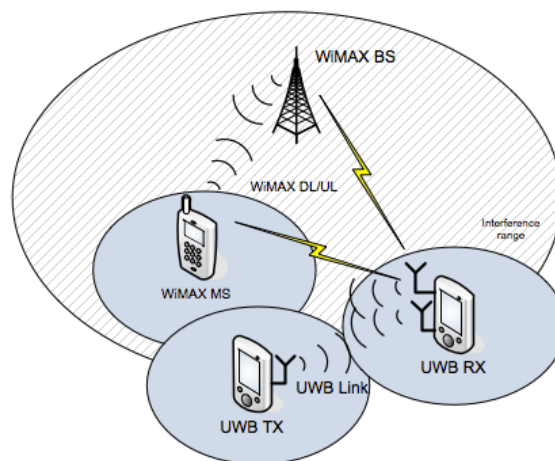


Figure 5.12: Co-existing scenario between UWB and WiMAX.

To demonstrate the DAA capabilities of UWB technology, we consider the following interference scenario: a primary user (e.g. WiMAX mobile terminal) operates in close proximity of a point-to-point UWB link, see Figure 5.12. During its start-up, the UWB communication system performs a spectrum scan of the environment to possibly detect and mitigate its interference towards the WiMAX terminal. The CEPT ECC TG3 have proposed a so-called flexible zone model for DAA, according to which the space around the victim receiver is separated in different zones depending on the received power of a primary user [47]. Depending on the detected interference level, the UWB device applies a relevant mitigation technique, e.g. dropping of a sub-band, tone nulling or analogue/digital notch filtering. Further, the presented DAA procedures can be elaborated to include coherent spectrum sensing and monitoring phase to better estimate the isolation distance from the victim receiver as well as to reduce the overhead for scanning the whole environment.

Table 5.1 summarizes the main set-up parameters for the proposed WiMAX interference test scenario. Since the required WiMAX DL sensitivity (detection level) is -90 dBm (or -97 dBm/MHz), the received WiMAX signal lies only 10.4 dB ($= -97 - 6.6 + 114$) above the WiMedia noise floor. The

challenging task of detecting the victim signal in harsh multipath environment and shadowing effects may be alleviated by increasing the integration period of the detection algorithm, using some a-priori knowledge of the incumbent system or exploiting the intrinsic receive diversity via multiple antennas.

Table 5.1: Parameters of the WiMAX interference scenario.

Parameter	Value
WiMAX TX UL power	20 dBm
WiMAX Bandwidth	5 MHz
WiMAX min DL sensitivity	-90 dBm
WiMAX Noise Figure (NF)	5 dB
WiMAX carrier frequency	3.5 GHz
SIR at WiMAX RX	- 6 dB
Thermal noise	-114 dBm/MHz
WiMedia signal level	-41.3 dBm/MHz
WiMedia Noise Figure	6.6 dB
Protection level	-60 dBm/MHz -65 dBm/MHz
Channel availability check-time	<= 50 ms

In this section we propose a differential algorithm for MB-OFDM receivers based on non-coherent energy detection of interfering or primary user signals. As specified in the interference scenario (see Table 5.1), the detection of a 5 MHz signal is considered, whereas the energy detector accumulates the FFT bins over a multiple of MB-OFDM symbol instants. The output of the detector is differentially compared with a detection threshold, and the bins that result in positive hypothesis tests indicate the presence of WiMAX transmissions.

The UWB receiver can deploy the sensing function to scan the spectrum continuously for WiMAX emissions during the start-up phase. A sensing phase of 30 up to 70 symbol slots is considered sufficiently long to detect reliably the WiMAX UL/DL signal. In case the UWB device fails to detect the victim device during this initial check, it will continue to monitor the environment on an on-going base, e.g. during the beaconing phase or the transmission-free intervals between two data frames.

The flow chart of the proposed interference detection scheme is shown in Figure 5.13. The algorithm takes as parallel input the averaged FFT bins over all RX antennas during a set number of slots. Depending on the time-frequency hopping pattern, the symbol blocks are accumulated in a normalized power array $\mathbf{p} = [p(1), p(2), \dots, p(k), \dots, p(N)]$, corresponding to up to three sub-bands

within a band group. After initializing $p_{\text{sum}}(1) = p_{\text{diff}}(1) = p(1)$, each power bin is decremented by the average of the preceding bins and then compared with a detection threshold. If the power of this differential bin exceeds the threshold, its index is output, while its value is neglected for the calculation of the supplementary moving sum array \mathbf{p}_{sum} . In case a bin value lies below the threshold, the moving sum is incremented by its value, after which the value is replaced by the increment of the moving sum, see Figure 5.13.

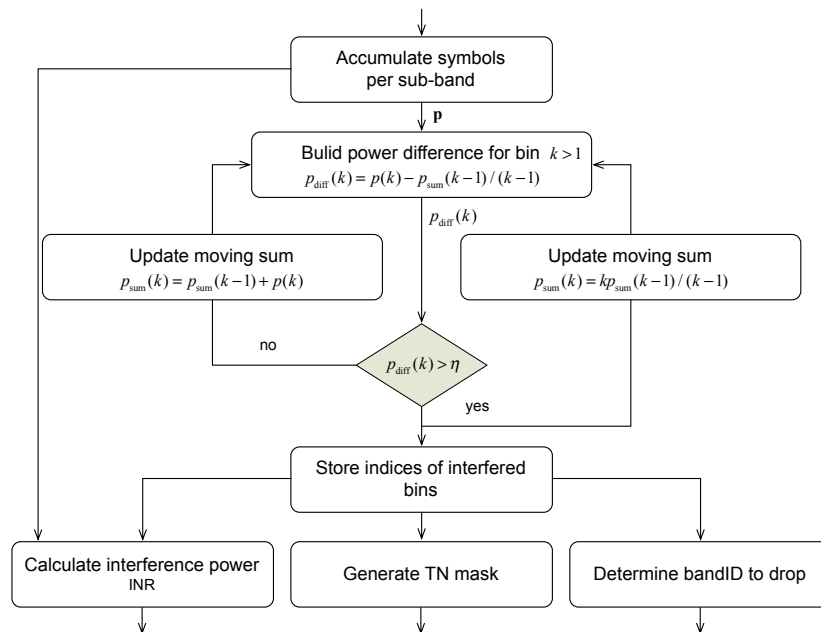


Figure 5.13: Flow diagram of per-bin differential interference detection.

In case of successful detection, the sub-band(s) corresponding to the detected interferer index is determined and fed back to the TX in order to perform e.g. band dropping techniques. Further, a binary tone-nulling (TN) mask for each sub-band is generated, containing 1's for each sub-carrier to be transmitted, and 0's for the tones to be zeroed. Variable number of guard tones N_{TN} are zeroed on both sides of the detected bin in order to allow for deeper notching of the transmit UWB signal.

Finally, the power level of the detected interferer and Interference-to-Noise Ratio (INR) are estimated, and a flag for successful detection is output. The power of the interferer may then be used to determine the interference zone and required isolation to the victim device.

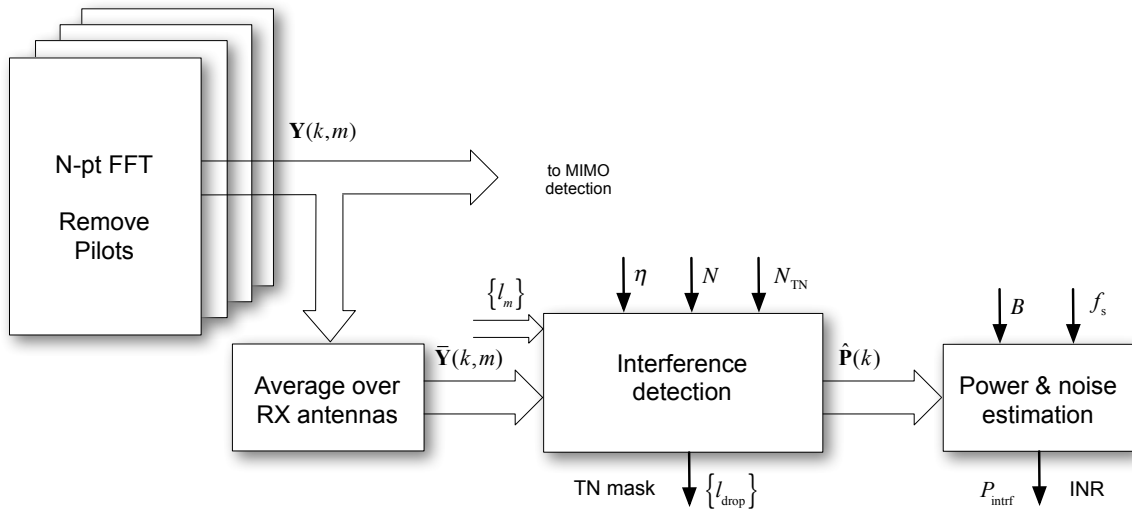


Figure 5.14: Block diagram of interference detection.

In order to verify the performance of the per-bin interference detector, we consider a MIMO MB-OFDM receiver deploying 4 antennas. The block diagram of the interference detection scheme including multiple FFT-, tone demapping and symbol averaging blocks is shown in Figure 5.14. The outputs of the N_R FFT blocks are first averaged over the all RX antennas and then fed in parallel to the interference detection block. The input $\bar{Y}(k,m)$ to the interference detector contains $N \times M$ tones (frequency bins), where M stands for the number of slots/instants the detection is to be carried over. The sequence $\{l_m\}$ specifies the time-frequency hopping pattern (TFC) of the receiver and contains the BandID values over 6 consecutive time instants. The parameters η , N , N_{TN} , B , and f_s define the normalized detection threshold, FFT-size, number of TN guard tones, system bandwidth and sampling frequency respectively. The interference detection block essentially accumulates the power levels on each frequency bin and sub-band, and outputs a sequence $\{l_{drop}\}$ of the sub-band(s) to be dropped, as well as a binary TN mask with zeros at each subcarrier index that has to be nulled during transmission of the next frame, see Figure 5.13. The succeeding block calculates the average interferer power level P_{intrf} and returns an estimate of the Interference-to-Noise (INR) ratio.

The probability of interference detection (P_{iDet}) of the proposed scheme is shown in Figure 5.15. One can conclude that integrating over only 30 slots already provides sufficiently high levels of P_{iDet} (e.g. above 90%), thus allowing for reliable and fast detection of a WiMAX uplink for very low levels of the interference-to-noise ratio (INR). Deploying multiple antennas at the receiver side improves the detection performance by up to 6 dB, owing to the intrinsic array gain and noise averaging, see Figure 5.15b).

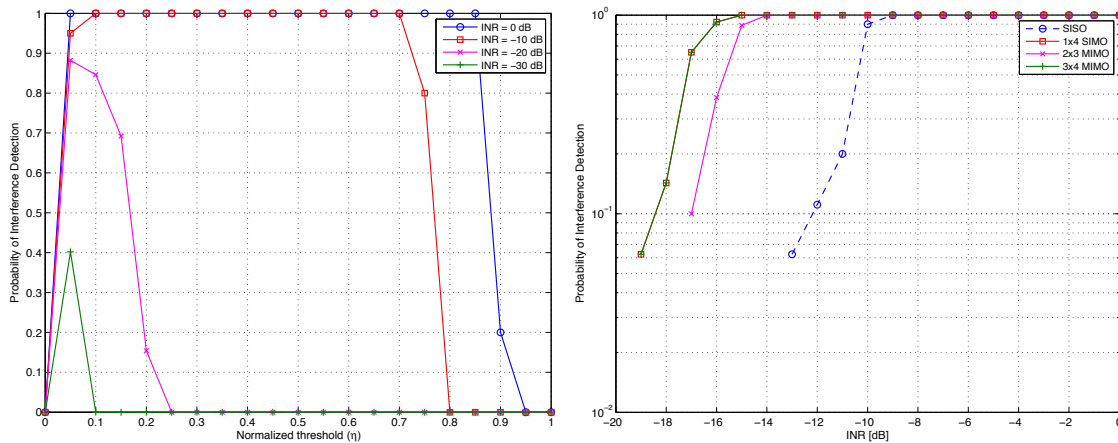


Figure 5.15: Performance of WiMAX interference detection for a) 3×4 MIMO and different values of the INR, and b) different antenna configurations for fixed threshold ($\eta = 0.3$) in CM1.

5.6 On the Implementation Complexity of MIMO MB-OFDM

5.6.1 Transceiver Architecture, Power Consumption and Silicon Area

As stated before, the proposed MIMO MB-OFDM system deploys spatial multiplexing with the goal to achieve linear increase in capacity. Splitting the input binary stream into N_T independent data streams would imply significant replication in both the transmitter and receiver architectures, where each sub-stream passes a separate antenna branch, as shown in Figure 4.1. Although the hardware and complexity costs are proportional to the number of transmit antennas, this approach offers the possibility to independently vary the parameters of the component blocks on each branch, and thus introduces a high degree of flexibility in the overall design of the system.

Given the fact that during a time slot all antenna branches transmit in the same frequency band, a common oscillator and frequency synthesis circuit can be shared. Besides reducing the complexity and power consumption, this also alleviates the problem of center frequency offsets among the separate TX RF front-ends. Further saving in area and power consumption can be achieved by a common pipelined IFFT processing, as will be discussed in the following section.

A different area-saving approach is to use a common encoder, puncturing and interleaving block, which output is then demultiplexed across the separate antenna branches. However, this implies increased processing rate of the encoder, which may become unfeasible in terms of power consumption for clock rates exceeding 1 GHz.

The receiver architecture of the proposed VHDR MIMO MB-OFDM system is based on a replicated direct-conversion SISO RX featuring additional blocks for channel estimation and MIMO combining. Similar to the TX architecture, it implies replicating most of the RF- and baseband processing blocks

of the single antenna receiver. In the digital baseband, the pipelined FFT processing approach can still reduce the HW costs of the MIMO RX. Further significant increase in complexity and power consumption is caused by the MIMO combining block, which has to extract the independent streams from the mixture of received signals. It is therefore essential to point out efficient schemes for MIMO detection that could allow for reductions of the RX complexity and a feasible implementation.

5.6.2 RF Frontend

The receiver frontend of a V-BLAST architecture consists of replicated RF antenna branches, each containing a pre-select BP filter, LNA, AGC, mixers and ADCs (one for each I and Q-component). Depending on the implementation, the deployed antennas and BP filters may have to be designed to operate either in the lower bands (3.1 GHz to 4.8 GHz) and/or the upper band of 6 GHz to 9 GHz. Similar to the TX, the frequency synthesis circuit can be shared among the receive branches, reducing the area, power consumption and mismatch between CFO offsets on different branches. To simplify the overall complexity of the receiver, the system could operate only in FFI mode, which will significantly alleviate the requirements for fast frequency switching, time and frequency synchronization and tracking, channel estimation and MIMO combining, as these have to be performed for a single sub-band only.

Regarding the area of the MIMO RX frontend, one may expect to end up with about 70% area increase for each additional antenna. A practical approach to facilitate implementation could be to develop a single antenna frontend-chip with appropriate interfaces so that one could easily connect two or more of them together to come to a multiple MIMO-suited frontend. In this case it will not be necessary to develop a separate chip for single, dual, triple, etc. number of antennas, but rather merely combine the required number of chips in a single package.

5.6.3 Efficient Multichannel FFT Processing

The FFT processing in an OFDM-based system is one of the high complexity modules, which typically account for a quarter of the power consumption of the system. In a spatially multiplexed VHDR MIMO MB-OFDM system, separate (I-)FFT processing is required to modulate the independent data streams on each TX branch. A straightforward approach of replicating the number of FFT processors would imply a dramatic increase also in the complexity and area needed, with the only advantage of using standard SISO FFT components, which do not have to be adjusted for MIMO transmission.

An alternative solution is offered by pipeline FFT processors, which feature multi-channel structure optimized for MIMO communication. In the case of e.g. WLAN MIMO-OFDM systems, a multi-channel mixed-radix pipeline FFT processor (MRMDC) is reported in [48], [49] to reduce the required number of logic gates by up to 25% with respect to conventional MIMO FFT processors like R4MDC. Compared to using typical SISO-OFDM FFT processors such as the R2³SDF in parallel, these savings

can reach up to 64% of the logic gates count for a 4×4 MIMO-OFDM system. Table 5.2 summarizes the hardware requirements of the mentioned FFT architectures.

Table 5.2: Comparison of FFT hardware requirements for K MIMO branches

Processor description	Number of processors (P)	Complex multipliers per P	Complex adders per P	Memory size per P
R2SDC	K	$\log_2 N - 1$	$2 \log_2 N$	$N - 1$
R2 ³ SDF	K	$(2/3)\log_2 N - 2$	$(2 + 2T/3)\log_2 N$	$N - 1$
R4MDC	$\lceil K/4 \rceil$	$(3/2)\log_2 N - 3$	$4\log_2 N$	$5N/2 - 4$
MRMDC	$\lceil K/4 \rceil$	$(4/3)\log_2 N - 4$	$(4 + T)\log_2 N$	$5N/2 - 4$

* N = FFT size, T = Number of adders required for a trivial multiplication

Regarding efficient MIMO FFT processing for MB-OFDM UWB systems, a similar 8-path pipeline approach is reported in [50] to enable 1-Gbps throughput at a clock frequency of 125 MHz in an FPGA implementation. While these solutions argue on reduced power consumption and optimized utilization of complex multipliers and FIFO registers as compared to SISO FFT-processing, exact savings are still highly dependent on the actual implementation platform and need further verification by system designers.

5.6.4 FPGA Implementation Complexity of the Proposed MIMO Algorithms

In order to obtain realistic estimates of the hardware resource utilization, the selected MIMO decoders have been implemented by partner VTT of the FP7 IP EUWB on a Xilinx ML605 FPGA board which has been connected in a HW-in-the-loop simulation to the MIMO-UWB test-bed. Besides the SISO MMSE reference mode and the differential interference detector, the 2×2 QRD-based linear MMSE receiver, the 3×4 MMSE-based SQRD SIC, as well as the 4×2 STF decoder have been selected for FPGA implementation.

Table 5.3 summarizes the findings on the FPGA resource consumption of the selected MIMO algorithms in [26]. In this proof-of-concept implementation, the synthesis results demonstrate that the FPGA implementation of the proposed MIMO algorithms is feasible for modern FPGA circuits. The resource utilization and performance results may serve as reference basis for designers considering a hardware implementation of MIMO decoders for next generation UWB devices. More details on the FPGA implementation and e.g. scalability of the 3×4 MMSE-based SQRD SIC can be found in [26].

Table 5.3: Synthesis of selected MIMO algorithms to XCVLX240T FPGA.

Resource utilization	Max. clock frequency	Max. PHY throughput*	DSP48 slices	LUTs	Registers	Block RAM
SISO MMSE	180 MHz	540 Mbps	7 (0.9%)	1159 (0.7%)	2139 (0.7%)	2 (0.5 %)
2×2 MMSE with QRD	210 MHz	1260 Mbps	137 (17%)	12551 (9%)	13653 (4%)	29 (6%)
3×4 MMSE-SQRD	160 MHz	1440 Mbps	236 (30%)	48560 (31%)	54908 (17%)	185 (44%)
4×2 STF Decoder	160 MHz	360 Mbps	122 (15%)	14318 (9%)	11214 (3%)	20 (4%)
Interference Detector	100 MHz	NA	11 (1%)	7785 (2%)	7897 (2%)	1 (0.2%)

*The maximum achievable throughput at PHY is calculated for code rate 3/4 and 16-QAM modulation

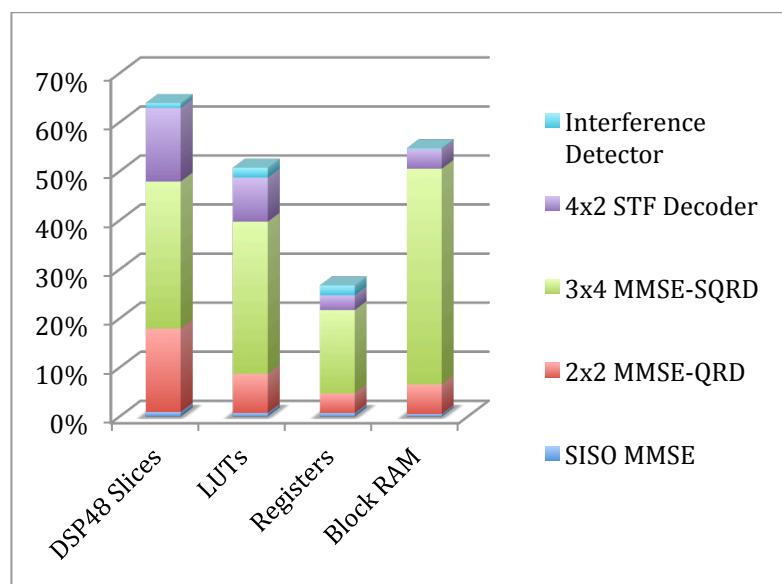


Figure 5.16: Resource utilization of the implemented MIMO algorithms on XCVLX240T FPGA platform.

5.7 Conclusions

In this chapter, multiple antenna approaches for very high data rates based on spatial multiplexing, Dual Mode transmission and Space-Time-Frequency Coding have been investigated, developed and verified. For V-BLAST architectures, efficient algorithms for matrix inversion with sorted QR decomposition and ordered successive interference cancellation have been proposed. The algorithm and overall system performance have been verified via simulations and the offline MIMO-UWB test-bed, considering the impact of real-world propagation constraints, synchronization in time- and frequency, as well as the estimation and compensation of imperfections in the receiver front-end.

For coded 3×4 MIMO MB-OFDM with spatial multiplexing, the both MMSE-QRD and MMSE-based O-SIC receiver performances of the VHDR mode are only slightly degraded as compared to that of an exhaustive search ML decoder. Moreover, under strong LOS transmission over very short distances, we have demonstrated that especially for symmetric MIMO systems the deployment of dual-polarized antennas or Dual Mode transmission can significantly improve the system performance in terms of error propagation.

For transmit diversity schemes, we have provided an orthogonal STF coding framework including simple algebraic rules for reliable decoding in MIMO systems deploying up to 4 TX and arbitrary number of RX antennas. Moreover, we propose an efficient approach of delivering soft-decision inputs to the channel decoding stage, by scaling the LLR metric with the estimated channel energy. The performance results indicate improvement of the minimum required SNR at the receiver that allows for an overall coverage improvement of the system.

Finally, we propose a low-complexity approach for robust interference detection in order to enable the deployment of flexible DAA mechanisms via Band-Dropping or Tone Nulling.

Chapter 6

Performance Verification via the MIMO-UWB Test-bed

While UWB offers an additional degree of freedom for communications through its huge bandwidth, the research and development on MIMO UWB and especially its implementation aspects is still in its infancy compared to the numerous contributions and practical solutions for narrow-band and wideband MIMO (as in e.g. IEEE 802.11n, 802.16e or 3GPP LTE). In particular, only few measurement results exist to demonstrate and verify the theoretical achievements and algorithm solutions for MIMO UWB systems [51]-[53]. This is mainly due to the fact that test equipment suitable for UWB measurements is still expensive and often does not meet the requirements for flexible design and investigation of sophisticated wireless transmissions like those in multiple antenna systems. Instead, most research in the field of MIMO UWB is carried out through accurate but often simplified MATLAB simulations, thus neglecting the effects of realistic imperfect channels or other real-world phenomena like fixed-point computing, RF impairments and imperfect synchronization on the performance and robustness of MIMO algorithms. In order to study and eventually overcome these uncertainties, extensive testing and verification of these approaches under close-to realistic conditions has to be performed.

Among the increasing number of experimental platforms developed over the recent years to evaluate the performance gains of MIMO technology, one can distinguish three general systems [54][55]:

- *prototype* – is an initial realization of a developed approach or a standard, intended to serve as proof of concept or instrument for future research and improvements;
- *demonstrator* – typically serves to show the feasibility and functionality of a system concept or development;
- *test-bed* – is a general research tool for further development and verification of algorithms under real-world conditions. It is aimed to provide significantly more exhaustive data under variable set of application scenarios and better knowledge about the behaviour of the MIMO channel than pure simulations, which often rely on numerous assumptions and simplified mathematical models. Therefore, a major requirement for this experimental platform is its high scalability, modularity and extendibility.

Regarding the real-time aspect of such an experimental system, it is classified as

- *offline* – where signal generation, acquisition and processing are performed without stringent timing constraints. This allows for the evaluation of highly scalable and modular system designs, however providing little support of feedback loops and knowledge on implementation complexity;
- *real-time* – featuring continuous, on-the-fly operation and processing of the algorithms under test. Due to their stringent time and complexity constraints, UWB real-time platforms are difficult to implement and highly rely on the availability of suitable RF and baseband components.

6.1 Experimental MIMO-UWB Test-bed

As mentioned in the description of the system concept, the offline MIMO-UWB test-bed enables performance verification of arbitrary system and algorithm designs by offering a real-air interface for up to 4×4 MIMO single- and multi-user configurations. Depending on the application scenario and selected MIMO scheme, the signal waveforms can be generated under the common MATLAB environment and then easily transmitted via the MIMO-UWB test-bed. While this approach preserves the flexibility and modularity of algorithm development, it allows for evaluation of the achievable performance gains under the effects of real-world phenomena such as hardware specific non-ideal behaviour, fixed-point implementations and channel propagation constraints.

Hereafter, we describe the general setup and capabilities of the developed offline MIMO-UWB test-bed.

6.1.1 General Set-up and Verification Environment

The main hardware components of the 4×4 offline MIMO UWB test-bed are two arbitrary waveform generators (AWGs) and a digital phosphor oscilloscope (DPO) available at the MIMO-UWB Laboratory at IKT, as shown in Figure 6.1. Waveform generation, instrument control signalling and data processing are performed on a Host PC, which is connected to the measurement devices via Gigabit LAN.

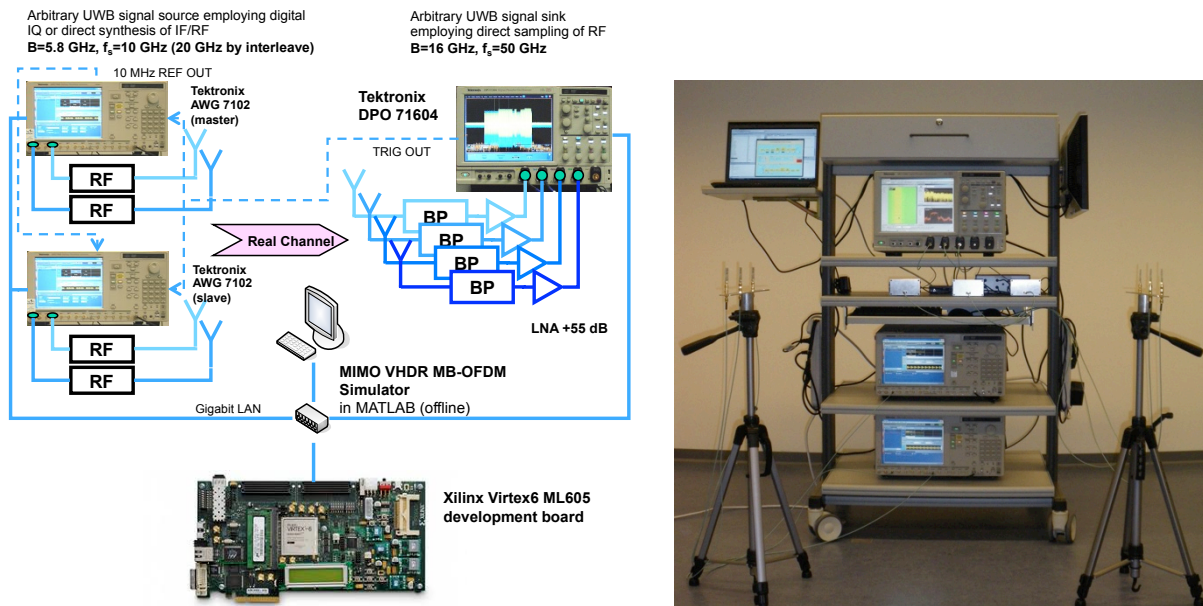


Figure 6.1: General setup of the MIMO-UWB test-bed

6.1.2 Transmitter

On the transmitter side, each Tektronix AWG7102 supports two channels with up to 10 GSPS and 5.8 GHz analogue bandwidth (or one interleaved channel with up to 20 GSPS), as well as 32 Msample waveform length per channel. The AWG enables the direct generation of RF signals, via the DAC, up to the effective frequency of 5.8 GHz with the capability to add real-world signal imperfections. The direct synthesis of IF or RF signals avoids I/Q degradations and time-consuming adjustments associated with traditional methods using I/Q modulators.

The main specifications of AWG7102 are summarized in Table 6.1. Each channel may be used either for baseband I/Q or direct IF/RF synthesis of arbitrary digital waveforms complying with the maximum available bandwidth. This allows for high flexibility in generating and loading various signals directly from a system-model simulator (e.g. one developed in MATLAB) without the need of up-conversion circuits and expensive UWB RF front-ends. Filtering, calibration and MIMO synchronization are therefore easily handled on a factory software basis while maintaining an acceptable signal quality.

Table 6.1: Main specifications of Tektronix AWG7102

Characteristics	Description
Waveform length	1 to 32,400,000 points (interleave is off) 1 to 64,800,000 points (interleave is on)
DAC resolution	10 bits or 8 bits (marker outputs are enabled)
Number of waveforms	1 to 16,000 waveforms

Sequence length	1 to 4,000 steps
Sequence controls	Repeat count, Wait-for-Trigger, Go-to-N, Jump
Number of analog outputs	2 (or 1 with interleaving)
Sampling rate control (with option 06)	10 MSPS to 10 GSPS (interleave is off) 10 GSPS to 20 GSPS (interleave is on)

In the evolved 4×4 MIMO set-up, the two AWGs are synchronized by a 10 MHz reference clock signal and jointly calibrated to minimize internal RF frontend mismatches. Further, a set of various sequencing commands enables the transmission of repetitive portions of the waveform through numerous program branches, jumps and loops. Therefore, it is possible to test and verify arbitrary 4×4 MIMO configurations with an upper RF frequency of 5.8 GHz without additional up-conversion. In Dual Mode operation, an external LO, band-pass pre-select filters and matched antennas are required to cover the higher frequencies of Band Group 6, see Figure 6.2.

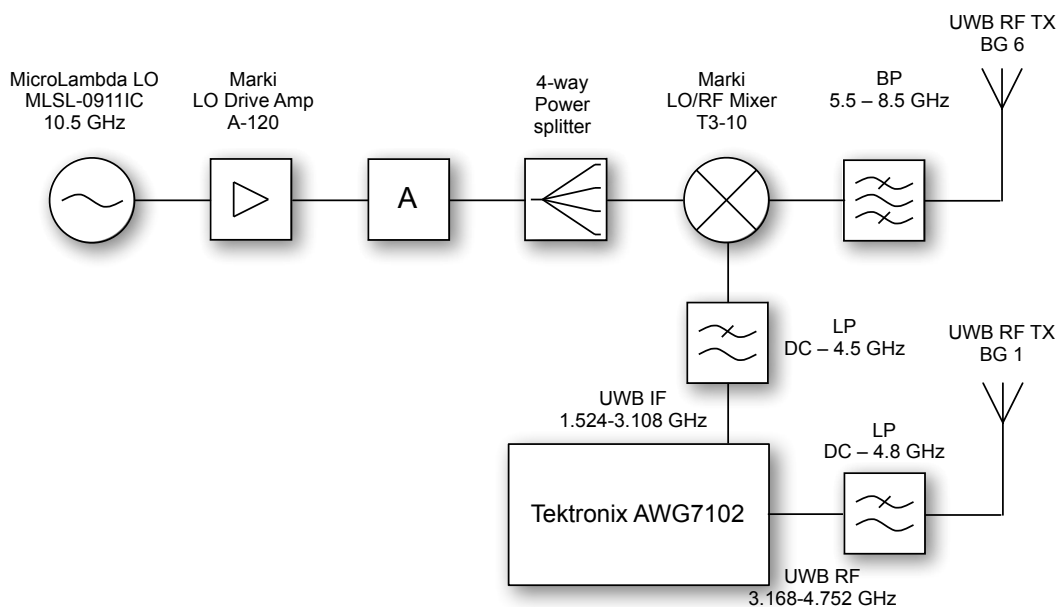


Figure 6.2: Block diagram of Dual Mode transmission via the MIMO-UWB test-bed.

For test and measurements in BG1 and BG6 we typically use small-size omni-directional UWB patch antennas, providing a maximum directive gain of 3dBi in the frequency range of 3 GHz - 4.8 GHz or 3.1 GHz -10 GHz respectively. The use of omni-directional antennas is guided by the fact that they facilitate the dense multipath propagation, which is especially favourable for MIMO transmissions. In addition, dual-polarized antennas [56], [57] developed by and courtesy of the High Frequency Institute (HFI) at LUH have been deployed in both 2×2 MIMO and Dual Mode operation (see Figure 6.11 in Section 6.3).

6.1.3 Receiver

On the receiver side, a digital phosphor oscilloscope Tektronix DPO71604 provides 4 channels with up to 50 GSPS per channel and 16 GHz analog bandwidth. The main specifications of the DPO71604 are summarized in Table 6.2. Among its time-, spectral and PSD testing capabilities, the DPO has been mainly utilized to reliably capture the transmitted MIMO waveforms for further offline processing and algorithm verification. The latter has been performed by the developed MIMO MB-OFDM data-path simulator on a fast personal computer in MATLAB.

Table 6.2: Main specifications of Tektronix DPO71604

Characteristics	Description
Input channels	4
Analog bandwidth (-3 dB)	16 GHz
Rise time 10% to 90%	27.5 ps
Input sensitivity	10mV/div to 1V/div
Vertical resolution	8 bit (11 bit with averaging)
Effective resolution	5.5 bit at 4 GHz
Max input voltage, 50 Ohm	< 1Vrms for < 1 V full scale settings < 5.5 Vrms for > 1V full scale settings
Delay between any 2 channels	< 100 ps
Max sample rate per channel	50 GSPS (real-time mode) 10 TSPS (ET/IT mode)
Max record length per channel	10,000,000 points
Real-time resolution	20 ps (50 GSPS)
Trigger types	Edge, Glitch, Runt, Width, Transition Time, Timeout, Pattern, State, Setup/Hold, Window

At the receiver frontend up to 4 UWB antennas are connected to the DPO through a bank of bandpass filters (with e.g. 1.5 GHz bandwidth) to pre-select the desired signals. These are then fed to up to 4 LNAs (MITEQ AMF-7D-00101800-30-10P) with 55 dB amplification (NF < 3 dB) for reliable acquisition under harsh SNR conditions. The trigger signal of the DPO is applied to its auxiliary output, which is connected to the trigger input of the AWG. This enables synchronous MIMO transmission and reception by triggering the DPO manually by an internal command. Both AWGs and the DPO are connected to the processing computer via Gigabit Ethernet. In combination with the data and control interface described below the MIMO test-bed allows for the fully automatic, reconfigurable and continuous generation, transmission, acquisition and processing of the MB-OFDM signals.

6.1.4 Data and Control Interfaces

The data and control interface between the AWGs, DPO and the processing computer is based on the VISA protocol (over TCP/IP) via Gigabit Ethernet. The interface from MATLAB to VISA is provided by the Instrument Control Toolbox, a versatile tool for device communication between MATLAB and measurement equipment of various manufacturers. It offers a graphical as well as a programming interface with specific functions for writing and reading data to/from, and setting up of the measurement equipment. This programming interface has been used to encapsulate the Instrument Control Toolbox within a custom GUI specialized for the MIMO test-bed requirements, as shown in Figure 6.3.

Before calling the equipment GUI, it is necessary to split the pre-processed sequence into multiple .mat-files as the AWGs and DPO have a limited record length (max 32,400,000 samples in the case of AWG). The input to the GUI is a matrix with N_T columns containing the transmit RF digitized signals, as well as a structure of predefined equipment settings. These include typical parameters such as sampling rate, record length, data format, number of used channels, but also MIMO enabling features like reference clock, triggering mode, channel coupling or sequencing commands. An automatic validation of all input parameters and status inquiry of the equipment are performed before this setup. After the Ethernet connection is established the user can select a list of .mat files created as described above. The last step is to configure the input variable containing the waveforms that should be transmitted and the output variable in which the received waveforms are to be stored. In case needed, an attenuation factor for the signal power may be optionally set. Here, no hardware knowledge or further settings are required from the user.

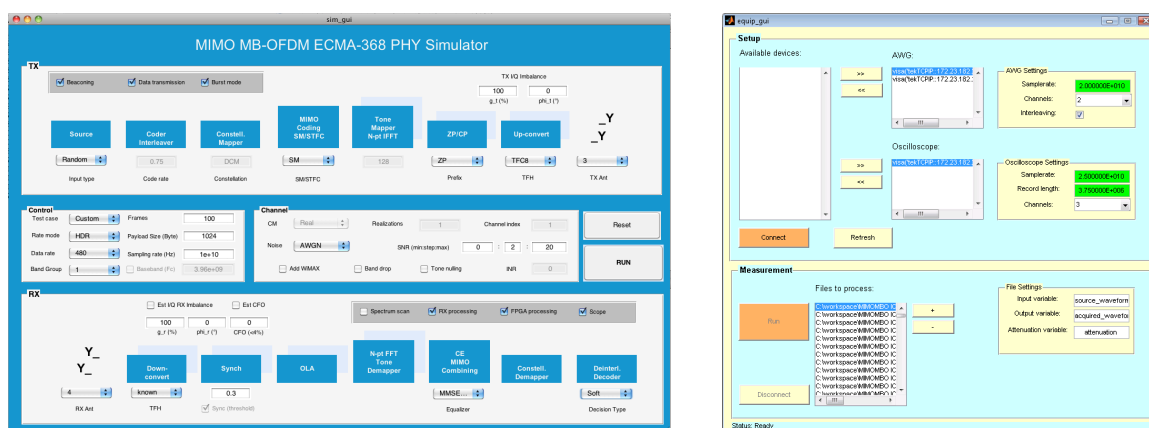


Figure 6.3: MIMO MB-OFDM MATLAB Simulator and GUI for instrument control

The input data matrix itself contains floating-point entries, whereas the numeric values represent the output voltage at each channel of the AWG. In this way, the transmit power can also be defined by software, ensuring the total allowed maximum transmit power for WiMedia devices of ca. -10 dBm has been equally allocated across all N_T outputs. This implies the same power constraint for MIMO

UWB transmission as for the single-antenna case and enables fair comparison between both systems. Since the generated transmit data is stored in files, the GUI provides additional degree of flexibility as it may be deployed in stand-alone mode or in batch mode to perform multi-mode measurements, e.g. with different number of antennas, modulation types and MIMO detectors.

Upon acquisition of the transmitted waveforms by the DPO, each receive channel is stored in a data structure directly on the processing computer. The size and format of the acquired data files is optimized to match the DPO record length, network resources and memory requirements of the processing computer. However, this procedure is very memory- and network bandwidth consuming since all sample points are internally stored in MATLAB as double precision and have to be properly converted before being written/read to/from the AWGs/DPO.

An important aspect throughout the acquisition process is the extraction of the received MB-OFDM frames from the acquired noisy sequence. In a very first stage, coarse frame synchronization is performed based on a simple threshold comparison, which becomes unreliable for very low SNR. To avoid missing part of the signal or locking at wrong portions of it, the cross-correlation coarse time-synchronization approach proposed in Section 4.2.1 has been applied to ensure accurate detection of the frame boundaries in the very low SNR regime.

6.1.5 Measurement and Verification Methodology

An important factor in carrying out the MIMO-UWB measurements is the definition and reliable estimation of the SNR at each receive branch, as this directly influences the quality of MIMO detection. In a coarse manner, we first estimate the received SNR on each antenna branch using the PSD of the band-limited RF signal and then calculate the noise power necessary to achieve a desired SNR value. Since the received signal on each antenna is the mixture of all N_T transmitted waveforms and the thermal noise, we first estimate its PSD and then subtract the average PSD of the pure noise signal between each two transmitted frames for the given frequency range. We then translate the system performance in terms of BER or FER as function of the received SNR or energy-to-noise per information bit E_b / N_0 .

6.2 Application-specific MIMO-UWB Channel Measurements

Besides the stochastic channel model described in Section 2.4.2, selected channel sounding data from the measurement campaigns in [13] have been used to verify the performance of the overall MIMO MB-OFDM system. In particular, we focus on the channel sounding performed in the A340 Mock-up at the premises of EUWB partner EADS, as well as the measurement campaign within a typical HE environment that has been carried out by partners UIL and LUH.

6.2.1 Enhancements in Spectral Efficiency

Recent studies and real channel measurements report the well-known linear increase in capacity of narrowband and broadband MIMO systems also for UWB environments [58]-[61]. In the following, we empirically calculate the ergodic MIMO-UWB channel capacity based on the estimated MIMO UWB channel transfer function acquired through our MIMO-UWB test-bed measurements. Provided that the measurement environment is fully isolated and there are no moving objects/persons in its vicinity, the MIMO-UWB channel is considered quasi-static for the duration of a single MB-OFDM frame. This ensures that the channel estimation sequence within the preamble of each frame is able to reflect the characteristics of the propagation environment and provide reliable knowledge for calculating the channel capacity. Given the sub-carrier spacing of MB-OFDM is greater than the coherence bandwidth of the frequency-selective multipath channel, the latter can be decomposed in a set of frequency-flat sub-channels. Similar to the measurement campaign reported in [60], we derive the capacity of the frequency-selective channel as the expectation of the capacities of its narrow-band components (MB-OFDM sub-carriers), resulting in $N = 128$ discrete frequency points over the frequency range of 528 MHz, i.e. with 4.125 MHz resolution. Each estimated MIMO sub-channel matrix has been normalized across all frequency bins to unity power, i.e.

$$\hat{\mathbf{H}}_{ji} := \sqrt{N} \frac{\hat{\mathbf{H}}_{ji}}{\|\hat{\mathbf{H}}_{ji}\|_2}.$$

The composite MIMO channel matrix $\hat{\mathbf{H}} = \{\hat{H}_{ji}(k)\}_{k=1}^N \in \mathbb{C}^{N_R \times N_T \times N}$ comprises the estimated $N_R \times N_T$ channel matrices over all frequency bins.

The ergodic capacity of the frequency-selective MIMO-UWB channel over the frequency range B is therefore

$$C_{\text{erg}} = \mathbb{E} \left\{ \frac{1}{B} \sum_{k=1}^N \log_2 \det \left(\mathbf{I} + \frac{\rho}{N_T} \hat{\mathbf{H}}^H(k) \hat{\mathbf{H}}(k) \right) \Delta f \right\} \quad [\text{bit/s/Hz}], \quad (6.1)$$

where ρ is the estimated SNR, B is the system bandwidth, and $\Delta f = 4.125$ MHz is the sub-carrier spacing for both HDR and VHDR modes. Figure 6.4a) shows the ergodic capacity of 100 CM1 realisations averaged over all received frames. Note that the estimated MIMO transfer function per sub-carrier incorporates the influence of spatial correlation for antenna spacing equal to the maximum wavelength of the MB-OFDM signal ($d = \lambda_{\text{max}}$), antenna characteristics and RF non-idealities on both sides of the transmission link.

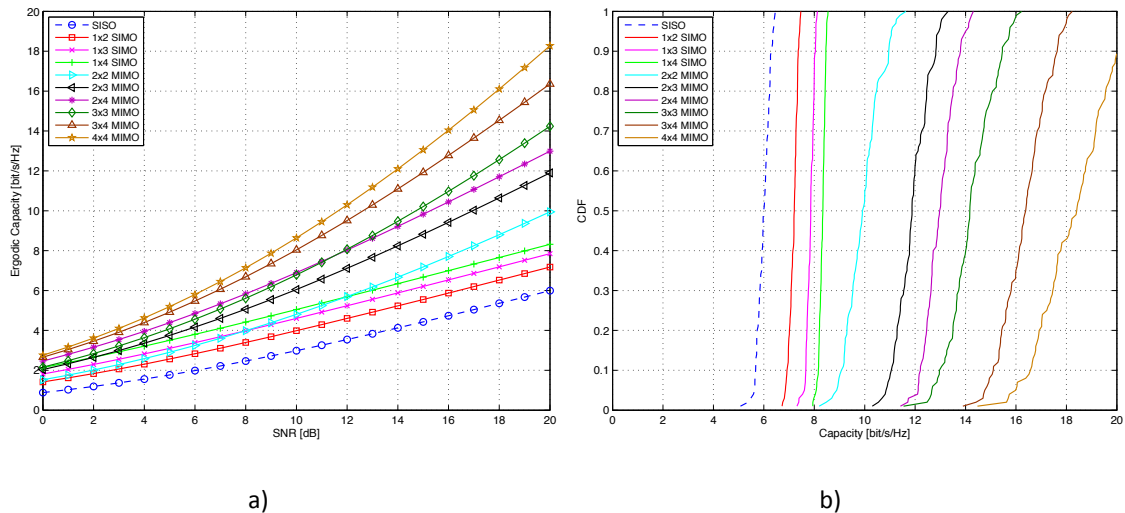


Figure 6.4: Ergodic capacity (a) and CDF thereof (b) of the MIMO-UWB channel for CM1.

As illustrated in Figure 6.4b), at estimated SNR of 20 dB the spectral efficiency of the measured MIMO-UWB channel for outage probabilities of less than 10% is considerably higher than that of SISO. As expected, each receive antenna provides additional capacity gain to the spatial multiplexing system, that remains constant with increasing the SNR. In the case of equal number of transmit and receive antennas, the capacity gain increases linearly with the size of the array. For comparison, Figure 6.5 shows the measured spectral efficiency under 1m LOS conditions for different MIMO configurations. The higher levels of the capacity as compared with the simulated results in Figure 6.4a) can be explained with the strong LOS characteristic of the environment and lower values of the spatial correlation during measurements, where the antenna spacing of $d = 10$ cm slightly exceeds the maximum wavelength of the signal.

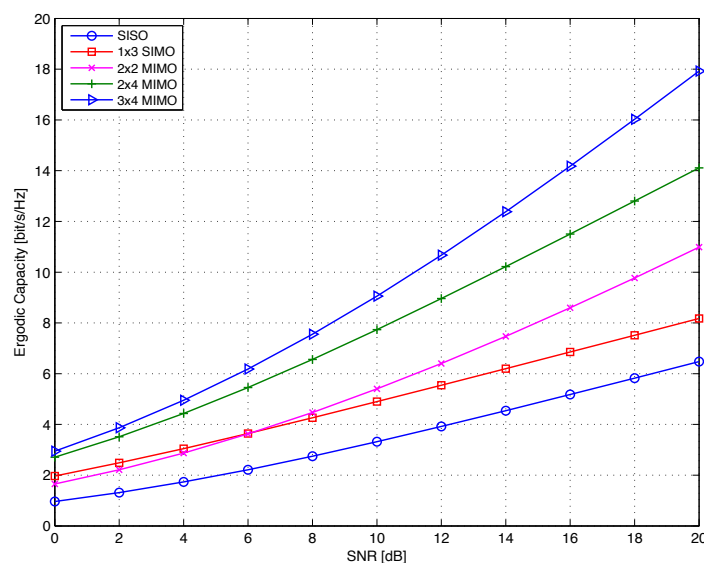


Figure 6.5: Measured ergodic capacity of the MIMO-UWB channel under LOS for different antenna configurations.

Figure 6.6 illustrates the effect of antenna spatial correlation on the ergodic capacity of a spatially multiplexed 3×4 MIMO system in CM1 as function of the antenna element spacing d . For low SNR values, the capacity loss due to higher correlation continually increases. A degradation of about 2 bit/s/Hz in spectral efficiency remains nearly constant as the spatial correlation among the multiple streams increases in the high SNR regime.

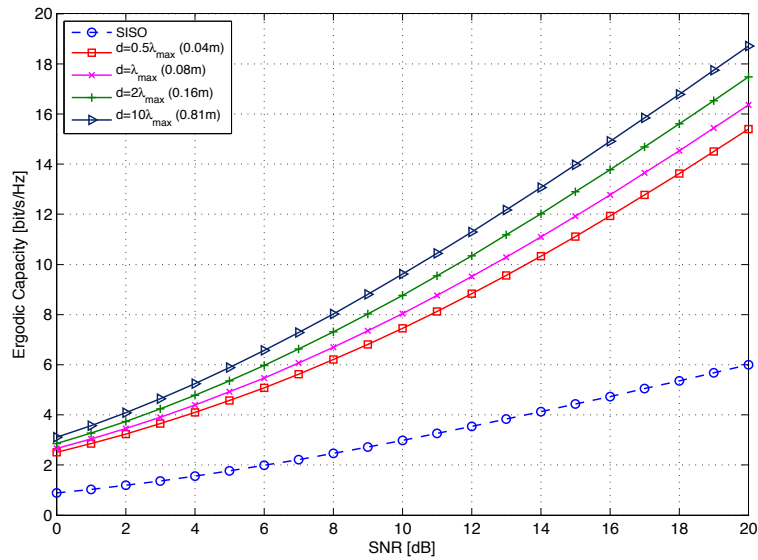


Figure 6.6: Ergodic capacity of a 3×4 MIMO system in CM1 as function of the antenna spacing.

We further calculate the maximum theoretically achievable throughput of the system taking into account the increase in overhead of the MIMO MB-OFDM transmission due to the increased total preamble size. The superframe format is compliant with the ECMA-369 MAC specification, as illustrated in Figure 6.7, including a Beaconsing Period (BP), Data Transmission Period (DTP) and initial spectrum sensing phase.

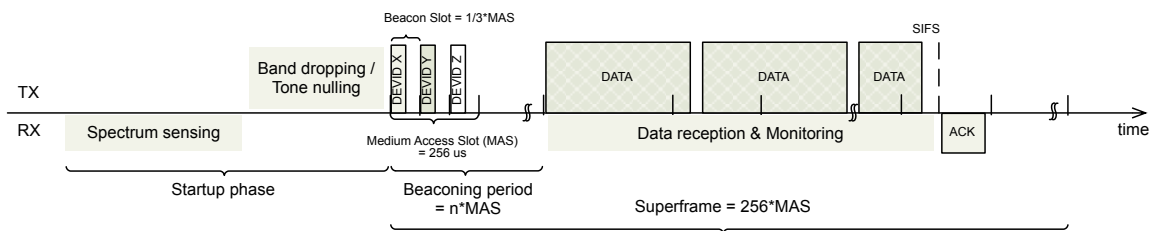


Figure 6.7: Superframe format of MB-OFDM.

Assuming NO-ACK scheme and collision-free medium access according to the Distributed Reservation Protocol (DRP) [3], we first plot the theoretical maximum throughput (TMT) for the different HDR modes as function of the payload size, see Figure 6.8. As expected, for all data rate modes the achievable throughput is maximized for the largest payload size caused by the reduced overhead in the system. For payload sizes above 1 KB, the effective throughput gain remains nearly constant with increasing modulation order, whereas for shorter frames it is largely independent of the payload data rate.

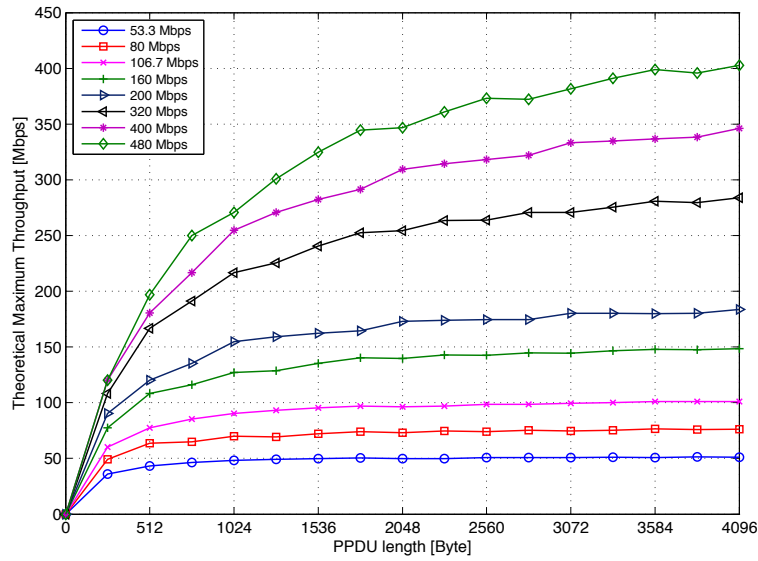


Figure 6.8: Theoretical maximum throughput for HDR modes as function of the PPDU length.

Here, the TMT is calculated as

$$S_{\text{DRP}} = \frac{8N_{\text{MT,MSDU}}L_{\text{MSDU}}}{T_{\text{DRPcycle}}} R, \quad (6.2)$$

where $N_{\text{MT,MSDU}}$ stands for the number of PPDU frames that fit in the maximum reserved time slots for transmission, L_{MSDU} is the MSDU frame size in Byte, and T_{DRPcycle} is the reservation duration in case of DRP. The deduction factor R corresponds to the ratio of the actual data transmission period to the superframe duration, and accounts for any packet losses or re-transmissions [62]. In the calculation, we further adjust the total PPDU frame duration T_{PPDU} and PLCP preamble length $T_{\text{PLCPpream}}$ as

$$T_{\text{PLCP,pream}} = (N_{\text{PS}} + N_{\text{FS}} + N_{\text{T}}N_{\text{CE}})T_{\text{SYM}} \quad \text{and} \quad T_{\text{PPDU}} = T_{\text{PLCP,pream}} + T_{\text{PLCP,hdr}} + N_{\text{PPDU}}T_{\text{SYM}} / N_{\text{T}}$$

to reflect the overhead due to time-orthogonal MIMO CE sequence and multiplexing gain (or equivalently reduced payload duration). The frame-related parameters have been adopted from the ECMA-368 specification in [3].

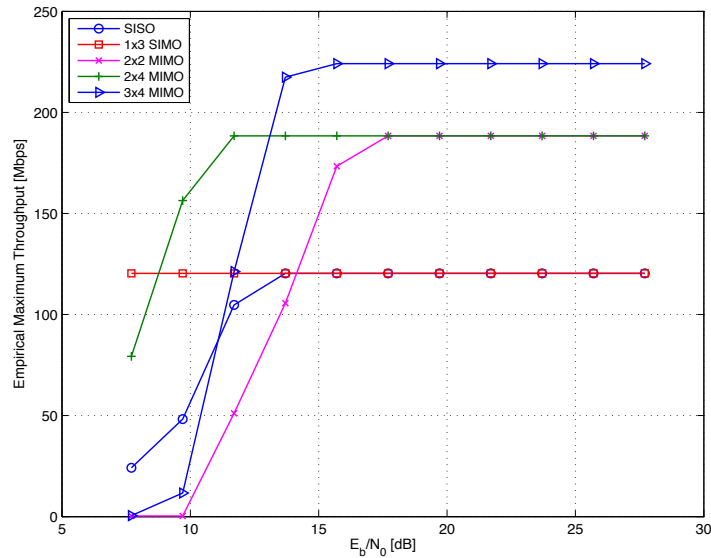


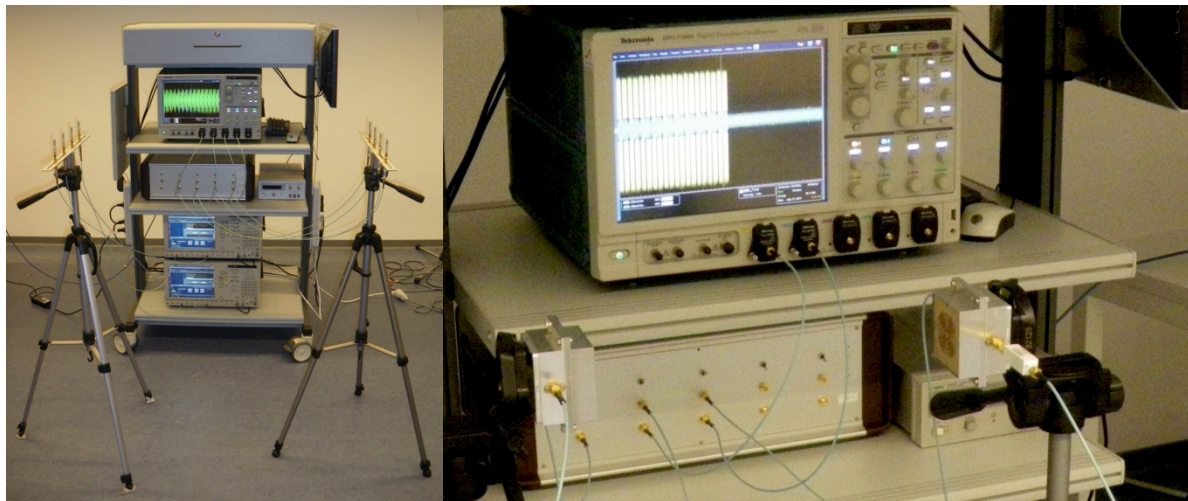
Figure 6.9: Empirical maximum throughput for 160 Mbps ($R_c = 1/2$, QPSK, TDS) mode with different MIMO configurations in 1m LOS.

Figure 6.9 illustrates the empirical maximum throughput with different antenna configurations for 1m LOS and fixed payload size of 1024 Byte. Depending on the number of correctly received frames, the TMT of the DRP protocol is calculated as function of the E_b/N_0 under the assumption of NO-ACK policy, hard reservations and burst transmission. The MIMO system with SMUX operates in mode 160 Mbps per antenna branch, resulting in linear increase in data rate over the air that is proportional to $\min(N_T, N_R)$. As consequence of the higher overhead of the MIMO preamble, the throughput gain decreases with higher number of the multiplexed streams. For fixed number of TX antennas, the maximum theoretical throughput can be reached for lower values of E_b/N_0 as the diversity gain increases with each additional RX antenna. However, as the MIMO system requires higher E_b/N_0 for equivalent performance with respect to SISO (due to e.g. correlated channels, imperfect CE or sub-optimal detection), reaching the maximum throughput levels for MIMO still requires additional amount of the energy per bit.

6.3 Performance Verification in Indoor Environment

The test and verification of the MIMO algorithms selected for FPGA implementation were conducted in both laboratory and typical office environment, including desks, metal cabinets, wooden cupboards, computers and smaller scattering objects of different kind. In accordance with the envisioned deployment scenarios, measurements were performed in short range LOS and obstructed LOS environment based on the evolved set-up of the offline MIMO-UWB test-bed (Figure 6.10) described before. The TX/RX antenna masts were positioned in 110 cm height and 1 m apart in LOS scenarios. For measurements in BG1 (3168 MHz to 4752 MHz), we used small-size omni-directional UWB patch antennas, providing a maximum directive gain of 3dBi in the abovementioned frequency

range. The use of omni-directional antennas was guided by the fact that they facilitate the dense multipath propagation, which is especially favourable for MIMO transmissions. The transmit and receive antenna arrays were set in a linear configuration with 10 cm inter-antenna separation (Figure 6.11), corresponding to the largest wavelength of the transmitted signals. The temporal stationarity of the channel was ensured by the absence of moving objects/persons, thus allowing us to assume a quasi-static channel conditions during a single MB-OFDM frame.



a)

b)

Figure 6.10: Evolved set-up of the offline MIMO-UWB test-bed with a) linear omni-directional antenna array, and b) dual-polarized antennas.

For the verification of Dual mode transmission with the implemented MMSE-SQRD receiver, we use dual-polarized antenna elements (Figure 6.11) to exploit the polarization fading mitigation and suppress miss-alignments of the TX/RX arrays [56][57]. This becomes advantageous especially in symmetric e.g. 2×2 MIMO systems, as the self-interference among the sub-channels can be effectively suppressed leading to diagonalization of the channel matrix and improved performance of the MIMO detectors.

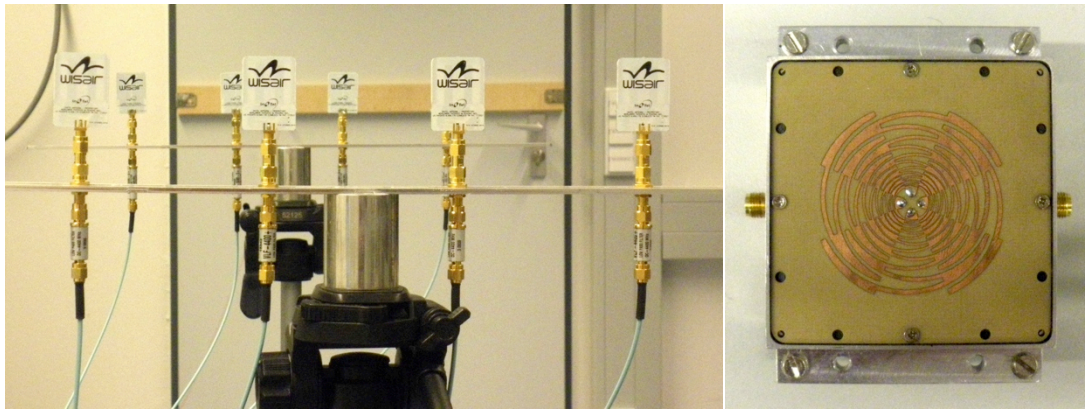


Figure 6.11: Close view of the a) linear array of omni-directional patch antennas for BG1 measurements, and b) log.-per. dual-polarized antennas for Dual Mode in BG1&BG6.

Table 6.3 lists the MIMO configurations and data rates for HDR/VHDR transmission that have been selected for FPGA implementation and algorithm verification.

Table 6.3: Selected MIMO HDR/VHDR modes for measurements and FPGA algorithm verification.

Mode ID	N_T	N_R	HDR (Mbps) FPGA/MATLAB	VHDR (Mbps) MATLAB	Remark
1	1	1	480	1920	Reference mode, MMSE QRD-based receiver
2	2	2	960	3840	Dual mode, MMSE QRD-based receiver
3	≤ 4	≤ 4	1920	7680	SMUX, MMSE-SQRD SIC
4	4	2	480*	1920*	Orthogonal STFC with soft decision decoding
5	≤ 4	≤ 4	-	-	Per-bin interference detection

* Data rates are calculated for Alamouti coding, deduced by the factor 3/4 for orthogonal STFC with 3 or 4 TX antennas.

All measured performance results for up to 4×4 MIMO configurations of MB-OFDM HDR/VHDR transmission imply multiples of the information bit rate as compared to SISO at no additional increase in transmit signal power or required bandwidth. It is therefore aim of this performance validation to demonstrate the ability of spatial multiplexing to linearly increase the system data rate and to verify the possible SNR degradation that is to be traded-off for such an increase in capacity. For spatial diversity schemes, we demonstrate the improvement in minimum SNR required to reach a target BER/PER, which is directly translated to enhancements of the link quality and coverage of the system. To ensure fair comparison among the different modulation schemes, the average power of the signal constellation has been normalized to unity. The maximum allowed transmit power has been equally divided over the antenna branches, ensuring pair comparison to the reference SISO transmission.

We now consider the deployment scenarios described in Section 5.1. In the A340 Mock-up environment, measured channel coverage data from Access Point Configuration (APC) 1 and 2 has

been acquired, including both Horn-Biconical-Horn and Biconical-Biconical antenna options, see Figure 6.12 and [13] for details.

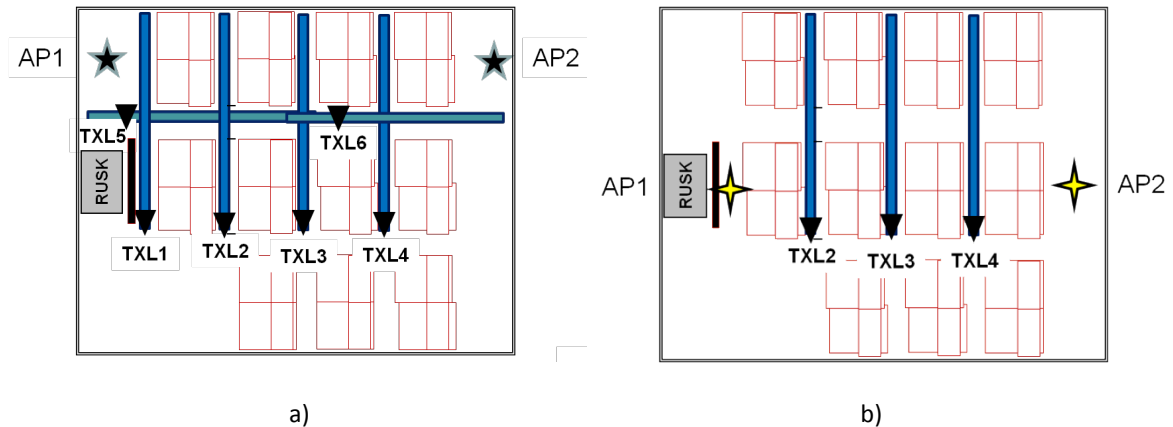


Figure 6.12: Access point configurations of the channel coverage measurements within the A340 Mock-up in [13]: a) APC1, b) APC2.

For the HE environment, we first consider measurement constellations of the multi-speaker (MS) scenario with a single user sitting on a sofa in the middle of a living room. Next, we verify the system performance in the single-point (sound bar) and two-point ambisound scenario using both bi-conical and Vivaldi antenna types, see Figure 6.13a-c).

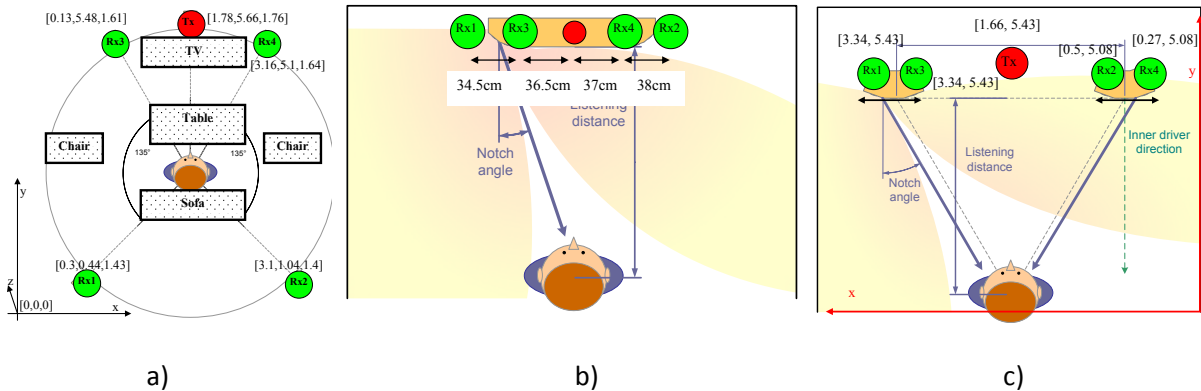


Figure 6.13: Antenna arrangement in the Home Entertainment Environment [13]: a) multi-speaker scenario, b) single-point ambisound (sound bar), c) two-point ambisound system.

Figure 6.14 shows the measured Packet Error Rate (PER) performance of 1×2 SIMO MB-OFDM in an A340 Mock-up at the premises of EWUB partner EADS, as well as in a Home Entertainment environment set up at IKT, comprising a single-point ambisound system, couch, cupboards, table, flowers, etc. within an emulated living room. In both scenarios, reliable performance is ensured for SNR values below 16 dB in the HE SISO case, and approximately 10 to 11 dB in SIMO transmission for a target PER of 8%.

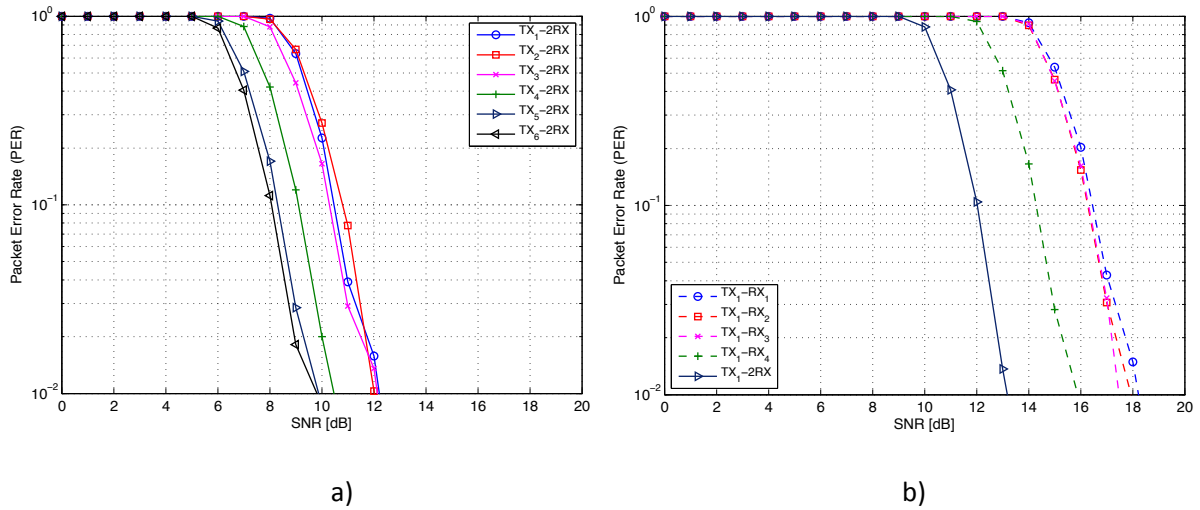


Figure 6.14: PER performance of 160 Mbps MB-OFDM in: a) A340 Mock-up APC1, and b) HE environment with single-point ambisound system.

We next compare the BER performances of the selected multiplexing and diversity algorithms both for fixed-point implementation on the FPGA platform, and offline floating-point processing of the acquired measurement data in MATLAB.

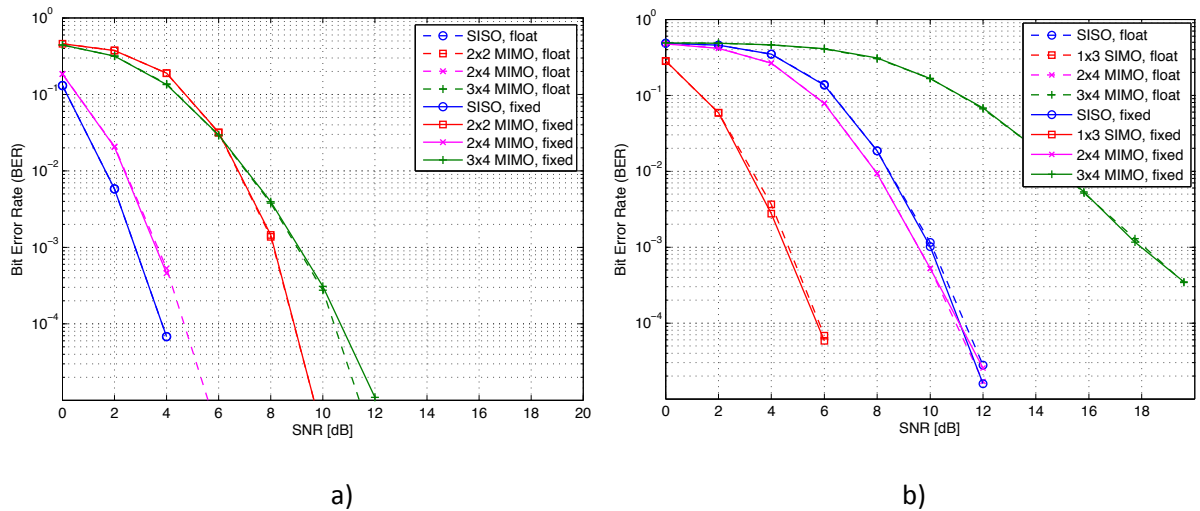


Figure 6.15: BER performance of MMSE-SQRD RX on FPGA with different antenna configurations: a)

$R_c = 1/2$, QPSK, TDS=2, and b) $R_c = 3/4$, DCM.

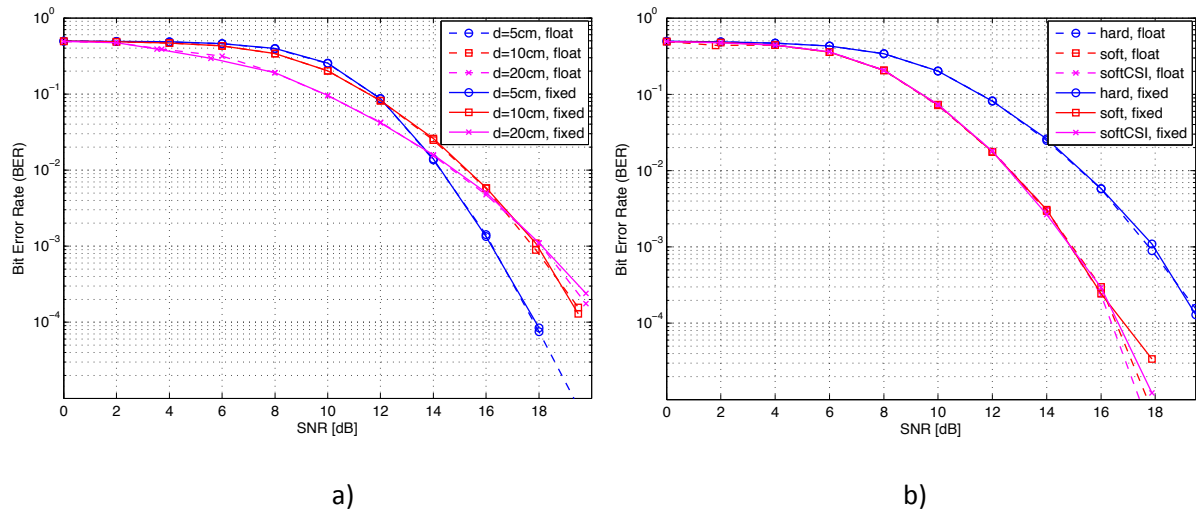


Figure 6.16: Measured BER performance of 3×4 MMSE-SQRD RX on FPGA for different a) antenna spacing, and b) decision type, $R_c = 3/4$, DCM.

Figure 6.15 shows the coded BER performances of the spatially multiplexed MIMO MB-OFDM system with the implemented MMSE-SQRD RX for a) 160 Mbps, and b) 480 Mbps per TX antenna branch. Comparing 1×3 SIMO with SISO, and 2×4 with 2×2 MIMO SMUX, each additional RX antenna is able to provide both array and diversity gains to the system, amounting to a total improvement of approximately 4.5 dB in the required SNR. Due to the strongly correlated channels in 1m LOS environment, the system can exploit only marginal diversity gains, as the slope of the BER curves remains nearly unchanged. The effect of spatial correlation (modelled by varying the antenna element spacing) on the performance of 3×4 MMSE-SQRD RX is illustrated in Figure 6.16a). In the high SNR regime, an antenna spacing close to half the maximum wavelength outperforms the cases when the spacing equals or is twice the maximum signal wavelength. This could be explained by the oscillating behaviour of the spatial correlation across the antenna element separation [84], and the fact that closely spaced antennas at the RX collect a slightly higher amount of signal energy, thus effectively improving the quality of detection due to higher SNR. It is further well known that providing soft decision to the Viterbi decoder is able to deliver additional performance gains, which account for nearly 3 dB as shown in Figure 6.16b).

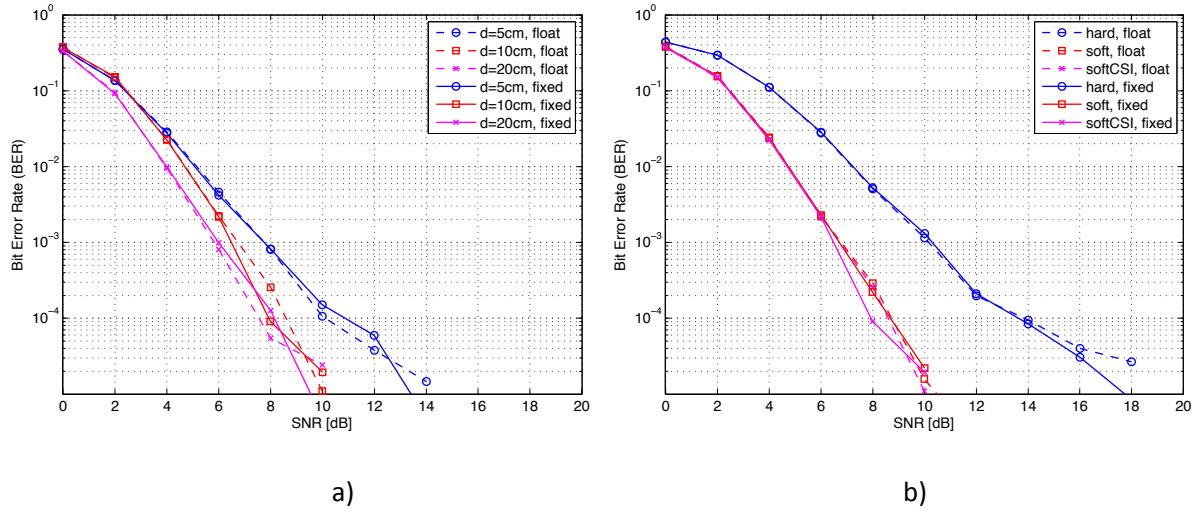


Figure 6.17: Measured BER performance of the orthogonal 4×2 STFC decoder on FPGA for different a) antenna spacing, and b) decision type, $R_c = 3/4$, DCM.

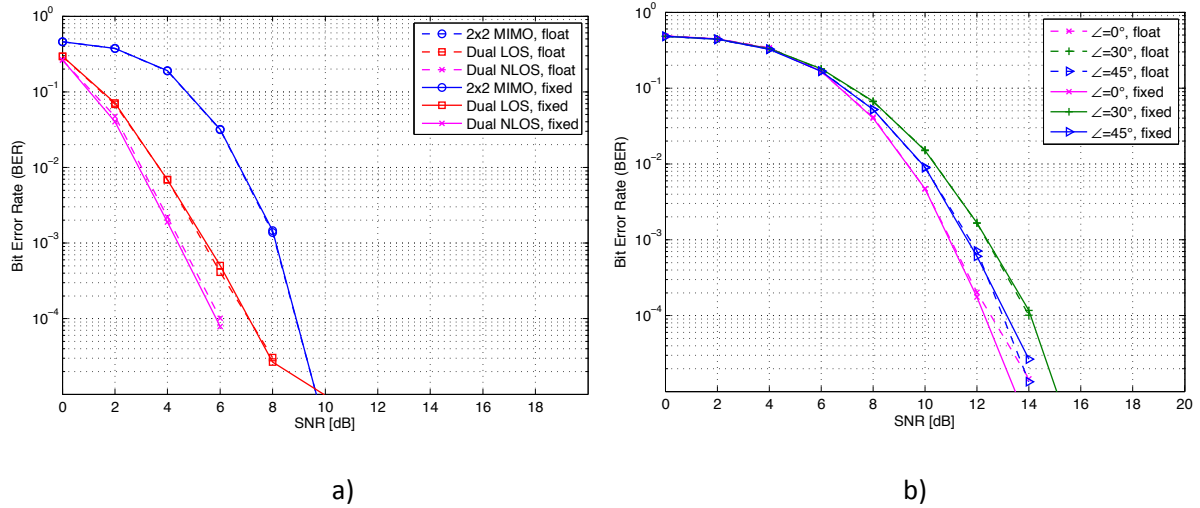


Figure 6.18: Measured BER performance of Dual Mode on FPGA with MMSE RX for a) $R_c = 1/2$, QPSK, TDS=2, and b) different antenna orientation, $R_c = 3/4$, DCM.

In case of orthogonal 4×2 STFC, an antenna spacing close to or exceeding the maximum wavelength of the MB-OFDM signal leads to nearly 2dB performance improvement as the decoder benefits from the higher diversity offered by the less correlated channel coefficients. Comparing soft with hard decision performance in Figure 6.17b), we observe an additional diversity gain of around 5dB by using soft outputs and the energy scaled LLR metric, as the STB decoder is able to minimize the error propagation in the succeeding channel decoding. Finally, in Figure 6.18 we provide measured performance results for Dual Mode transmission in BG1 and BG6 with a) 160 Mbps, and b) 480 Mbps per link as function of the antenna orientation. We observe in the left part of the figure that Dual Mode can improve the BER of a 2×2 MIMO system by nearly 3dB. As the spatial streams become orthogonal in the frequency domain, the channel matrix is effectively orthogonalized leading to reduced self-interference between the links and enhanced performance of the MMSE detection.

In Figure 6.18b) we notice that optimum orientation of the dual-polarized antennas is able to provide additional 2 dB gain, since the isolation between the cross polarizations varies with the relative angle of the antenna arms.

For all measurement modes and selected receivers, the implemented fixed-point FPGA processing shows reliable and stable behaviour, with marginal to negligible deviations from the floating-point performance in the SNR range of interest.

6.4 Conclusions

In this chapter, we have provided measured performance results for selected MIMO schemes. The measurement set-ups and interfaces of the offline MIMO-UWB as well as deployment scenarios have been defined. The comparison of floating-point processing and fixed-point FPGA implementation results reveals only marginal deviations in performance, suggesting the feasibility of the proposed solutions. Regarding Dual Mode operation, significant performance gains can be achieved as compared to symmetric 2×2 MIMO systems due to the orthogonality of the signals paths and the relaxed channel matrix decomposition.

Although the implementation of the proposed MIMO algorithms has been verified only with offline hardware-in-the-loop simulations, it has been carried out in a way that the resource consumption and performance results are valid also for a real-time system. There are some fixed-point losses because of the high amount of consecutive fixed-point arithmetic operations, which each may cause small inaccuracy to the results. In general, the performance and resource consumption show that the implemented algorithms are feasible with the selected FPGA processing units.

In summary, we have provided validation results for an FPGA design platform, which contains parallel implementations of SISO MMSE decoder, 2×2 MIMO MMSE decoder, up to 4×4 MIMO MMSE-SQRD SIC decoder, 4×2 STFC decoder, and a differential interference detector.

Chapter 7

Summary and Conclusions

The main focus of this thesis has been the system design and validation of advanced multiple antenna schemes aiming at highest data rates, extended coverage and robustness of UWB short-range communications. We have demonstrated the inherent advantages of MIMO technology combined with MB-OFDM transmission for selected deployment scenarios and application requirements.

In particular, the capacity gains offered by spatial multiplexing have been validated both by means of extensive simulations and real-world measurement campaigns. We have further deployed and verified the performance of low-complexity sub-optimal MIMO decoding algorithms for V-BLAST architectures, based on (sorted) QR-Decomposition and MMSE criterion. For coded 3×4 MIMO MB-OFDM with spatial multiplexing, the receiver performance of the VHDR mode is only slightly degraded as compared to that of an exhaustive search ML decoder. Moreover, under strong LOS environments over very short distances, we have demonstrated that especially for symmetric MIMO systems the deployment of e.g. dual-polarized antennas can significantly improve the system performance in terms of error propagation. The result of this orthogonal transmission over separate polarization dimensions is a diagonalization of the MIMO channel matrix, which can be easily inverted or decomposed via QRD, especially in the case of bad-conditioned channels. The same positive effect has been observed in Dual Mode operation, in which the transmit signals are placed on different sub-bands, thus minimizing the cross-interference of the TX-RX signal paths. The performance of the above orthogonal transmission schemes outperforms that of conventional symmetric MIMO systems by several dB in the minimum required SNR and is much less influenced by antenna spatial correlations due to increased isolation between the signal paths.

For transmit diversity schemes, we have provided an orthogonal STF coding framework including simple algebraic rules for reliable decoding in MIMO systems deploying up to 4 TX and arbitrary number of RX antennas. Moreover, we propose an efficient approach of delivering soft-decision inputs to the channel decoding stage, by scaling the LLR metric with the estimated channel energy. The performance results indicate improvement of the minimum required SNR at the receiver that can be directly translated to enhancements of the system coverage or reduction of the TX power in case power savings become of interest.

In addition to these multiplexing and diversity schemes, we propose a low-complexity differential interference detector which scans the available spectrum for incumbent users and reacts accordingly by dropping an interfered sub-band or generating TN mask for the subsequent transmit frame, as envisioned by the DAA approach. Measurement and simulation results indicate sufficiently high probabilities of interference detection at INR values well below 0 dB, whereas the inherent gains of using multiple antennas improve the algorithm performance in terms of both lower probability of false alarm and of missed detection.

For all considered MIMO schemes, the impact of RF frontend imperfections has been analyzed, modelled and evaluated. Suitable approaches for the estimation and compensation of PN, I/Q imbalance and CFO been proposed and validated. The corresponding performance results prove their suitability and robustness in the entire MB-OFDM RX operational range. Moreover, reliable timing and TFC acquisition algorithms have been developed and verified under real-world constraints and HW effects. The proposed synchronization block is able to perform fast frame- and hopping pattern acquisition with sufficiently low probabilities of false alarm and missed detection, whereas the RMS of the timing offset for worst-case CM4 simulations lies below 2 samples for SNR values exceeding 0 dB. As expected, the array and diversity gains offered by using multiple antennas at the RX relax the

setup of the detection threshold as compared to SISO case, and further improve the synchronization performance in terms of probability of detection.

Finally, notes on the resource consumption of the FPGA implementation of selected MIMO schemes indicate that the performance results are valid also for a real-time system. Even with some fixed-point losses, the performance degradation compared to floating-point simulations in MATLAB is only marginal. In general, the resource evaluation and prediction have shown that the implemented algorithms are feasible with the selected FPGA processing units. In summary, validation results for a hardware-in-the-loop prototyping Virtex6 FPGA platform have been provided that comprises the parallel implementations of a SISO MMSE, 2×2 MIMO MMSE with QRD, scalable up to 4×4 MMSE-SQRD SIC, and 4×2 STF decoder, as well as of a differential interference detector.

This thesis has contributed to the field of high-speed, short-range UWB communications with multiple antennas on both side of the link. The feasibility of the proposed system and algorithm designs and achievable MIMO gains has been verified via real-world measurements, including the estimation and compensation of RF frontend imperfections. The flexible and modular system design enables both extensive algorithm development and test in the common programming environment, as well as hardware-in-the-loop co-simulations and real-time transmissions over the air. The developed offline MIMO-UWB test-bed and FPGA prototyping platform featuring several low-complexity implementations of MIMO receivers provide ideal basis for further algorithm design, measurement and verification in current and future research areas, including, but not limited to UWB and MIMO.

List of Figures

Figure 2.1: Worldwide UWB power emission limits.	6
Figure 2.2: WiMedia frequency band plan	7
Figure 2.3: Time-frequency interleaving in MB-OFDM	8
Figure 2.4: MB-OFDM TX architecture.....	10
Figure 2.5: MB-OFDM RX architecture	12
Figure 2.6: Typical realisation of a) the impulse responses, and b) PDPs of a spatially correlated 2×2 MIMO-UWB CM1.	16
Figure 2.7: CDF of the mean excess delay of the spatially correlated MIMO-UWB channel model.....	17
Figure 2.8: Absolute value of the spatial correlation coefficient of the SIMO channel impulse responses.	18
Figure 2.9: Frequency behaviour of the spatial correlation coefficient for varying antenna spacing. .	19
Figure 3.1: Spatial Multiplexing scheme for MIMO Wireless Communications.	23
Figure 3.2: Dual mode operation of MB-OFDM with multiple antennas.....	24
Figure 3.3: Space-Time-Block Coding with Alamouti scheme.....	26
Figure 3.4: Measured BER performance of uncoded vs. coded 3×4 MIMO MB-OFDM with different decoders in 1m LOS a,b) HDR ($R_c = 3/4$, DCM) and c,d) VHDR ($R_c = 1/2$, 16-QAM).....	30
Figure 4.1: General concept of a modular MIMO MB-OFDM system.....	32
Figure 4.2: Xilinx ML605 development board with Virtex 6 XC6VLX240T FPGA.....	34
Figure 4.3: PER of MB-OFDM as function of the achievable distance in CM1 for different antenna configurations ($R_c = 1/2$, QPSK).	37
Figure 4.4: VHDR frequency band plan.....	38
Figure 4.5: PHY Header bit assignment.....	40
Figure 4.6: Standard PPDU frame structure	41
Figure 4.7: MIMO PLCP preamble transmission	42
Figure 4.8: Worldwide frequency allocation for UWB devices according to [10].....	43
Figure 4.9: Synchronization of time-frequency interleaved signals.....	45

Figure 4.10: Coarse time- and TFC acquisition per RX branch.	47
Figure 4.11: Block diagram of CCF metric calculation.....	48
Figure 4.12: Proposed TFC acquisition in a frequency-hopping MB-OFDM system.	49
Figure 4.13: Probability of detection for different a) antenna configurations in CM1, and b) channel models CM1-4 (TFC6, SNR=0 dB).	52
Figure 4.14: Probabilities of false alarm and missed detection a) in CM1-4 for TFC6, and b) in CM1 for different TFCs (SNR=0 dB).	52
Figure 4.15: Average RMS of STO estimate a) in CM1-4 for TFC6, and b) in CM1 for different TFCs. ...	53
Figure 4.16: Average MSE of channel estimation for a) SISO in CM1-4 with different TFCs, and b) 3×4 MIMO with different antenna spacing in CM1 with TFC6.	55
Figure 4.17: Effect of phase noise on the received QPSK constellation.	57
Figure 4.18: Influence of I/Q imbalance on the received sub-carriers of the: up) RF signal, and down) baseband OFDM signal.	58
Figure 4.19: I/Q imbalance at a single RX antenna branch.....	59
Figure 4.20: Impact of I/Q imbalance on the received DCM constellation.....	60
Figure 4.21: I/Q imbalance estimation and compensation per antenna branch.	61
Figure 4.22: Effect of I/Q imbalance on the a) uncoded BER performance, and b) average MSE of channel estimation of 480 Mbps MB-OFDM (1m LOS, TFC8).	61
Figure 4.23: Block diagram of an iterative CFO estimator.....	62
Figure 4.24: Performance of CFO estimation and compensation in terms of the a) measured uncoded BER for QPSK in 1m LOS, and b) normalized average MSE of CFO estimation in AWGN and CM1 for CFO=4%.	63
Figure 5.1: Deployment scenarios of the FP7 IP EUWB [39][40].	66
Figure 5.2: Measured BER performance of VHDR MB-OFDM with 16-QAM for different MIMO configurations and a) uncoded, and b) $R_c=1/2$ coded transmission in 1m LOS.....	69
Figure 5.3: Measured performance of 3×4 MIMO (V)HDR MB-OFDM as function of the a) antenna spacing, and b) soft/hard decision metric in 1m LOS.....	70
Figure 5.4: Measured BER performance of 2×2 MIMO in LOS with dual-polarized antennas as function of the vertical antenna orientation for $R_c=3/4$ and a) DCM, and b) 16-QAM mapping.	71
Figure 5.5: Measured BER performance of Dual Mode in LOS/NLOS for different data rates.	71

Figure 5.6: Block diagram of MIMO detection with MMSE-based Sorted QR Decomposition.....	72
Figure 5.7: Measured BER performance of a) HDR ($R_c = 3/4$, DCM, TFC8) and, b) VHDR mode ($R_c = 1/2$, 16-QAM, TFC11) in 1m LOS for different antenna configurations.	75
Figure 5.8: Measured BER performance of 3×4 MIMO MB-OFDM in 1m LOS for a) QRD-based MMSE, and b) O-SIC with MMSE-based SQRD receiver.....	75
Figure 5.9: Block diagram of STF soft-decision combining with scaled LLR calculation.....	78
Figure 5.10: Measured BER performance of orthogonal STFC (total rate $R=18/32$, TFC6) for different antenna configurations and modulations: a) QPSK, and b) 16-QAM.....	82
Figure 5.11: Measured BER performance of 4×2 orthogonal STFC (total rate $R=18/32$, TFC6) for different data rates as function of the a) decision type, and b) antenna spacing d	82
Figure 5.12: Co-existing scenario between UWB and WiMAX.....	83
Figure 5.13: Flow diagram of per-bin differential interference detection.....	85
Figure 5.14: Block diagram of interference detection.	86
Figure 5.15: Performance of WiMAX interference detection for a) 3×4 MIMO and different values of the INR, and b) different antenna configurations for fixed threshold ($\eta = 0.3$) in CM1.	87
Figure 5.16: Resource utilization of the implemented MIMO algorithms on XCVLX240T FPGA platform.	90
Figure 6.1: General setup of the MIMO-UWB test-bed	94
Figure 6.2: Block diagram of Dual Mode transmission via the MIMO-UWB test-bed.	95
Figure 6.3: MIMO MB-OFDM MATLAB Simulator and GUI for instrument control	97
Figure 6.4: Ergodic capacity (a) and CDF thereof (b) of the MIMO-UWB channel for CM1.....	100
Figure 6.5: Measured ergodic capacity of the MIMO-UWB channel under LOS for different antenna configurations.	100
Figure 6.6: Ergodic capacity of a 3×4 MIMO system in CM1 as function of the antenna spacing. ...	101
Figure 6.7: Superframe format of MB-OFDM.	101
Figure 6.8: Theoretical maximum throughput for HDR modes as function of the PPDU length.	102
Figure 6.9: Empirical maximum throughput for 160 Mbps ($R_c = 1/2$, QPSK, TDS) mode with different MIMO configurations in 1m LOS.	103
Figure 6.10: Evolved set-up of the offline MIMO-UWB test-bed with a) linear omni-directional antenna array, and b) dual-polarized antennas.....	104

Figure 6.11: Close view of the a) linear array of omni-directional patch antennas for BG1 measurements, and b) log.-per. dual-polarized antennas for Dual Mode in BG1&BG6.	105
Figure 6.12: Access point configurations of the channel coverage measurements within the A340 Mock-up in [13]: a) APC1, b) APC2.	106
Figure 6.13: Antenna arrangement in the Home Entertainment Environment [13]: a) multi-speaker scenario, b) single-point ambisound (sound bar), c) two-point ambisound system.	106
Figure 6.14: PER performance of 160 Mbps MB-OFDM in: a) A340 Mock-up APC1, and b) HE environment with single-point ambisound system.	107
Figure 6.15: BER performance of MMSE-SQRD RX on FPGA with different antenna configurations: a) $R_c = 1/2$, QPSK, TDS=2, and b) $R_c = 3/4$, DCM.	107
Figure 6.16: Measured BER performance of 3×4 MMSE-SQRD RX on FPGA for different a) antenna spacing, and b) decision type, $R_c = 3/4$, DCM.	108
Figure 6.17: Measured BER performance of the orthogonal 4×2 STFC decoder on FPGA for different a) antenna spacing, and b) decision type, $R_c = 3/4$, DCM.	109
Figure 6.18: Measured BER performance of Dual Mode on FPGA with MMSE RX for a) $R_c = 1/2$, QPSK, TDS=2, and b) different antenna orientation, $R_c = 3/4$, DCM.	109

List of Tables

Table 2.1: Main parameters of the IEEE 802.15.3a UWB CM1-4 in [16].....	14
Table 4.1: Main parameters of the WPAN IEEE 802.15.3a statistical path loss model in [15].	35
Table 4.2: Link budget of HDR MB-OFDM in AWGN.....	37
Table 4.3: Link budget of VHDR MB-OFDM in 1m LOS	38
Table 4.4: Timing- and rate dependent parameters of HDR/VHDR MB-OFDM	39
Table 4.5: Bit assignment for rate-dependent parameters	40
Table 4.6: Supported MIMO modes	41
Table 4.7: Band group allocation for BG1 and BG6	43
Table 4.8: Supported Time-Frequency Codes for BG1 and BG6.	44
Table 4.9: Conditional probabilities of frame acquisition.....	50
Table 5.1: Parameters of the WiMAX interference scenario.	84
Table 5.2: Comparison of FFT hardware requirements for K MIMO branches	89
Table 5.3: Synthesis of selected MIMO algorithms to XCVLX240T FPGA.....	90
Table 6.1: Main specifications of Tektronix AWG7102.....	94
Table 6.2: Main specifications of Tektronix DPO71604	96
Table 6.3: Selected MIMO HDR/VHDR modes for measurements and FPGA algorithm verification.	105

Bibliography

- [1] E. Telatar, "Capacity of multi-antenna Gaussian channels," *European Transactions on Communications*, vol. 10, no. 6, pp. 585-595, 1999.
- [2] G. J. Foschini and M. J. Gans, "On limits of wireless communications in a fading environment when using multiple antennas," *Wireless Personal Communications*, vol 6, no. 3, pp. 311-335, 1998.
- [3] Ecma International, "High Rate Ultra Wideband PHY and MAC Standard," Standard ECMA 368, 3rd Edition, Dec. 2008, web page: www.ecma-international.org
- [4] G. Heidari. WiMedia UWB – Technology of choice for wireless USB and Bluetooth. John Wiley & Sons. 2008.
- [5] K. Mandke et al., "The Evolution of Ultra Wide Band Radio for Wireless Personal Area Networks", *High Frequency Electronics*, pp. 22-32, Sept. 2003.
- [6] Federal Communications Commission, "FCC Revision of Part 15 of the Commission's Rules Regarding Ultra-Wideband Transmission Systems," Feb 2002.
- [7] A. Batra et al., "Design of a Multiband OFDM System for Realistic UWB Channel Environments", *IEEE Transactions on Microwave Theory and Techniques*, Vol. 52, pp. 2123- 2138, Sept. 2004.
- [8] T. Schenk, P. Smulders, and E. Fledderus, "Multiple Carriers in Wireless Communications - Curse or Blessing?", *Tijdschrift Ned. Elektron.- \& Radiogenoot. (NERG)*, Vol. 70. No. 4, pp. 112-123, Dec. 2005.
- [9] A. Batra et al., "Multi-band OFDM Physical Layer Proposal for IEEE 802.15 Task Group 3a", *IEEE P802.15-03/268r2*, Nov. 2003.
- [10] WiMedia Alliance, web page: <http://www.wimedia.org>
- [11] S. Mirabbasi and K. Martin, "Classical and Modern Receiver Architectures", *IEEE Communications Magazine*, Nov. 2000.
- [12] X. Hong, C. Wang, B. Allen, and W. Q. Malik, "Correlation-based double-directional stochastic channel model for multiple-antenna ultra-wideband systems," *IET Microw. Antennas Propag.*, vol. 1, no. 6, pp. 1182 -1191, 2007.
- [13] EUWB Deliverable D3.1.2b. "Application-specific MIMO-UWB channel measurements and parameter extraction (final)," available at <http://euwb.eu/deliverables>.
- [14] A. A. M. Saleh and R. Valenzuela, "A statistical model for indoor multipath propagation," *IEEE J. Select. Areas Commun.*, vol. SAC-5, no. 2, pp. 128-137, Feb. 1987.
- [15] S. S. Ghassemzadeh and V. Tarokh, *The Ultra-wideband Indoor Path Loss Model*, Report IEEE P802.15-02/277r0-SG3a, 2002.
- [16] J. Foerster, "Channel Modeling Sub-committee Report Final," IEEE P802.15-02/490r1-SG3a, 2003.
- [17] J. Adeane, W. Q. Malik, I. J. Wassell, and D. J. Edwards, "Simple correlated channel model for ultrawideband multiple-input multiple-output systems," *IET Microwaves, Antennas & Propagation*, vol. 1, pp. 1177-1181, 2007.
- [18] V. Poor: "MIMO Wireless Communications", Cambridge University Press, 2007.

-
- [19] G. J. Foschini, "Layered space-time architecture for wireless communication in a fading environment when using multi-element antennas", *Bell Labs Tech. J.*, 1(2):41-59, 1996.
- [20] S. Alamouti, "A simple transmit diversity technique for wireless communications," *IEEE Sel. Areas Comm.*, pp. 1451-1458, Oct. 1998.
- [21] M. Jankiranam: "Space-Time Codes and MIMO Systems", Artech House, 2004.
- [22] W. P. Siriwongpairat, M. Olfat, and K. J. R. Liu, "Multiband-OFDM MIMO coding framework for UWB communication systems," *IEEE Transactions on Signal Processing*, vol. 54, no. 1, pp. 214–224, Jan. 2006.
- [23] A. Burg: "VLSI Circuits for MIMO Communication Systems", Hartung-Gorre Verlag Konstanz, 2006.
- [24] A. Wilzeck: "A Software Defined Radio Approach for High Data-Rate Multi-Antenna Wireless Communications with Frequency Domain Processing", Shaker Verlag, 2009.
- [25] EUWB Deliverable D3.3.2. "Application-aware algorithm and system design for link quality enhancements and range extension for VHDR," available at <http://euwb.eu/deliverables>.
- [26] EUWB Deliverable D3.4.1. "Resource evaluation and prediction of multiple antenna solutions via prototyping," available at <http://euwb.eu/deliverables>.
- [27] PULSERS II Deliverable D2a1.1. "Definition of VHDR MBO link-level simulator".
- [28] T. M. Schmidl and D. C. Cox, "Robust frequency and timing synchronization for OFDM," *IEEE Transactions on Communications*, vol. 45, no. 12, pp. 1613-1621, 1997.
- [29] H. Minn, V. K. Bhargava, and K. B. Letaief, "A robust timing and frequency synchronization for OFDM systems," *IEEE Transactions on Wireless Communications*, vol. 24, no. 5, pp. 822-839, May. 2003.
- [30] J.-T. Lai, A.-Y. Wu, and W.-C. Chen, "A Systematic Design Approach to the Band-Tracking Packet Detector in OFDM-Based Ultrawideband Systems," *IEEE Transactions on Vehicular Technology*, vol. 56, no. 6, pp. 3791–3806, Nov. 2007.
- [31] Z. Ye, C. Duan, P. Orlik, and J. Zhang, "A Low-Complexity Synchronization Design for MB-OFDM Ultra-Wideband Systems," *2008 IEEE International Conference on Communications*, pp. 3807-3813, 2008.
- [32] PULSERS II Deliverable D2a-1.2. "Study of VHDR MB-OFDM timing acquisition".
- [33] D. Petrovic, W. Rave, and G. Fettweis, "Intercarrier Interference due to Phase Noise in OFDM - Estimation and Suppression," *IEEE Vehicular Technology Conference (VTC 2004)*, pp. 1901-1905, 2004.
- [34] T. C. W. Schenk, P. F. M. Smulders, and E. R. Fledderus, "On the influence of phase noise induced ICI in MIMO OFDM systems," *IEEE Communications Letters*, vol. 9, no. 8, pp. 682-684, Aug. 2005.
- [35] A. van Zelst and T. C. W. Schenk, "Implementation of a MIMO OFDM-Based Wireless LAN System," *IEEE Transactions on Signal Processing*, vol. 52, no. 2, pp. 483-494, Feb. 2004.
- [36] T. C. W. Schenk, P. F. M. Smulders, and E. R. Fledderus, "Estimation and compensation of TX and RX IQ imbalance in OFDM-based MIMO systems," *2006 IEEE Radio and Wireless Symposium*, pp. 215-218.
- [37] M. Windisch and G. Fettweis, "Standard-Independent I/Q Imbalance Compensation in OFDM Direct-Conversion Receivers," in *9th International OFDM Workshop (InOWo'04)*, 2004.

- [38] A. Burg, M. Borgmann, M. Wenk, M. Zellweger, W. Fichtner, and H. Bolcskei, "VLSI implementation of MIMO detection using the sphere decoding algorithm," *IEEE Journal of Solid-State Circuits*, vol. 40, no. 7, pp. 1566-1577, Jul. 2005.
- [39] EUWB Deliverable D3.1.1. "Definition of system concepts, requirements and application scenarios," available at <http://euwb.eu/deliverables>.
- [40] S. Zeisberg, V. Schreiber, "EUWB - Coexisting Short Range Radio by Advanced Ultra-Wideband RadioTechnology," ICT Mobile and Wireless Communications Summit, Stockholm, June 2008.
- [41] D. Wübben, R. Bohnke, V. Kuhn, and K.-D. Kammeyer, "MMSE extension of V-BLAST based on sorted QR decomposition," *2003 IEEE 58th Vehicular Technology Conference. VTC 2003-Fall (IEEE Cat. No.03CH37484)*, no. 1, pp. 508-512 Vol.1, 2003.
- [42] L. C. Tran and A. Mertins, "Space-Time-Frequency Code implementation in MB-OFDM UWB communications: Design criteria and performance," *IEEE Transactions on Wireless Communications*, vol. 8, no. 2, pp. 701-713, Feb. 2009.
- [43] X.-B. Liang, "Orthogonal designs with maximal rates", *IEEE Trans. on Inform. Theory* vol. 49, no. 10, pp. 2468-2503, 2003
- [44] H. Wang, X.-G. Xia, "Upper bounds of rates of complex orthogonal space-time block codes", *IEEE Trans. on Inform. Theory* vol. 49, no. 10, pp. 2788-2796, 2003.
- [45] G.B. Giannakis, Z. Liu, X. Ma, and S. Zhou: "Space-time coding for broadband wireless communications", New Jersey: John Wiley & Sons, 2007, pp. 61-68.
- [46] R. Nordman, "Soft decision decoding of the orthogonal complex MIMO codes for three and four transmit antennas," *Physical Communication*, vol. 5, no. 1, 2012.
- [47] F. Berens, "The European Detect and Avoid approach for UWB," WALTER DAA Tutorial, ETSI, Sophia Antipolis, France, 2009.
- [48] T. Sansaloni, A. Pérez-Pascual, V. Torres, and J. Valls, "Efficient pipeline FFT processors for WLAN MIMO-OFDM systems," *Electronics Letters*, vol. 41, no. 19, pp. 1043-1044, 2005.
- [49] S. Lee, Y. Jung, and J. Kim, "Low complexity pipeline FFT processor for MIMO-OFDM systems," *IEICE Electronics Express*, vol. 4, no. 23, pp. 750-754, 2007.
- [50] L. Liu, J. Ren, X. Wang, and F. Ye, "Design of Low-Power, 1GS/s Throughput FFT Processor for MIMO-OFDM UWB Communication System," *2007 IEEE International Symposium on Circuits and Systems*, pp. 2594-2597, May 2007.
- [51] T. Kaiser, F. Zheng, and E. Dimitrov, "An Overview of Ultra Wideband Systems with MIMO", *Proceedings of the IEEE*, vol.97, no.2, pp.285-312, 2009.
- [52] T. Kaiser and F. Zheng, *Ultra Wideband Systems with MIMO*, John Wiley & Sons, Ltd, 2010.
- [53] EUWB Deliverable D3.2.2. "Definition of the evolved set-up of a 4×4 MIMO test-bed and set-ups for multi-user/interferer scenario," available at <http://euwb.eu/deliverables>.
- [54] S. Caban, C. Mehlführer, R. Langwieser, A. L. Scholtz, and M. Rupp, "Vienna MIMO Testbed," *EURASIP Journal on Advances in Signal Processing*, vol. 2006, pp. 1-14, 2006.
- [55] T. Kaiser, A. Wilzeck, M. Berentsen, and M. Rupp, "Prototyping for MIMO Systems - An Overview," in *Proc. 12th European Signal Processing Conference (EUSIPCO'04)*.
- [56] O. Klemp, G. Armbrecht, and H. Eul, "On the Polarization Diversity Performance of Log-Per. Multiarm-Antennas for MB-OFDM UWB Communications," in *Proceedings of the 3rd Workshop on Positioning, Navigation and Communication (WPNC'06)*, 2006, pp. 105-110.

- [57] G. Armbrecht, O. Klemp, and I. Rolfes, "Radio Science Correlation properties of dual polarized antennas with finite pattern orthogonality in mobile fading channels," *Advances In Radio Science*, no. 2005, pp. 95-99, 2007.
- [58] W. Q. Malik and D. J. Edwards, "Measured MIMO Capacity and Diversity Gain With Spatial and Polar Arrays in Ultrawideband Channels," *IEEE Transactions on Communications*, vol. 55, no. 12, pp. 2361-2370, Dec. 2007.
- [59] A. F. Molisch, "Ultrawideband propagation channels and their impact on system design," *2007 International Symposium on Microwave, Antenna, Propagation and EMC Technologies for Wireless Communications*, pp. K4- 1-K4- 5, Aug. 2007.
- [60] W. Malik, "MIMO capacity and multipath scaling in ultra-wideband channels," *Electronics Letters*, vol. 44, no. 6, pp. 427-428, 2008.
- [61] M. Chiani, M. Z. Win, and A. Zanella, "On the Capacity of Spatially Correlated MIMO Rayleigh Fading Channels," *T-IT*, vol. 49, no. 10, pp. 2363-2371, 2003.
- [62] Y. Zang, G. Hiertz, J. Habetha, B. Otal, H. Sirin, and H. J. Reumerman, "Towards high speed wireless personal area network-efficiency analysis of MBOA MAC," in *Proceedings of International Workshop on Wireless Ad-Hoc Networks 2005 (IWWAN 2005)*, Feb 2005.
- [63] H. Boelcskei, D. Gesbert, and A. Paulraj, "On the capacity of wireless systems employing OFDM-based spatial multiplexing," *IEEE Trans. Comm.*, pp. 225-234, Feb. 2002.
- [64] Xilinx.com, Virtex-6 FPGA ML605 Evaluation Kit, web page: <http://www.xilinx.com/products/devkits/EK-V6-ML605-G.htm>
- [65] J. P. Kermaol, L. Schumacher, K. I. Pedersen, P. E. Mogensen, and F. Frederiksen, "A Stochastic MIMO Radio Channel Model With Experimental Validation," *IEEE Journal on Selected Areas in Communications*, vol. 20, no. 6, pp. 1211-1226, 2002.
- [66] D. Sen, S. Chakrabarti, and R. V. R. Kumar, "An Efficient Timing Synchronization Scheme for Ultra-Wideband Multi-Band OFDM Systems," *Environment*. 2007.
- [67] P. Luethi, A. Burg, S. Haene, D. Perels, N. Felber, and W. Fichtner, "VLSI Implementation of a High-Speed Iterative Sorted MMSE QR Decomposition," in *2007 IEEE International Symposium on Circuits and Systems*, 2007, no. 2, pp. 1421-1424.
- [68] H. S. Kim, W. Zhu, J. Bhatia, K. Mohammed, A. Shah, and B. Daneshrad, "An efficient FPGA based MIMO-MMSE detector," in *Proceedings of 15th European Processing Conference (EUSIPCO 2007)*, 2007, vol. 1, no. Eusipco, pp. 1131-1135.
- [69] A. Zanella, M. Chiani and M. Z. Win, "MMSE Reception and Successive Interference Cancellation for MIMO Systems with High Spectral Efficiency", *IEEE Transactions on Wireless Communications*, vol. 4, pp. 1244-1253, 2005.
- [70] T. A. Cover and Joy A. Thomas. *Elements of Information Theory*. John Wiley & Sons, Inc., New York, NY, 10158, first edition, 1991.
- [71] A. Goldsmith. *Wireless Communications*. Cambridge University Press, 2005.
- [72] J. H. Winters, "On the capacity of radio communication systems with diversity in Rayleigh fading environment", *IEEE J. Sel. Areas Comm.*, vol. 5, no.5, pp. 871-878, 1987.
- [73] M. Win and R. Scholtz, "On the energy capture of ultrawide bandwidth signals in dense multipath environments," *IEEE Communications Letters*, vol. 2, no. 9, 1998, pp. 245-247.
- [74] M. Mroue et al., "Performance of a simple architecture of an analog CMOS detector for MB-UWB receiver," *International Conference on Ultra-Wideband*, Marina Bay, Singapore, pp. 107-112.

- [75] M. Simon and V. Vilnrotter, "Alamouti-type space-time coding for free-space optical communication with direct detection," *IEEE Transactions on Wireless Communications*, vol. 4, no. 1, 2005, pp. 35-39.
- [76] L. Yang and G. Giannakis, "Analog space-time coding for multiantenna ultra-wideband transmissions," *IEEE Trans. Commun.*, vol. 52, no. 3, 2004, pp. 507-517.
- [77] A. Molisch, J. Foerster, and M. Pendergrass, "Channel models for ultrawideband personal area networks," *IEEE Wireless Communications*, vol. 6, no. 10, 2003, pp. 14-21.
- [78] S.-K. Yong, "TG3c channel modelling sub-committee final report," Technical Report, IEEE, 2009.
- [79] A. Anttonen, A. Mämmelä, P. Pasupathy "Low complexity phase-unaware detectors based on estimator-correlator concept," in *Ultra-Wideband Communications: Novel Trends*, InTech, 2011.
- [80] S. Zeisberg, V. Schreiber, "EUWB - Coexisting Short Range Radio by Advanced Ultra-Wideband Radio Technology," *ICT Mobile and Wireless Communications Summit*, Stockholm, June 2008.
- [81] EUWB Deliverable D3.3.1. "Application-aware algorithm and system design for extremely high data rates," available at <http://euwb.eu/deliverables>.
- [82] EUWB Deliverable D3.3.3. "Application-aware algorithm and system design for multi-user enhancements for VHDR," available at <http://euwb.eu/deliverables>.
- [83] EUWB Deliverable D3.2.1. "Definition of the initial set-up of a 2×4 MIMO test-bed," available at <http://euwb.eu/deliverables>.
- [84] W. Q. Malik, "Spatial correlation in ultrawideband channels," *IEEE Transactions on Wireless Communications*, vol. 7, no. 2, pp. 604-610, Feb. 2008.
- [85] J. Penketh and M. Collados, "Performance and implementation complexity of receiver algorithms for MIMO-OFDM based wireless LAN systems," in *Proc. 15th IEEE International Symposium in Personal, Indoor and Mobile Radio Communications*, Sept. 2004, pp. 1522-1526.
- [86] F. Nekoogar, "Ultra-Wideband Communications: Fundamentals and Applications", Prentice Hall, 2005.
- [87] W. P. Siritwongpairat, "Cross-Layer Design for Multi-Antenna Ultra-Wideband Systems," 2005.
- [88] P. W. Wolniansky, G. J. Foschini, G. D. Golden, and R. a. Valenzuela, "V-BLAST: an architecture for realizing very high data rates over the rich-scattering wireless channel," *1998 URSI International Symposium on Signals, Systems, and Electronics. Conference Proceedings (Cat. No.98EX167)*, pp. 295-300.
- [89] C. Mehlführer, S. Geirhofer, S. Caban, and M. Rupp, "A flexible MIMO testbed with remote access," in *Proceedings of 13th European Signal Processing Conference (EUSIPCO'05)*, 2005, pp. 2-5.
- [90] M.-O. Wessman, A. Svensson, and E. Agrell, "Frequency diversity performance of coded multiband-OFDM systems on IEEE UWB channels," *IEEE 60th Vehicular Technology Conference, 2004. VTC2004-Fall. 2004*, pp. 1197-1201, 2004.
- [91] C. Snow, L. Lampe, and R. Schober, "Performance analysis and enhancement of multiband OFDM for UWB communications," *IEEE Transactions on Wireless Communications*, vol. 6, no. 6, pp. 2182-2192, 2007.
- [92] H. Boche, A. Bourdoux, J. R. Fonollosa, T. Kaiser, A. Molisch, and W. Utschick, "Smart antennas: state of the art," *IEEE Vehicular Technology Magazine*, vol. 1, no. 1, pp. 8-17, Mar. 2006.
- [93] S. H. Yoon and J. W. Chong, "Packet detection and symbol timing synchronization algorithm for Multi-Band OFDM UWB," *IEICE Transactions on Communications*, vol. 89, no. 4, p. 1433, 2006.

-
- [94] T. Haustein, A. Forck, H. Gäbler, V. Jungnickel, and S. Schiffermüller, "Real-Time Signal Processing for Multiantenna Systems: Algorithms, Optimization, and Implementation on an Experimental Test-Bed," *EURASIP Journal on Advances in Signal Processing*, vol. 2006, pp. 1–22, 2006.
- [95] G. L. Stuber, J. R. Barry, S. W. Mclaughlin, Y. G. Li, M. a. Ingram, and T. G. Pratt, "Broadband MIMO-OFDM Wireless Communications," *Proceedings of the IEEE*, vol. 92, no. 2, pp. 271–294, Feb. 2004.
- [96] A. Batra, J. Balakrishnan, and A. Dabak, "MULTI-BAND OFDM: A NEW APPROACH FOR UWB," in *Proceedings of the 2004 International Symposium on Circuits and Systems, 2004 (ISCAS'04)*, 2004, vol. 5, pp. 4–7.
- [97] A. Burg, M. Borgmanr, M. Wenk, C. Studer, and H. Bolcskei, "Advanced receiver algorithms for MIMO wireless communications," in *Proceedings of the Design Automation & Test in Europe Conference*, 2006, p. 6 pp.
- [98] G. Ren, Y. Chang, and H. Zhang, "SNR estimation algorithm based on the preamble for wireless OFDM systems," *Science in China Series F: Information Sciences*, vol. 51, no. 7, pp. 965–974, Jun. 2008.
- [99] M. Speth, S. a. Fechtel, G. Fock, and H. Meyr, "Optimum receiver design for wireless broad-band systems using OFDM - Part I," *IEEE Transactions on Communications*, vol. 47, no. 11, pp. 1668–1677, 1999.
- [100] M. Speth, S. Fechtel, G. Fock, and H. Meyr, "Optimum receiver design for OFDM-based broadband transmission -Part II - A case study," *IEEE Transactions on Communications*, vol. 49, no. 4, pp. 571–578, Apr. 2001.
- [101] W. P. Siritwongpairat and K. J. R. Liu, "Performance characterization of multiband UWB communication systems using Poisson cluster arriving fading paths," *IEEE Journal on Selected Areas in Communications*, vol. 24, no. 4, pp. 745–751, Apr. 2006.
- [102] A. Molisch, M. Z. Win, and J. Winters, "Space-time-frequency (STF) coding for MIMO-OFDM systems," *IEEE Communications Letters*, vol. 6, no. 9, pp. 370–372, Sep. 2002.
- [103] A. Molisch, "Ultrawideband Propagation Channels-Theory, Measurement, and Modeling," *IEEE Transactions on Vehicular Technology*, vol. 54, no. 5, pp. 1528–1545, Sep. 2005.
- [104] H. Minn, M. Zeng, and V. K. Bhargava, "On timing offset estimation for OFDM systems," *IEEE Communications Letters*, vol. 4, no. 7, pp. 242–244, Jul. 2000.

Own Contributions

Conferences:

C. T. Le, E. Dimitrov, A. Anggraini, J. Peissig, H.-P. Kuchenbecker, "Effect of Spatial Correlation on MMSE-Based Interference Alignment in a Multiuser MIMO MB-OFDM System," 8th IEEE International Conference on Wireless and Mobile Computing, Networking and Communications, WiMob 2012, Barcelona, Spain, 2012.

E. Dimitrov, C. Kupferschmidt, T.Kaiser, J. Korpi, R. Nordman, A. Anttonen, A. Giorgetti, and M. Chiani, "Design and Implementation of Advanced Algorithms for MIMO-UWB Wireless Communications," 2011 IEEE International Conference on Ultra-Wideband, ICUWB 2011, Bologna, Sept 12-14, 2011.

C. T. Le, E. Dimitrov, S. Moghaddamnia, and T. Kaiser, "Performance Investigation of MMSE-Based Interference Alignment for Multiuser MIMO UWB," 2011 IEEE International Conference on Ultra-Wideband, ICUWB 2011, Bologna, Sept 12-14, 2011.

C. Kupferschmidt, E. Dimitrov, and T. Kaiser, "Multiple Antenna UWB Systems WP3 of the EUWB-Project", The 2009 International Conference on Advanced Technologies for Communications, Hai Phong, Vietnam, Oct 12-14, 2009.

E. Dimitrov and T. Kaiser, "Advanced MIMO VHDR MB-OFDM Approaches," 2008 IEEE International Conference on Ultra-Wideband, ICUWB 2008, Hannover, Sept 10-12, 2008.

C. Kupferschmidt, E. Dimitrov and T. Kaiser, "Multiple Antenna UWB Systems - WP3 of the EUWB Project," Invited Session, 2008 IEEE International Conference on Ultra-Wideband, ICUWB 2008, Hannover, Sept 10-12, 2008.

F. Berens, E. Dimitrov, T. Kaiser, A. Anttonen, A. Krause, and A. Weir, "An enhanced very high data rate UWB airinterface based on the WIMEDIA standard - An European View," 2007 IEEE International Conference on Ultra-Wideband, ICUWB 2007, Singapore, Sept 24-26, 2007.

F. Berens, E. Dimitrov, T. Kaiser, A. Anttonen, A. Krause, and A. Weir, "The PULSERS II view towards very high data rate OFDM based UWB systems," 16th ICT Mobile and Wireless Communications Summit, Budapest, July 1-5, 2007.

Journals:

T. Kaiser, F. Zheng, and E. Dimitrov, An Overview of Ultra Wideband Systems with MIMO, *Proceedings of the IEEE*, vol.97, no.2, pp.285-312, 2009.

T. Kaiser, C. Senger, J. Schroeder, S. Galler, E. Dimitrov, M. El-Hadidy, and B. Tau Sieskul, Ultra-Wideband Wireless Systems: A Broad Overview, *Union Radio-Scientifique Internationale (URSI)*, pp. 24-40, March 2007.

Curriculum Vitae

Persönliche Daten

Name: Emil Dimitrov
 Geburtsdatum: 01. Oktober 1977
 Geburtsort: Sofia, Bulgarien

Beruflicher Werdegang

seit 07/2011 wiseSense GmbH, Hannover
Senior Software-Entwickler

10/2006 – 06/2011 Institut für Kommunikationstechnik IKT, Leibniz Universität Hannover
Wissenschaftlicher Mitarbeiter

Wissenschaftlicher Werdegang

10/2000 – 09/2006 Universität Duisburg-Essen, Standort Duisburg
Master of Science (M.Sc.) der Informations- und Kommunikationstechnik, Studienrichtung Kommunikationstechnik

10/1996 – 03/2000 Universität St. Kliment Ohridski, Sofia
Studium des Wirtschaftsmanagement, Stipendiat des „Soros - Open Society Institute“ sowie des bulgarischen Bildungsministeriums

09/1991 – 07/1996 Gymnasium „First English Language School“, Sofia
Abitur mit Auszeichnung